

# **INVESTIGATION OF THE RHEOLOGICAL BEHAVIOUR OF NANOSUSPENSIONS**

**A Thesis Submitted to  
the Graduate School of Engineering and Sciences of  
İzmir Institute of Technology  
in Partial Fulfillment of the Requirements for the Degree of**

**MASTER OF SCIENCE**

**in Materials Science and Engineering**

**by**

**Öykü ÇELEN**

**September, 2011**

**İZMİR**

We approve the thesis of **Öykü ÇELEN**

---

**Prof. Dr. Muhsin ÇİFTÇİOĞLU**  
Supervisor

---

**Prof. Dr. Devrim BALKÖSE**  
Committee Member

---

**Assoc. Prof. Dr. Mustafa DEMİR**  
Committee Member

20 September 2011

---

**Assoc. Prof. Dr. Mustafa DEMİR**  
Head of the Department of  
Materials Science and Engineering

---

**Prof. Dr. Sedat AKKURT**  
Dean of the Graduate School of  
Engineering and Sciences

## **ACKNOWLEDGEMENTS**

I would like to express my gratitude in the first place to my advisor Prof. Dr. Muhsin Çiftçiođlu who provided me the opportunity to do research on particle synthesis and rheology of colloidal suspensions. His guidance and encouragement throughout this research was a great help. My special thanks to Özlem Çađlar Duvarcı for her constant help in rheology measurements and FTIR analysis. Thanks to the Center for Material Research staff for their understanding, friendly cooperation, and support.

I would like to express my gratitude to all members of my family, for their patience, understanding, and support all throughout the study.

# ABSTRACT

## INVESTIGATION OF THE RHEOLOGICAL BEHAVIOUR OF NANOSUSPENSIONS

The rheology of concentrated calcium carbonate, titania, silica, alumina and zirconia suspensions of submicron/nanosized particles in non-aqueous media was investigated. Calcium carbonate and silica particles were synthesized by carbonation route and Stöber method respectively while titania, alumina and zirconia powders were obtained commercially. Suspensions of the ball milled natural calcium carbonate powders were also prepared. The dispersion of these powders especially at high solids loadings was observed to be difficult. The viscosity of the 45 vol% suspensions of precipitated  $\text{CaCO}_3$  particles increased about 21 times at a shear rate of  $400 \text{ sec}^{-1}$  relative to its initial value indicating shear-thickening behaviour.

The onset of shear thickening was at 20, 30 and 40 vol% for three different commercial titania powder suspensions. The onset of shear thickening was at lower solids volume contents and the increase in viscosity with shear rate was far less dramatic for the titania suspensions with polydispersed particle size distributions. The critical shear rate was  $187 \text{ sec}^{-1}$  for silica suspensions at 47 vol% with a discontinuous jump in viscosity. Rheological data at higher shear rates was not obtained due to the torque limitations of the rheometer.

The critical shear rate of the polydispersed alumina powder suspensions were higher than their relatively monodispersed counterparts. The highest solids loading achieved in alumina based suspensions was 62 vol%.

The dynamic shear rheology measurements showed that the solid part of the silica suspension was becoming more dominant over the liquid part as the solid content was increased. The volume fraction dependence of the high shear viscosity was fitted to a modified Krieger-Dougherty model for titania and silica suspensions. The fit of the rheological data to the Power law and to a modified version of Cross model were analysed.

# ÖZET

## NANOSÜSPANSİYONLARIN REOLOJİK DAVRANIŞLARININ İNCELENMESİ

Mikronaltı/nanoboyutlu kalsiyum karbonat, titan, silika, alümina ve zirkonya tozlarının organik bazlı yoğun süspansiyonlarının reolojisi incelenmiştir. Kalsiyum karbonat parçacıkları kirecin karbondioksit gazıyla çökeltilmesiyle, silika parçacıkları ise Stöber metodu ile sentezlenmiştir. Titan, alümina ve zirkonya tozları da ticari firmalardan sağlanmıştır. Bilyalı değirmende öğütülen doğal kalsiyum karbonat tozlarının reolojik davranışları incelenmiştir. Öğütülmüş bu tozların özellikle yüksek katı hacimsel içeriklerinde sıvı ortamda dağılımı kolay olmamıştır. Çökeltilecek sentezlenen kalsiyum karbonat parçacıklarının katı hacimsel içeriği %45 olan süspansiyonları kayma hızı  $400 \text{ s}^{-1}$ 'ye kadar çıkarılınca viskozitesi ilk değerinin 21 katı artarak kayma hızıyla kalınlaşan akışkan davranışı göstermiştir.

Çeşitli titan süspansiyonlarında kayma kalınlaşma başlangıcı 20, 30 ve %40'lık katı hacimlerinde görülmüştür. Farklı boyutta parçacık dağılımlarına sahip olan titan süspansiyonlarında kayma kalınlaşma davranış başlangıcı daha düşük katı hacimlerinde gerçekleşmiştir ve viskozite artışı önemli ölçüde daha az görülmüştür. Hacimsel olarak %47 katı içeren silika süspansiyonlarının kritik kayma hızı  $187 \text{ s}^{-1}$ 'dir. Bu kayma hızında viskozitede ani bir yükselme görülmüştür. Reometre cihazının tork limitlerinden dolayı yüksek kayma hızlarında veri alınamamıştır.

Parçacık dağılımları çoklu olan alümina süspansiyonlarındaki kritik kayma hızı tekil dağılımlı olanlarına nazaran daha yüksek değerlerde gözlemlenmiştir. En yüksek katı hacmi %62 olarak alümina bazlı süspansiyonlarda görülmüştür.

Dinamik kayma reolojisi ölçümleri silika süspansiyonlarında katı kısmının sıvı kısmına göre daha baskın olduğunu göstermiştir. Titan ve silika dağılımlarında modifiye edilmiş Krieger-Dougherty modeli ile maksimum çıkılabilecek katı parçacık içerikleri hesaplanmıştır. Reolojik verilerin güç kanunu yasası ve modifiye edilmiş Cross modeline uygunlukları analiz edilmiştir.

# TABLE OF CONTENTS

LIST OF TABLES .....	viii
LIST OF FIGURES.....	x
LIST OF SYMBOLS.....	xviii
CHAPTER 1. INTRODUCTION.....	1
CHAPTER 2. RHEOLOGICAL BEHAVIOUR OF COLLOIDAL SUSPENSIONS.....	3
2.1. Shear Thinning.....	3
2.2. Shear Thickening.....	5
2.3. Viscoelasticity.....	10
2.4. Rheological Models of Shear-Thickening Fluids.....	14
2.4.1. Ostwald / de Waele (Power Law).....	14
2.4.2. Modified Cross-Model for shear-thickening fluids.....	15
2.5. Recent Studies on the Rheological Behaviour of Colloidal Suspensions.....	16
CHAPTER 3. EXPERIMENTAL STUDY.....	19
3.1. Preparation of CaCO <sub>3</sub> particles.....	19
3.1.1. CaCO <sub>3</sub> Synthesis by CO <sub>2</sub> Bubbling Method.....	19
3.1.2. Ball milling of CaCO <sub>3</sub> Particles.....	20
3.2. Synthesis of Silica Particles.....	21
3.3. Specifications of Commercial TiO <sub>2</sub> , Al <sub>2</sub> O <sub>3</sub> and ZrO <sub>2</sub> Powders.....	22
3.4. Characterization Methods.....	23
3.5. Rheological Methods.....	23
CHAPTER 4. RESULTS AND DISCUSSION.....	24
4.1. Synthesis, Characterization and Rheological Behaviour of CaCO <sub>3</sub> ....	24
4.1.1. Synthesis of CaCO <sub>3</sub> Particles.....	24

4.1.1.1. CO <sub>2</sub> -bubbling.....	24
4.1.1.2. Ballmilling Process.....	34
4.1.2. Rheological Behaviour of CaCO <sub>3</sub> Suspensions.....	38
4.2. Characterization and Rheological Behaviour of TiO <sub>2</sub> .....	46
4.2.1. Characterization of Commercial TiO <sub>2</sub> Powders.....	46
4.2.2. Rheological Behaviour of TiO <sub>2</sub> suspensions.....	54
4.3. Synthesis, Characterization and Rheological Behaviour of SiO <sub>2</sub> .....	93
4.3.1. Characterization of synthesized SiO <sub>2</sub> particles.....	93
4.3.2. Rheology of synthesized SiO <sub>2</sub> suspensions.....	99
4.4. Characterization and Rheological Behaviour of Al <sub>2</sub> O <sub>3</sub> .....	109
4.4.1. Characterization of Commercial Al <sub>2</sub> O <sub>3</sub> powders.....	109
4.4.2. Rheology of synthesized Al <sub>2</sub> O <sub>3</sub> suspensions.....	111
4.5. Characterization and Rheological Behaviour of ZrO <sub>2</sub> .....	114
4.5.1. Characterization of Commercial ZrO <sub>2</sub> powders.....	114
4.5.2. Rheology of synthesized ZrO <sub>2</sub> suspensions.....	114
CHAPTER 5. CONCLUSIONS.....	116
REFERENCES.....	118

# LIST OF TABLES

<b><u>Table</u></b>	<b><u>Page</u></b>
Table 3.1. Specifications of materials used in sol preparation.....	21
Table 3.2. Synthesis Parameters employed for the preparation of monodisperse silica spheres.....	22
Table 3.3. The specifications of the commercial powders.....	22
Table 4.1. The model parameters of Power Law calculated for the suspensions of Ball1 in ethylene glycol. ....	43
Table 4.2. The model parameters of Power Law of different calculated for the suspensions Ball1 in ethylene glycol prepared by ballmilling.....	46
Table 4.3. The model parameters of modified Krieger-Dougherty model for the suspensions of titania powders. ....	57
Table 4.4. The zero, critic and maximum values of viscosity, shear rate and shear stress of CT1-ethylene glycol suspensions with optimum amount of surfactant.....	62
Table 4.5. The model parameters of Power Law for the suspensions of CT1 in ethylene glycol with optimized amount of surfactant .....	63
Table 4.6. The model parameters of the modified Cross Model for the suspensions of CT1 in ethylene glycol with optimized amount of surfactant .....	67
Table 4.7. The zero, critic and maximum values of viscosity, shear rate and shear stress of CT2-ethylene glycol suspensions.....	70
Table 4.8. The model parameters of Power law model calculated for the suspensions of CT2 in ethylene glycol.....	72
Table 4.9. The model parameters of the modified Cross Model for the suspensions of CT2 in ethylene glycol .....	75
Table 4.10. The zero, critic and maximum values of viscosity, shear rate and shear stress of CT3-ethylene glycol suspensions.....	78
Table 4.11. The model parameters of Power law model calculated for the suspensions of CT3 in ethylene glycol.....	79
Table 4.12. The model parameters of the modified Cross model calculated for the suspensions of CT3 in ethylene glycol .....	82

Table 4.13. The zero, critic and maximum values of viscosity, shear rate and shear stress of CT4-ethylene glycol suspensions.....	85
Table 4.14. The model parameters of Power law model calculated for the suspensions of CT4 in ethylene glycol.....	86
Table 4.15. The model parameters of the modified Cross model calculated for the suspensions of CT4 in ethylene glycol .....	89
Table 4.16. The model parameters of the modified Krieger-Dougherty model calculated for the suspension of SS3.....	99
Table 4.17. The model parameters of Power law model calculated for the suspensions of SS3.....	102
Table 4.18. The model parameters of the modified Cross model calculated for the 47 vol% suspension of SS3 in ethylene glycol .....	104

## LIST OF FIGURES

<b><u>Figure</u></b>	<b><u>Page</u></b>
Figure 2.1. Rheogram of idealized shear-thinning (pseudoplastic) behaviour.....	3
Figure 2.2. Dispersions at rest and flowing through a tube .....	4
Figure 2.3. Apparent viscosity and flow curves for typical time-independent fluids .....	5
Figure 2.4. The schematic representation of viscosity versus shear rate for shear thickening systems at different solids contents.....	6
Figure 2.5. The dependence of the critical shear rate for the onset of shear thickening as function of phase volume of the dispersed phase.....	9
Figure 2.6. Effect of particle size on the critical shear rate at which shear thickening is initiated.....	9
Figure 2.7. The effect of shape on shear thickening.....	10
Figure 2.8. (a) Schematic representation of a typical rheometry setup, with the sample placed between two plates. (b) Schematic representation of stress response to oscillatory strain deformation for an elastic solid, a viscous fluid and a viscoelastic material.....	12
Figure 2.9. Frequency dependence of $G'$ and $G''$ for (a) a suspension of hydrogel particles and (b) for the elastomer blend Further measurements of DC-9040: (c) Strain dependence of $G'$ and $G''$ , (d) Constant-rate measurements at strain rates $0.002\text{ s}^{-1}$ , $0.02\text{ s}^{-1}$ , $0.45\text{ s}^{-1}$ and $10\text{ s}^{-1}$ , (e) master curve of constant-rate measurements that were scaled both in magnitude and frequency.....	13
Figure 3.1. Experimental setup for the carbonation experiment.....	20
Figure 4.1. The SEM micrographs of corn-starch.....	24
Figure 4.2. The SEM micrographs of ceramic gas-diffuser.....	25
Figure 4.3. The XRD pattern of slaked lime.....	26
Figure 4.4. The FTIR spectra of slaked lime.....	26
Figure 4.5. The TGA curve of slaked lime.....	27
Figure 4.6. The SEM micrographs of slaked lime.....	27
Figure 4.7. The pH and conductivity change during $\text{CaCO}_3$ synthesis reaction.....	29

Figure 4.8. The SEM micrograph of sample taken at pH=12.45 from the reaction slurry.....	29
Figure 4.9. The SEM micrograph of sample taken at pH=12 from the reaction slurry.....	30
Figure 4.10. The SEM micrograph of sample taken at pH=11.52 from the reaction slurry.....	30
Figure 4.11. The SEM micrograph of sample taken at pH=9.67 from the reaction slurry.....	31
Figure 4.12. The SEM micrograph of sample taken at pH=7 from the reaction slurry.....	31
Figure 4.13. The XRD pattern of synthesized CaCO <sub>3</sub> particles.....	32
Figure 4.14. The FT-IR spectra of synthesized CaCO <sub>3</sub> particles.....	33
Figure 4.15. The TGA curve of synthesized CaCO <sub>3</sub> particles.....	33
Figure 4.16. The SEM micrographs of natural CaCO <sub>3</sub> particles.....	34
Figure 4.17. The SEM micrographs of Ball1.....	35
Figure 4.18. Particle size distribution of Ball1 at different time intervals.....	35
Figure 4.19. Particle size distribution of Ball1 at the end of 250 min.....	36
Figure 4.20. The SEM micrographs of small zirconia beads used in grinding.....	37
Figure 4.21. The SEM micrographs of Ball2.....	37
Figure 4.22. Particle size distribution of Ball2 at the end of grinding process.....	38
Figure 4.23. Dynamic viscosity curve of 45 vol% suspension of synthesized CaCO <sub>3</sub> particles in ethylene glycol.....	39
Figure 4.24. Flow curve of 45 vol% suspension of synthesized CaCO <sub>3</sub> particles in ethylene glycol.....	39
Figure 4.25. Flow curve of 45 vol% suspension of synthesized CaCO <sub>3</sub> particles in ethylene glycol (the solid line represents the power law model) .....	40
Figure 4.26. Static viscosity curves of the suspensions of Ball1 in ethylene glycol.....	40
Figure 4.27. Dynamic viscosity curves of the suspensions of Ball1 in ethylene glycol.....	44
Figure 4.28. Flow curves of the suspensions of Ball1 in ethylene glycol.....	42

Figure 4.29. Flow curves of the suspensions of Ball1 in ethylene glycol (the solid lines represent the power law model).....	42
Figure 4.30. Static viscosity curves of the suspension of Ball1 in ethylene glycol prepared by ballmilling.....	43
Figure 4.31. Dynamic viscosity curves of the suspensions of Ball1 in ethylene glycol prepared by ballmilling.....	44
Figure 4.32. The comparison of dynamic viscosity curves of the suspensions of Ball1 in ethylene glycol.....	44
Figure 4.33. Flow curves of the suspensions of Ball1 in ethylene glycol prepared ballmilling.....	45
Figure 4.34. Flow curves of the suspensions of Ball1 in ethylene glycol prepared by ballmilling (the solid lines represent the power law model).....	46
Figure 4.35. The FT-IR spectra of commercial TiO <sub>2</sub> powders.....	47
Figure 4.36. The XRD patterns of titania powders.....	48
Figure 4.37. The TGA curves of TiO <sub>2</sub> powders.....	49
Figure 4.38. The particle size distribution of CT1.....	49
Figure 4.39. The particle size distribution of CT2.....	50
Figure 4.40. The particle size distribution of CT3.....	51
Figure 4.41. The particle size distribution of CT4.....	51
Figure 4.42. The comparison of the particle size distributions of titania powders.....	52
Figure 4.43. The SEM micrographs of powder CT1.....	52
Figure 4.44. The SEM micrographs of powder CT2.....	53
Figure 4.45. The SEM micrographs of powder CT3.....	53
Figure 4.46. The SEM micrographs of powder CT4.....	53
Figure 4.47. Flow curve of pure ethylene glycol.....	54
Figure 4.48. Flow curve of pure ethylene glycol (the solid lines represents the power law model).....	55
Figure 4.49. The dynamic viscosity curve of pure ethylene glycol.....	55
Figure 4.50. Relative high shear viscosity as a function of volume fraction of solids for the commercial TiO <sub>2</sub> powders .....	56

Figure 4.51. The dynamic viscosity curves of the suspensions of CT1 in ethylene glycol at different solids contents without surfactant.....	57
Figure 4.52. Flow curves of the suspensions of CT1 in ethylene glycol at different solids contents without surfactant.....	58
Figure 4.53. Viscosity versus the amount of surfactant added per powder CT1 weight at different solids contents.....	59
Figure 4.54. The static viscosity curves of the suspensions of the suspensions of CT1 in ethylene glycol at different solids contents with optimized amount of surfactant.....	59
Figure 4.55. Comparison of the viscosity curves of 30 vol% suspension of CT1 in ethylene glycol with and without surfactant.....	60
Figure 4.56. Flow curves of the suspensions of CT1 in ethylene glycol at different solids contents with optimized amount of surfactant.....	61
Figure 4.57. The dynamic viscosity curves of the suspensions of CT1 in ethylene glycol at different solids contents with optimized amount of surfactant.....	62
Figure 4.58. Flow curves of the suspensions of CT1 in ethylene glycol with optimized amount of surfactant (the solid lines represent the power law model) .....	63
Figure 4.59. Calculated $K_I$ and $K_{II}$ values of the Power law model for the suspensions of CT1 in ethylene glycol with optimized amount of surfactant at different solids contents.....	64
Figure 4.60. Calculated $n_I$ and $n_{II}$ values of the modified Power law model for the suspensions of CT1 in ethylene glycol with optimized amount of surfactant at different solids contents.....	64
Figure 4.61. Calculated $n_I$ and $K_I$ values of Power law model for the suspensions of CT1 in ethylene glycol with optimized amount of surfactant at different solids contents.....	65
Figure 4.62. Calculated $n_{II}$ and $K_{II}$ values of Power law model for the suspensions of CT1 in ethylene glycol with optimized amount of surfactant at different solids contents.....	66
Figure 4.63. Dynamic viscosity curves of the suspensions of CT1 in ethylene glycol with optimized amount of surfactant (the solid lines represent the modified cross model).....	67
Figure 4.64. Calculated $K_I$ and $K_{II}$ values of the modified Cross model for the suspensions of CT1 in ethylene glycol with optimized amount of surfactant.....	68

Figure 4.65. Static viscosity curves of CT2 at different solids contents in ethylene glycol .....	69
Figure 4.66. Flow curves of the suspensions of CT2 in ethylene glycol at different solids contents.....	69
Figure 4.67. Dynamic viscosity curves of the suspensions of CT2 in ethylene glycol at different solids content.....	70
Figure 4.68. Flow curves of the suspensions of CT2 in ethylene glycol at different solids contents (the solid lines represent the power law model).....	71
Figure 4.69. Calculated $K_I$ and $K_{II}$ values of Power law model for the suspension of CT2 in ethylene glycol.....	72
Figure 4.70. Calculated $n_I$ and $n_{II}$ values of Power law model for the suspensions of CT2 in ethylene glycol.....	73
Figure 4.71. Calculated $n_I$ and $K_I$ values of Power law model for the suspensions of CT2 in ethylene glycol.....	73
Figure 4.72. Calculated $n_{II}$ and $K_{II}$ values of Power law model for the suspensions of CT2 in ethylene glycol.....	74
Figure 4.73. Dynamic viscosity curves of the suspensions of CT2 in ethylene glycol at different solids contents (the solid lines represent modified cross model).....	75
Figure 4.74. Calculated $K_I$ and $K_{II}$ values of the modified Cross model for the suspensions of CT2 in ethylene glycol.....	76
Figure 4.75. Static viscosity curves of the suspensions of CT3 in ethylene glycol at different solids contents .....	76
Figure 4.76. Flow curves of the suspensions of CT3 in ethylene glycol at different solids contents.....	77
Figure 4.77. Dynamic viscosity curves of the suspensions CT3 in ethylene glycol at different solids contents.....	78
Figure 4.78. Flow curves of the suspensions of CT3 in ethylene glycol (the solid lines represent the power law model).....	79
Figure 4.79. Calculated $K_I$ and $K_{II}$ values of Power law model for the suspensions of CT3 in ethylene glycol.....	80
Figure 4.80. Calculated $n_I$ and $n_{II}$ values of Power law model for the suspensions of CT3 in ethylene glycol.....	80
Figure 4.81. Calculated $n_I$ and $K_I$ values of Power law model for the suspensions of CT3 in ethylene glycol.....	81

Figure 4.82. Calculated $n_{II}$ and $K_{II}$ values of Power law model for the suspensions of CT3 in ethylene glycol.....	81
Figure 4.83. Dynamic viscosity curves of the suspensions of CT3 in ethylene glycol at different solids contents (the solid lines represent modified cross model).....	82
Figure 4.84. Calculated $K_I$ and $K_{II}$ values of the modified Cross model for the suspensions of CT3 in ethylene glycol.....	83
Figure 4.85. Static viscosity curves of the suspensions of CT4 in ethylene glycol at different solids contents .....	83
Figure 4.86. Flow curves of the suspensions of CT4 in ethylene glycol at different solids contents.....	84
Figure 4.87. Dynamic viscosity curves of the suspensions of CT4 in ethylene glycol at different solids contents.....	85
Figure 4.88. Flow curves of the suspensions of CT4 in ethylene glycol at different solids contents (the solid lines represent the power law model).....	86
Figure 4.89. Calculated $K_I$ and $K_{II}$ values of the Power law for the suspensions of CT4 in ethylene glycol.....	87
Figure 4.90. Calculated $n_I$ and $n_{II}$ values of Power law for the suspension of CT4 in ethylene glycol.....	87
Figure 4.91. Calculated $n_I$ and $K_I$ values of Power law for the suspensions of CT4 in ethylene glycol.....	88
Figure 4.92. Calculated $n_{II}$ and $K_{II}$ values of Power law for the suspension of CT4 in ethylene glycol.....	88
Figure 4.93. Dynamic viscosity curves of the suspensions of CT4 in ethylene glycol (the solid lines represent the modified cross model).....	89
Figure 4.94. Calculated $K_I$ and $K_{II}$ values of the modified Cross model for the suspensions of CT4 in ethylene glycol.....	90
Figure 4.95. Comparison of $\eta_c$ values of the suspensions of TiO <sub>2</sub> powders at different solids contents .....	90
Figure 4.96. Comparison of $\gamma_c$ values of the suspensions of TiO <sub>2</sub> powders at different solids contents .....	91
Figure 4.97. Comparison of $\sigma_c$ values of the suspensions of TiO <sub>2</sub> powders at different solids contents.....	91
Figure 4.98. Comparison of $\eta_{max}$ values of the suspensions of TiO <sub>2</sub> powders at different solids contents.....	92

Figure 4.99. Comparison of $\sigma_{\max}$ values of the suspensions of TiO <sub>2</sub> powders at different solids contents.....	94
Figure 4.100. The SEM micrographs of SS1.....	93
Figure 4.101. Particle Size Distribution of SS1.....	94
Figure 4.102. The SEM micrographs of SS2.....	95
Figure 4.103. Particle Size Distribution of SS2.....	95
Figure 4.104. The SEM micrograph of SS3.....	96
Figure 4.105. Particle Size Distribution of SS3.....	96
Figure 4.106. The SEM micrograph of SS4.....	97
Figure 4.107. Particle Size Distribution of SS4.....	97
Figure 4.108. The SEM micrograph of SS5.....	98
Figure 4.109. Particle Size Distribution of SS5.....	98
Figure 4.110. Comparison of Particle Size Distribution of the synthesized silica particles.....	99
Figure 4.111. Relative high shear viscosity as a function of volume fraction of solids for the suspensions of SS3 in ethylene glycol.....	100
Figure 4.112. Static Viscosity curves of the suspensions of SS3 in ethylene glycol at different solids contents .....	100
Figure 4.113. Dynamic viscosity curves of the suspensions of SS3 in ethylene glycol at different solids contents .....	101
Figure 4.114. Flow curves of the suspensions of SS3 in ethylene glycol at different solids contents.....	102
Figure 4.115. Power law curve fitting for the suspensions of SS3 in ethylene glycol.....	103
Figure 4.116. Modified Cross model curve fitting for the suspension of SS3 in ethylene glycol.....	103
Figure 4.117. Amp- sweep tests of 20 vol% suspensions of SS3 in ethylene glycol suspension.....	104
Figure 4.118. Freq-sweep graph of 20 vol% suspensions of SS3 in ethylene glycol.....	105
Figure 4.119. Amp-sweep graph of 30 vol% suspensions of SS3 in ethylene glycol.....	105

Figure 4.120. Freq-sweep graph of 30 vol% suspensions of SS3 in ethylene glycol.....	106
Figure 4.121. Amp-sweep graph of 40 vol% suspensions of SS3 in ethylene glycol.....	106
Figure 4.122. Freq-sweep graph of 40 vol% suspensions of in ethylene glycol.....	107
Figure 4.123. Amp-sweep graph of 45 vol% suspensions of SS3 in ethylene glycol.....	107
Figure 4.124. Freq-sweep graph of 45 vol% suspensions of SS3 in ethylene glycol.....	108
Figure 4.125. Amp-sweep graph of 47 vol% suspensions of SS3 in ethylene glycol.....	108
Figure 4.126. Freq-sweep graph of 47 vol% suspensions of SS3 in ethylene glycol.....	109
Figure 4.127. The SEM micrographs of AL1.....	110
Figure 4.128. Particle Size Distribution of AL1.....	110
Figure 4.129. The SEM micrographs of AL2.....	110
Figure 4.130. Particle Size Distribution of AL2.....	111
Figure 4.131. Dynamic viscosity curves of the suspensions of AL1 in ethylene glycol at different solids contents in ethylene glycol.....	112
Figure 4.132. Flow curves of the suspensions of AL1 in ethylene glycol at different solids contents.....	112
Figure 4.133. Dynamic viscosity curves of the suspensions of AL2 in ethylene glycol at different solids contents .....	113
Figure 4.134. Flow curves of the suspensions of AL2 in ethylene glycol at different solids contents .....	113
Figure 4.135. The SEM micrographs of zirconia.....	114
Figure 4.136. Dynamic viscosity curves of the suspensions of zirconia in ethylene glycol at different solids contents.....	115
Figure 4.137. Flow curves of the suspensions of zirconia in ethylene glycol at different solids conents.....	115

## LIST OF SYMBOLS

$G$	relaxation modulus/shear modulus
$G'$	elastic/storage modulus
$G''$	viscous/loss modulus
$K$	the consistency index
$n$	flow index
$a$	particle radius
Pe	Peclet number
S	shear stress
sec	second
SEM	scanning electron microscope
XRD	x-ray diffraction
TGA	thermal gravimetric analysis
W	weight percentage
$I$	intensity
$k_F$	forward reaction rate
GNF	generalized newtonian fluid

### *Greek Letters*

$\Phi$	volume fraction
$\Phi_{\max}$	maximum-packing volume fraction
$\dot{\gamma}$	shear rate
$\dot{\gamma}_c$	critical shear rate
$\dot{\gamma}_0$	applied strain (constant)
$\dot{\gamma}_{\max}$	maximum shear rate
$\bar{\bar{\gamma}}$	shear rate tensor
$\eta$	viscosity
$\eta_s$	viscosity of the pure liquid
$\eta_r$	relative viscosity
$\eta_0$	zero shear viscosity

$\eta_{\infty}$	infinite shear viscoisty
$\eta^*$	complex (dynamic) viscosity
$\eta_c$	critical viscosity
$\eta_{\max}$	maximum viscosity
$\sigma$	shear stress
$\sigma_c$	critical shear stress
$\omega$	radial frequency
$\delta$	the phase angle
$\theta$	Bragg diffraction angle
$\tau$	shear stres
$\bar{\tau}$	shear stres tensor

# CHAPTER 1

## INTRODUCTION

The interest towards suspension rheology has been increasing over the last few decades. The development of suitable tools to study the complex and variable microstructure of flowing dispersions as well as the growing popularity of nanoparticles and nanocomposites have contributed significantly to the current rheological research. The suspension and nanoparticle dispersion rheology have been investigated by various scientific disciplines each of which brings distinct viewpoints and methods towards a better suspension behaviour understanding. The complex rheological behaviour of suspensions is strongly affected by the nature of the micro/nanostructure and the interparticle forces by which it is controlled (Mewis and Wagner, 2009).

Many industrially important processes depend on the flow of fluids containing particulates. Minerals processing and tailings disposal, the forming of ceramic components, pumping of coal–water mixtures, concrete structure construction and pharmaceutical production are some of these processes. Shear thickening is the phenomena in which the viscosity of the suspension increases with increasing shear rate which is usually undesirable in industry. A fundamental understanding of the process of shear thickening of particulate suspensions may provide clues for a strategy towards minimization of the problems in industry (Franks et al., 2000; Barnes, 1989)

“Smart Fluids” is a generic term for any particle-filled, fluid-based suspension that changes its consistency in a magnetic, electric, shear or light-field. They sense and respond to the environment. Smart fluids can be classified as shear thickening fluids, electro-rheological fluids, magneto-rheological and photo-rheological fluids. Shear-thickening fluids (STFs) which are a sub-group of smart fluids certainly spark the curiosity of scientists, especially in damping and energy-absorption applications. Shear thickening fluids are used in drilling to protect a well from blow outs and they are also used as flexible-body armour which would solidify at the point of a ballistic impact causing resistance to rupture. STFs can function in an energy or communication transmission cable to provide enhanced protection against externally applied forces like

damage or puncture from a shovel. Researchers have also explored the STFs response in sporting equipment and automotive applications, such as skis and tennis rackets that efficiently dissipate vibrations without losing stiffness. STFs embedded in a passenger compartment liner can be designed to protect passengers in a car accident (Wagner and Brady, 2009).

The purpose of this thesis was to prepare concentrated suspensions of carbonate and oxide submicron/nano particles dispersed in non-aqueous media for energy-absorption applications, investigate their rheological behaviour and analyse the fit of the data to various shear-thickening fluid models.

## CHAPTER 2

# RHEOLOGICAL BEHAVIOUR OF COLLOIDAL SUSPENSIONS

### 2.1. Shear Thinning

Shear-thinning behaviour is very common in polymer solutions, polymer melts, paints, glues, as well as toiletry products. These materials may exhibit three distinct flow regions as seen in Figure 2.1. The limiting apparent viscosity at zero shear rate ( $\eta_0$ ) stays constant with respect to shear rate in the lower Newtonian region. The apparent viscosity ( $\eta$ ) decreases with shear rate in the middle region where the power law equation is a suitable model. The slope of the curve which is called the limiting viscosity at infinite shear rate ( $\eta_\infty$ ) is constant with changing shear rates in the upper Newtonian region (Barnes, 1989).

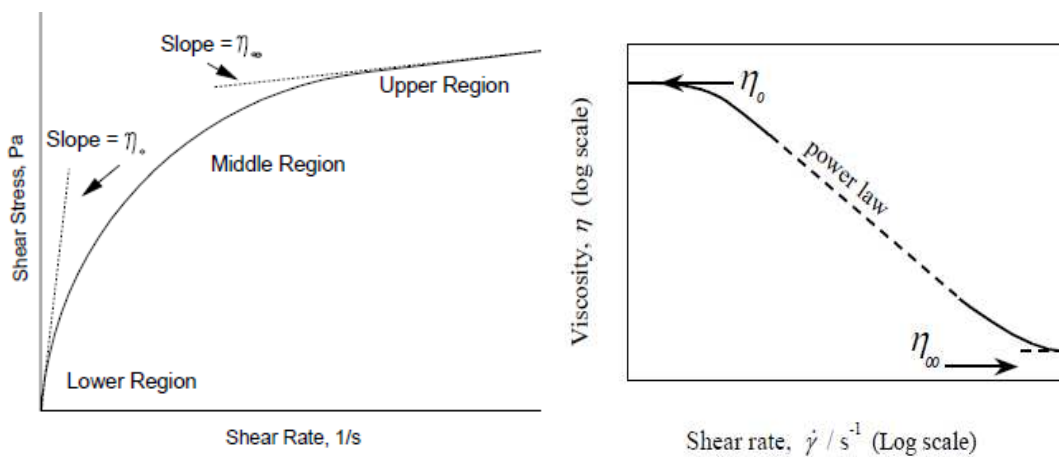


Figure 2.1. Rheogram of idealized shear-thinning (pseudoplastic) behaviour (Source: Steffe, 1996).

The schematic representation of suspensions at rest and flowing through a tube is shown in Figure 2.2 (Schramm, 1998). Particles in whisker like morphology suspended in a liquid align lengthwise in the direction of the flow with increasing shear

rates. Chain-type molecules in a melt or in a solution can disentangle, stretch and orient themselves parallel to the flow direction. Particle or molecular alignments allow particles and molecules to slip past each other more easily. Sphere-shaped particles may be deformed to a “Rugby or American Football ball” shape becoming smaller in diameter but longer. Elastically deformable corpuscular cells with a coin-like shape such as red blood cells suspended in plasma may be reshaped to long thinbles with reduced diameters causing an easier passage through small blood vessels and a higher flow rate. Shear can also induce irregular lumps of aggregated primary filler particles to break up and this can help a suspension with broken-up filler aggregates to flow faster at a given shear stress.

The shear-thinning effect is often reversible with some time lag for most of the fluids. The liquids regain their original high viscosity when the applied shear stress is decreased or finally removed. The chain-type molecules return to their natural state of non-orientation, deformed droplets return to their original ball-shape and the aggregates reform due to Brownian motion (Schramm, 1998).

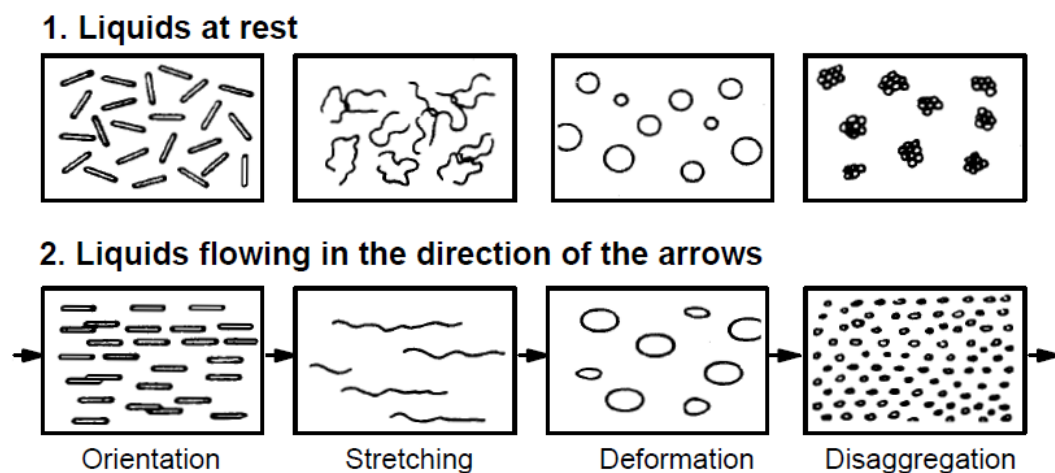


Figure 2.2. Dispersions at rest and flowing through a tube  
(Source: Schramm, 1998)

The stripping of solvent layers from dissolved molecules or particle surfaces and the reduction of the intermolecular interactions causing resistance to flow is reported to be another possible explanation for the shear-thinning behaviour of a suspension in the rheological literature (Schramm, 1998).

## 2.2. Shear Thickening

Shear-thickening is specific to non-Newtonian fluids and implies that the viscosity of a fluid increases with increasing shear rate. This phenomenon although the increase can be gradual finally leads to a discontinuous jump in the viscosity. All kinds of suspensions of solid particles in a fluid show this phenomenon (Wagner and Brady, 2009). The viscosity of a shear-thickening suspension is dependent on the degree of shear stress. The flow curve has an increasing slope and  $\eta$  increases with increasing shear stress as seen in Figure 2.3. This behaviour is almost immediately reversible in suspensions. The viscosity instantly decreases as soon as the shear rate is decreased (Barnes, 1989).

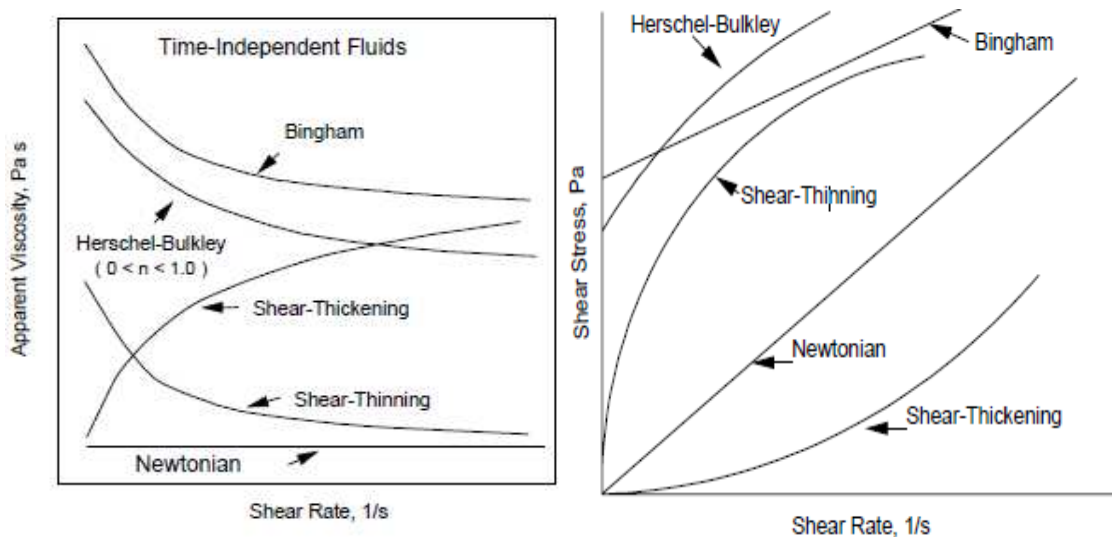


Figure 2.3. Apparent viscosity and flow curves for typical time-independent fluids (Source: Steffe, 1996).

Dispersions with a high concentration of solids or polymers; such as ceramic suspensions, starch dispersions, plastisol pastes (with insufficient softener content) are examples of shear-thickening fluids (Mezger, 2002).

Shear thickening materials are much less common in industrial practice compared to shear-thinning materials. Shear-thickening behaviour is desirable for special applications on the other hand and is therefore encouraged in these cases. It is usually undesirable and should never be ignored because this can lead to enormous

technical problems and in some cases destruction of equipment, e.g. pumps or stirrers (Mezger, 2002).

Shear-thickening systems usually have a high but finite viscosity at zero shear rate. Pseudoplastic liquids have a defined viscosity ( $\eta_0$ ) independent of shear rate which is called the “zero shear viscosity” and they behave similar to Newtonian liquids at very low shear rates (Schramm, 1998). The viscosity ( $\eta$ ) of a suspension of hard spheres can be predicted by Einstein’s formula at very low volume fractions ( $\Phi \leq 0.03$ ), where  $\eta_s$  is the viscosity of the pure liquid:

$$\eta = \eta_s(1 + 2.5\phi) \quad (2.1)$$

Einstein calculated this formula from the viscous dissipation produced by the flow around a single sphere. Therefore, Einstein’s formula as seen in Equation 2.1 is merely valid for the suspensions at low solids contents so that the flow field around one sphere is not considerably influenced by neighbour spheres (Larson, 1999).

The viscosity decreases with increasing shear rate at low shear rates. The viscosity starts to increase above a critical value of shear rate  $\dot{\gamma}_c$  (Barnes, 1989). Shear-thickening behaviour is not observed sometimes unless higher shear rates are applied, e.g. at  $\dot{\gamma} > 1000 \text{ sec}^{-1}$  for highly concentrated dispersions. The viscosity curve of a suspension is presented in Figure 2.4. which displays shear-thinning behaviour up to medium shear rates and then shows a “dilatant peak” at high shear rates (Mezger, 2002). The fracture of the sample occurs or the viscosity begins to decrease after this shear-thickening region.

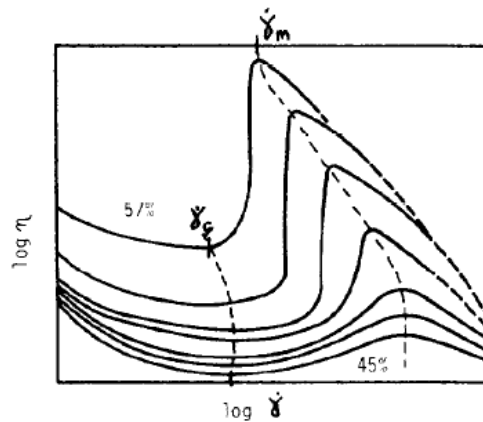


Figure 2.4. The schematic representation of viscosity versus shear rate for shear thickening systems at different solids contents (Source: Barnes, 1989).

Shear thickening behaviour was extensively used to define a ‘‘well-behaved’’ rise in viscosity with increasing shear rate until Hoffman (1972) reported that highly concentrated suspensions of monodispersed particles indeed exhibit a discontinuous jump in viscosity at some critical shear rate. Hoffman observed that monodispersed suspensions under shear display diffraction patterns, which change with the onset of shear thickening. He was able to show that layers of particles, packed in a two dimensional hexagonal packing at low rates of shear, break up into less ordered arrays in the region of shear thickening by using these patterns. Each layer of particles is parallel to surfaces of constant shear, and one axis of the packing always points in the direction of flow in most viscometric flows. Hoffman suggested that instability in flow caused the particles to break out of their ordered layers at some critical level of shear stress and jam into one another, thereby causing a rise in viscosity with the help of these deductions (Hoffman 1998).

The Hoffman’s order-to-disorder transition theory leads to a more ‘fluid-like’ state when shear thickening occurs. At sufficiently high shear rates the structures deteriorate because some of the particles are pushed out of the layered sheets or strings due to hydrodynamic instabilities and interact more strongly with particles in adjacent layers. In this scenario the flow becomes less efficient and the viscosity begins to increase without increase in the volume of the suspension.

Brady and co-workers simulated the flow behaviour of concentrated suspensions by Stokesian dynamics. Investigating moderate density charge stabilized suspensions by this approach, Brady and Bossis (1985, 1988) found that the model predicts shear thickening without layering, and the cause of shear thickening appears to be cluster formation. These clusters are composed of compact groups of particles formed when shear forces drive particles into close contact. Under these conditions, short range lubrication forces cause the increase in viscosity with increasing shear as the clusters become larger and larger. This explanation for shear thickening dates back to Krut (1952). Bossis and Brady (1989) and Phung and Brady (1992) obtained similar results when modelling the behaviour of hard-sphere suspensions (Hoffman, 1998).

The parameters that control shear-thickening behaviour are the particle size distribution, phase volume, particle shape, interaction with other particles, the continuous phase viscosity, type of deformation experienced by the particles of the

suspension (shear or extension, steady or unsteady), flow field rate and deformation time (Barnes, 1989).

The shear-thickening initiation was reported to be around 50% solids content by volume in the pioneering research papers. The effect of solids volume content is presented in Figure 2.5. The critical shear rate where the onset of shear thickening is observed increases rapidly if the solids volume content is much less than 50%. If the phase volume content is significantly greater than 50% the critical shear rate decreases rapidly.

Dimensional analysis implies that for a given value of  $\Phi$ , all monodisperse hard-sphere suspensions ought to show an onset of shear-thickening at a universal value of the Peclet number  $Pe$ , or reduced stress  $\sigma_r$ . Thus, the critical shear rate  $\dot{\gamma}_c$  for shear-thickening ought to be proportional to the inverse cube of the particle radius,  $\dot{\gamma}_c \propto a^{-3}$ . A compilation of data for a wide range of sterically or electrostatically stabilized suspensions of spheres with diameters from 0.03 to 100  $\mu\text{m}$  show a scaling law that deviates somewhat from this ( $\dot{\gamma}_c \propto a^{-2}$ ) (Barnes 1989). A plot of the onset of shear thickening with particle size for systems with a nominal particle phase volume content of 50% in Figure 2.6. As the particle size decreases, the critical shear value increases (Hoffman, 1998). The systematic deviation from the expected scaling law probably arises from deviations from a hard-sphere repulsive potential; since “softness” caused by electrostatic charges or deformability of the steric stabilizing layer is generally more important for small particles than large ones, a deviation toward a weaker power law should be expected (Larson, 1999).

Broadening of a continuous particle size distribution also increases  $\Phi_m$ . This in turn increases the critical shear rate ( $\dot{\gamma}_c$ ). The dispersions of polydispersed particles will exhibit a pronounced shear thickening under applied stress. The increase in viscosity with shear will be far less dramatic than with monodisperse particles (Hoffman, 1998).

Clarke’s study of shape showed that it can profoundly influence the flow of large particle size suspensions with rods having a greater effect than plates as seen in Figure 2.7. It is difficult to draw any quantitative conclusions from his work because he did not study the effect over a wide range of size, shape, phase volume, and shear-rate.

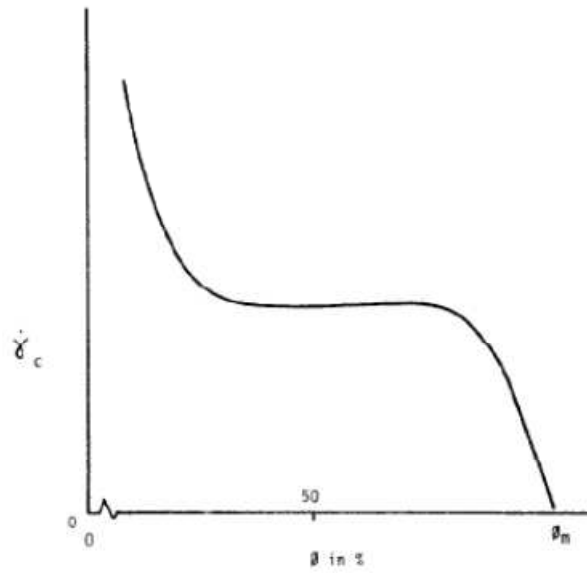


Figure 2.5. The dependence of the critical shear rate for the onset of shear thickening as a function of phase volume content of the dispersed phase (Source: Barnes, 1989).

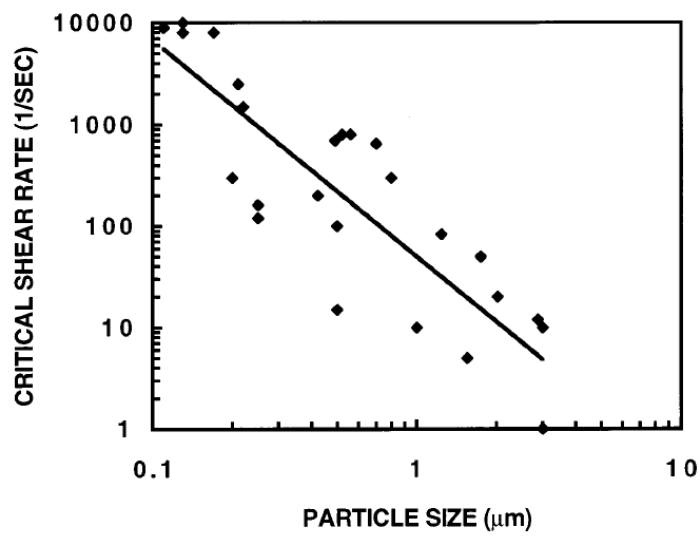


Figure 2.6. Effect of particle size on the critical shear rate at which shear thickening is initiated (Source: Hoffman, 1998).

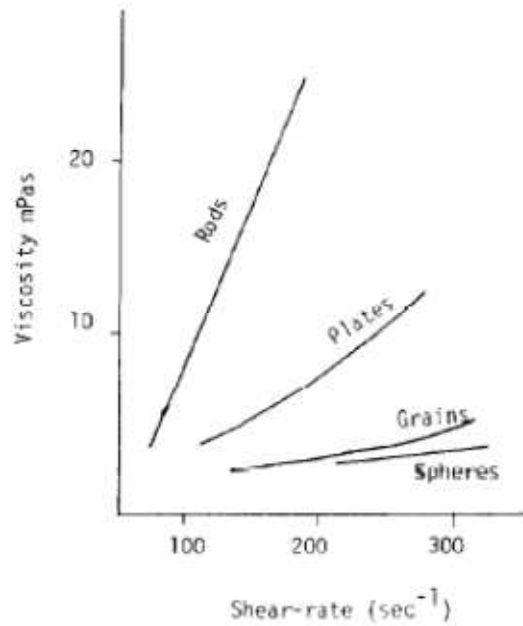


Figure 2.7. The effect of shape on shear thickening for  $\Phi=0.2$  (Source: Barnes, 1989).

### 2.3. Viscoelasticity

Many materials can be readily classified as solids or fluids, exhibiting elastic and viscous behaviour, respectively. The decision about whether a material is a solid or a liquid should be given after observations conducted over time. Lead which is used as a roofing material for churches in the past can be given as an example. Lead is a metallic solid; however, it has some fluid-like properties and will creep and flow under its own weight, which happens slowly over many years. If a roof is pitched too steeply, it could even slip completely off eventually. The timescale of the measurement relative to the characteristic time of the material should be taken into consideration when a classification of materials is done. The ratio of these times is given by the Deborah number in the Equation 2.2:

$$D_e = \text{stress relaxation time} / \text{observation time} \quad (2.2)$$

The material behaviour can be classified into three categories by Deborah number:  $D_e \gg 1$  for solid-like materials,  $D_e \sim 0(1)$  for viscoelastic materials and  $D_e \ll 1$  for liquid-like materials. The material displays both viscous and elastic behaviour

(viscoelastic) when the Deborah number is of the order of 1 (Goodwin and Hughes, 2000).

When a viscoelastic material is placed under load, the deformation is composed of two portions: the first part occurs immediately and the second part occurs only after a certain time delay. After the load has been removed, either a delayed partial or a delayed complete reformation takes place (Mezger, 2002). In linear viscoelastic region the ratio of maximum stress to the maximum strain is constant. This behaviour will be observed when the stress is applied to a Hookean spring or a dashpot containing Newtonian oil. Hookean deformation behaviour is formally described using Hooke's law:

$$\sigma = G \cdot \gamma \quad (2.3)$$

The constant of proportionality is the shear viscosity in the constitutive equation as seen in Equation 2.4.

$$\sigma = \eta \dot{\gamma} \quad (2.4)$$

There are two simple arrangements that these models can be combined: in series or parallel. Maxwell and Kelvin models are obtained respectively when they are placed in series and parallel. If a stress is applied to the parallel elements of a Kelvin model, both elements will respond. Thus a linear addition of the stresses describes the constitutive Equation 2.5:

$$\sigma = G\gamma + \eta\dot{\gamma} \quad (2.5)$$

For a Maxwell model it is the strain rates that linearly add:

$$\dot{\gamma} = \frac{\dot{\sigma}}{G} + \frac{\sigma}{\eta} \quad (2.6)$$

Both of these models display contributions from the viscosity and elasticity, and so both show viscoelastic behaviour.

The basic principle of an oscillatory rheometer is to induce a sinusoidal shear deformation in the sample and measure the resultant stress response; the time scale probed is determined by the frequency of oscillation ( $\omega$ ) of the shear deformation. The

sample is placed between two plates, as shown in Figure 2.8(a) in a typical experiment. While the top plate remains stationary, a motor rotates the bottom plate, thereby imposing a time dependent strain  $\gamma(t)=\gamma \cdot \sin(\omega t)$  on the sample. Simultaneously, the time dependent stress  $\sigma(t)$  is quantified by measuring the torque that the sample imposes on the top plate.

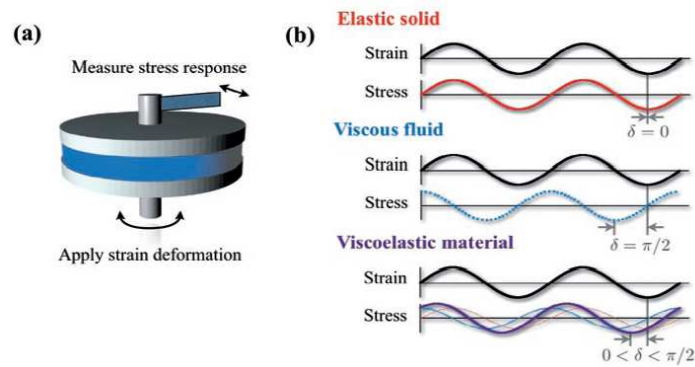


Figure 2.8. (a) Schematic representation of a typical rheometry setup, with the sample placed between two plates. (b) Schematic representation of stress response to oscillatory strain deformation for an elastic solid, a viscous fluid and a viscoelastic material (Source: Weitz et al., 2007).

The main differences between materials can be revealed by measuring the time dependent stress response at a single frequency as shown schematically in Figure 2.8(b). If the material is an ideal elastic solid, then the sample stress is proportional to the strain deformation, and the proportionality constant is the shear modulus of the material. The stress is always absolutely in phase with the applied sinusoidal strain deformation. In contrast, the stress in the sample is proportional to the rate of strain deformation, where the proportionality constant is the viscosity of the fluid if the material is a purely viscous fluid. The applied strain and the measured stress are out of phase, with a phase angle  $\delta=\pi/2$ , as shown in the center graph in Figure 2.8(b).

Viscoelastic materials show a response that contains both in-phase and out-of-phase contributions, as shown in the bottom graph of Figure 2.8(b); these contributions reveal the extents of solid-like (red line) and liquid-like (blue dotted line) behavior. As a consequence, the total stress response (purple line) shows a phase shift  $\delta$  with respect to the applied strain deformation that lies between that of solids and liquids,  $0 < \delta < \pi/2$ . The viscoelastic behaviour of the system at  $\omega$  is characterised by the storage modulus,  $G'(\omega)$ , and the loss modulus,  $G''(\omega)$ ,

which respectively characterise the solid-like and fluid-like contributions to the measured stress response. For a sinusoidal strain deformation  $\gamma(t) = \gamma_0 \sin(\omega t)$ , the stress response of a viscoelastic material is given by  $\sigma(t) = G'(\omega)\gamma_0 \sin(\omega t) + G''(\omega)\gamma_0 \cos(\omega t)$ .

In a typical rheological experiment,  $G'(\omega)$  and  $G''(\omega)$  are desired to be measured. The measurements are made as a function of  $\omega$  because the solid-like or liquid-like property of a soft material depends on the time scale at which it is deformed. The plot of  $G'(\omega)$  and  $G''(\omega)$  for a suspension of hydrogel particles is a typical example displayed in Figure 2.9(a) (Weitz et al., 2007). The response is viscous-like at the lowest accessible frequencies, with a loss modulus that is much larger than the storage modulus while the storage modulus dominates the response at the highest frequencies, indicating solid-like behaviour.

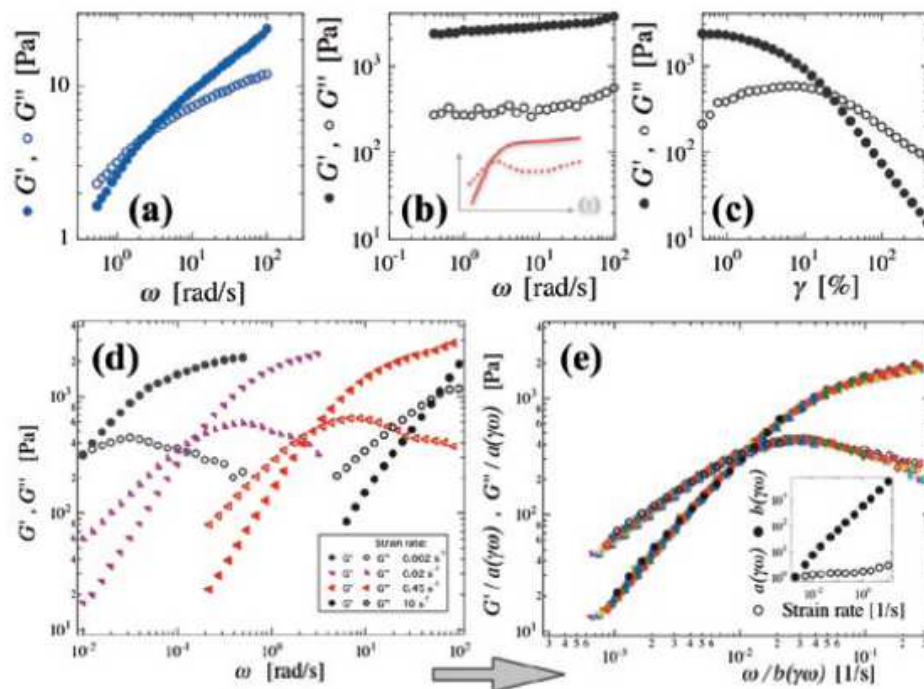


Figure 2.9. Frequency dependence of  $G'$  and  $G''$  for (a) a suspension of hydrogel particles and (b) for the elastomer blend Further measurements of DC-9040: (c) Strain dependence of  $G'$  and  $G''$ , (d) Constant-rate measurements at strain rates 0.002 s<sup>-1</sup>, 0.02 s<sup>-1</sup>, 0.45 s<sup>-1</sup> and 10 s<sup>-1</sup>, (e) master curve of constant-rate measurements that were scaled both in magnitude and frequency (Source: Weitz et al., 2007).

## 2.4. Rheological Models of Shear-Thickening Fluids

### 2.4.1. Ostwald / de Waele (Power Law)

For substances which show a negligible yield value ( $S_0 \rightarrow 0$ ) but a varying differential viscosity, it is often possible to represent the behaviour by a power law relation known as the Ostwald-de Waele model. The dependence of shear stress,  $S$  on  $\dot{\gamma}$  is represented by Equation 2.7.

$$S = K\dot{\gamma}^n \quad (2.7)$$

where  $S$  refers to shear stress and  $K$  and  $n$  are the empirical parameters.

$$\eta_I(I_{2,\dot{\gamma}}) = K|I_{2,\dot{\gamma}}|^{\frac{n-1}{2}} \quad (2.8)$$

$$\tau = K|I_{2,\dot{\gamma}}|^{(n-1)/2} \dot{\gamma} \quad (2.9)$$

In steady, unidirectional shear flows  $|I_{2,\dot{\gamma}}| = \dot{\gamma}^2$ , and the constitutive equation is reduced to

$$\tau_{ij} = (K\dot{\gamma}^{n-1})\dot{\gamma}_{ij} = K\dot{\gamma}_{ij}^n \quad (2.10)$$

with the apparent viscosity given by Equation 2.11

$$\eta = K\dot{\gamma}^{n-1} \quad (2.11)$$

The viscosity index  $n$  is less than one in shear-thinning fluids, also called pseudoplastic fluids; whereas, it is greater than one in shear thickening or dilatant fluids.  $K$ , the consistency, is the value of the shear stress when  $\dot{\gamma}_c = 1$ . The model becomes identical to Newton's model when the viscosity index is equal to one. The power-law model is widely used for medium range of shear rates. In processes covering a wide range of shear rates the model is unable to converge to steady-state values at the limits (Hunter, 2001; Peker and Helvacı, 2008).

## 2.4.2. Modified Cross-Model for Shear-Thickening Fluids

Galindo-Rosales et al. proposed a viscosity function for shear thickening behaviour able to cover the three regions characteristic of the general viscosity curve exhibited by shear thickening fluids. The proposed viscosity function could be used, for instance, to perform numerical simulations of steady flows involving STFs together with the Generalized Newtonian Fluid constitutive equation (Galindo-Rosales et al., 2011).

A Generalized Newtonian Fluid (GNF) is an idealized incompressible fluid, whose viscosity is a function of the instantaneous shear rate, but not dependent upon the history of deformation. GNF constitutive equation is developed from the Newtonian constitutive equation for incompressible fluids. (see Equation 2.11) However the viscosity is not constant in this case, so the Equation 2.11 becomes Equation 2.12.

$$\bar{\tau} = \mu \bar{\dot{\gamma}} \quad (2.11)$$

$$\bar{\tau} = \eta(\dot{\gamma}) \bar{\dot{\gamma}} \quad (2.12)$$

In Equation 2.8  $\bar{\tau}$  is the shear stress tensor,  $\bar{\dot{\gamma}} = \nabla \vec{v} + (\nabla \vec{v})^T$  is the shear rate tensor,  $\eta(\dot{\gamma})$  is a scalar function, and  $\dot{\gamma} = |\bar{\dot{\gamma}}| = \sqrt{II_{\bar{\dot{\gamma}}}/2}$ . The GNF constitutive equation is also quite general, since the functional form of  $\eta(\dot{\gamma})$  can be adapted to fit the specific non-Newtonian behaviour of the system under study.

The non-newtonian behaviour can simply be analysed in three different regions. A slight shear thinning behaviour up to a critical shear rate exists in zone I, shear thickening takes place between  $\gamma_c$  and a higher critical value  $\gamma_{max}$  where the apparent viscosity takes its maximum value in zone II and finally zone III is characterised by a steep shear thinning behaviour for values of  $\gamma > \gamma_{max}$ . Therefore, a simple way of building a function valid for the whole viscosity curve of a shear thickening fluid consists in using a piecewise definition, taking the three different regions into account separately. Thus, the function can be stated as follows

$$\eta(\dot{\gamma}) = \begin{cases} \eta_I(\dot{\gamma}) & \text{for } \dot{\gamma} \leq \dot{\gamma}_C \\ \eta_{II}(\dot{\gamma}) & \text{for } \dot{\gamma}_C < \dot{\gamma} \leq \dot{\gamma}_{max} \\ \eta_{III}(\dot{\gamma}) & \text{for } \dot{\gamma}_{max} < \dot{\gamma} \end{cases} \quad (2.13)$$

where  $\eta_i(\dot{\gamma})$  is the viscosity function that fits the zone of the general viscosity curve (i representing zones I, II, and III). The functions  $\eta_i(\dot{\gamma})$  following the model of Cross was developed as:

$$\eta(\dot{\gamma}) = \eta_\infty + \frac{\eta_0 - \eta_\infty}{1 + (K\dot{\gamma})^n} \quad (2.14)$$

$$\eta(\dot{\gamma}) = \begin{cases} \eta_I(\dot{\gamma}) = \eta_C + \frac{\eta_0 - \eta_C}{1 + [K_I(\dot{\gamma}^2 / (\dot{\gamma} - \dot{\gamma}_C))]^{n_I}} & \text{for } \dot{\gamma} \leq \dot{\gamma}_C \\ \eta_{II}(\dot{\gamma}) = \eta_{max} + \frac{\eta_C - \eta_{max}}{1 + [K_{II}((\dot{\gamma} - \dot{\gamma}_C) / (\dot{\gamma} - \dot{\gamma}_{max}))\dot{\gamma}]^{n_{II}}} & \text{for } \dot{\gamma}_C < \dot{\gamma} \leq \dot{\gamma}_{max} \\ \eta_{III}(\dot{\gamma}) = \frac{\eta_{max}}{1 + [K_{III}(\dot{\gamma} - \dot{\gamma}_{max})]^{n_{III}}} & \text{for } \dot{\gamma}_{max} < \dot{\gamma} \end{cases} \quad (2.15)$$

## 2.5. Recent Studies on the Rheological Behaviour of Colloidal Suspensions

A viscosity function for shear thickening fluids has been proposed by Galindo-Rosales et al. (2011). It is convenient to use this model both in numerical simulations and curve-fitting procedure, because it has a continuous derivative. The three characteristic regions present in the typical viscosity curves of shear thickening fluids can be represented by the function that they have proposed. Moreover, it also contemplates other particular cases where one of the shear thinning regions is absent. The accuracy and robustness of the fitting seems to be controlled by the quality of the experimental data set, and does not depend on the nature of the fluid.

Bergström (1998) studied the steady shear properties of the concentrated stable colloidal suspensions of ceramic powders and whiskers. In his study the non-aqueous powder suspensions all displayed a shear thinning behaviour, which was modelled by the high shear form of the Cross equation. Also the volume fraction dependence of the high shear viscosity was fitted to a modified Krieger-Dougherty model.

Chadwick et al. (2002) investigated the rheological properties of dispersions of particles of uncoated commercial anatase in ethylene glycol. The samples exhibited

shear thickening behaviour between  $\Phi=0.30-0.33$ . The  $\Phi_{\max}$  was found as 0.6, through adaptation of the Krieger–Dougherty equation and application of viscosity data.

The rheological behaviour of titanium dioxide (rutile) suspensions has been investigated under steady shear conditions in order to study the influence of dispersed phase content by Zupancic et al. (1997). The onset of shear thickening behaviour was observed in the highest shear stress region at solids volume fraction higher than 0.20. A satisfactory fitting of both shear-thinning and shear-thickening behaviour is given for those suspensions examined by modified versions of the Krieger- Dougherty and Cross equations.

Morris et al. (1999) showed that the rheological properties of aqueous coated titania pigment suspensions were strongly affected by pH and chemical surface coating composition and the suspensions exhibited shear-thinning behaviour.

Wagner et al. (2003) reported the ballistic penetration performance of a composite material composed of woven Kevlar fabric impregnated with a colloidal shear thickening fluid (silica particles (450 nm) dispersed in ethylene glycol which were synthesized by Stöber method. The results demonstrated a significant enhancement in ballistic penetration resistance due to the addition of shear thickening fluid to the fabric, without any loss in material flexibility. Then Wagner et al. (2007) also used PMMA particles, which were softer than silica particles and the shear-thickening fluid was applied to the Kevlar fabric for energy absorption tests. The PMMA-STF exhibited a post-thickening behaviour different from the silica sphere suspensions.

Galindo-Rosales et al. (2009) have investigated the rheological behaviour of fumed-silica in polypropylene glycol of two different molecular weights. They have prepared 10% (w/w) nonfloculated colloidal suspensions which exhibited reversible-shear-thickening.

Rangari et al. (2010) have prepared shear thickening fluids of silica nanoparticles (15 and 200 nm) in PEG by high intensity ultrasonic irradiation for liquid body armor applications. The weight fractions of 15 and 200 nm silica particles were 38-55% and 40-52% respectively. They have reported that the onset of sheartickening of 15 nm particles was lower than 200 nm particles.

Wagner et al. (2006) also have studied Rheo-SANS investigations of particle alignment in systems of dilute and concentrated acicular particle PCC (precipitated calcium carbonate)/PEG suspensions, which demonstrated that particle flow alignment

under shear was clearly influenced by average particle aspect ratio, particle loading, and shear rate. The results supported a hydrocluster-type mechanism for shear thickening.

## CHAPTER 3

### EXPERIMENTAL STUDY

#### 3.1. Preparation of Calcium Carbonate Particles

The calcium carbonate particles were obtained by two different methods. First one is the synthesis of  $\text{CaCO}_3$  particles by carbonation route. Secondly, the natural  $\text{CaCO}_3$  particles were grinded with zirconia beads.

##### 3.1.1. $\text{CaCO}_3$ Synthesis by $\text{CO}_2$ Bubbling Method

The experimental setup for the synthesis of  $\text{CaCO}_3$  particles is shown in Figure 3.1. To begin with a ceramic gas diffuser was prepared in order to diffuse  $\text{CO}_2$  gas bubbles into the reaction solution. Alumina and corn starch were added into water. The corn starch was used as a pore maker. The volume ratios of alumina, corn starch and water were 42 : 20 : 38 respectively. Dispersant (hydropalat) was used to obtain a well-dispersed suspension. Then this suspension was poured into the cylinders which were made from paper. After waiting for one night for letting the water in the suspension evaporate, the cylinders were put into oven (Carbolite RHF1600). Initially the temperature of the oven was increased incrementally by  $2^\circ\text{C}$  up to  $500^\circ\text{C}$  in order to get rid of the starch. Afterwards, it was raised to  $1325^\circ\text{C}$  and held on at that temperature for two hours. Finally, it was cooled to room temperature (Gregorova and Pabst, 2007).

After preparing the ceramic gas diffuser, the slurry of 1% (wt) slaked lime was prepared in ultrapure water. After being filtered through a 200-mesh sieve, the slurry was stirred during one hour. Next, the  $\text{CO}_2$  gas was bubbled into the slurry at a flow rate of  $1 \text{ dm}^3/\text{min}$ . The reaction was carried out at room temperature. The reaction was controlled by pH value of the medium. The reaction was stopped when the final pH value of the suspension reached about 7. The precipitated  $\text{CaCO}_3$  was centrifuged and

rinsed with deionized water. It was further dried at 120 °C for 8 hours in an oven (Wang et al., 2006).

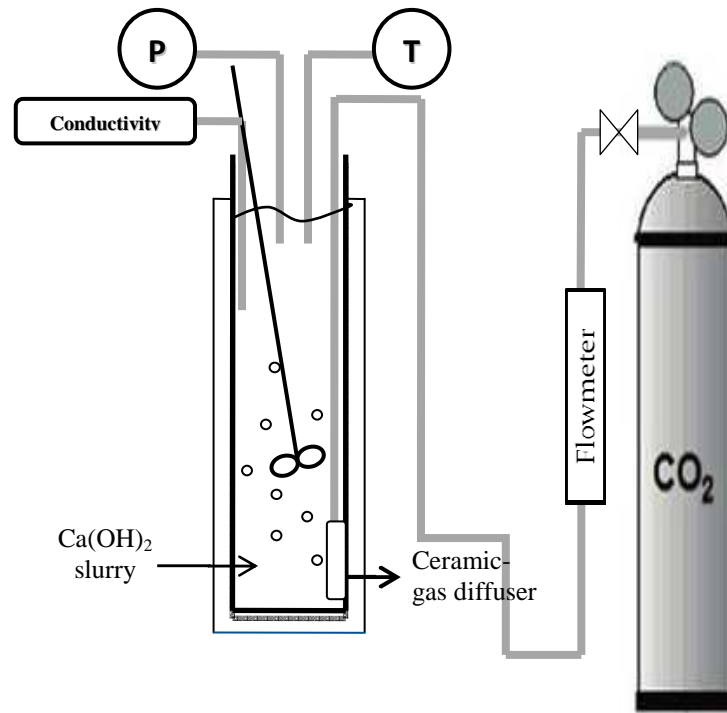


Figure 3.1. Experimental setup for the carbonation experiment.

### 3.1.1. Ballmilling of $\text{CaCO}_3$

Retsch PM 100 ballmill was used for grinding natural  $\text{CaCO}_3$  particles in order to reduce size. Two ballmilling processes were done.

#### 3.1.1.1. Ball1

A slurry of 30% wt natural  $\text{CaCO}_3$  (ground calcium carbonate) particles were prepared in deionized water. The total volume of the slurry was 150 ml. Then they were ballmilled with zirconia beads with the size of 2 mm (200 g) and 10 mm (98 g) during 5 hours at 650 rpm with an inverse rotation in between 5 minute intervals. Surfactant was not used in this grinding experiment. The suspension was centrifuged at 7000 rpm and washed with ethanol. Next, it was left at 40°C in the etuve for one night for drying.

### 3.1.1.2. Ball2

A slurry of 15% wt natural  $\text{CaCO}_3$  (ground calcium carbonate) particles in deionized water was prepared. The total volume of the slurry was 150 ml. Darvan 811 (sodium polyacrylate) was used as a surfactant and its concentration was 2% wt. The slurry was first ballmilled with zirconia beads with the size of 2 mm (200 g) and 10 mm (98 g) during 5 hours at 650 rpm with an inverse rotation in between 5 minute intervals.. After ballmilling with 2 mm and 10 mm zirconia beads, it was changed with the zirconia beads of 50  $\mu\text{m}$  and ballmilled for 9 hours. The suspension was centrifuged at 7000 rpm and washed with deionized water and ethanol. Next, it was left at 40°C in the etuve for one night for drying (Frances et al., 2004; Jang et al., 2009; Inam et al., 2011).

### 3.2. Synthesis of Silica Particles

Silica spheres were synthesized by controlled hydrolysis and condensation reactions of Tetraethyl-orthosilicate (TEOS). The monodisperse silica spheres in the size range of 100-500 nm were prepared by Stöber process (Stöber et al., 1968; Topuz, 2009) by changing the sol parameters including catalyst to alkoxide molar ratio as seen in Table 3.2. The specifications of chemicals utilized for preparation of silica particles are given in Table 3.1. Synthesis of monodisperse silica spheres was completed by stirring 4 hours at room temperature in a pyrex bottle. Then the particles were recovered by centrifuging and washed several times with deionized water and ethanol respectively. Finally the powder was dried in etuve at 313K. Before centrifuging, a sample was taken and diluted for size analysis (ZetaSizer 3000HS). The size and the shape of the spheres were examined by using SEM (Philips XL 30S, SFEG).

Table 3.1. Specifications of materials used in sol preparation.

Materials	Specifications
TEOS $\text{Si}(\text{OC}_2\text{H}_5)_4$	98%, M=208.3, d=0.934 $\text{g}/\text{cm}^3$ (Aldrich)
$\text{NH}_4\text{OH}$	26% $\text{NH}_3$ , M=35.05, d=0.9 $\text{g}/\text{cm}^3$ (Riedel)
Ethylalcohol $\text{C}_2\text{H}_5\text{OH}$	absolute, M=46.07, d=0.79 $\text{g}/\text{cm}^3$ (Merck)
$\text{H}_2\text{O}$	Ultrapure

Table 3.2. Synthesis Parameters employed for the preparation of monodisperse silica spheres.

Codes	Size (nm)	TEOS concentration	TEOS	NH <sub>3</sub>	H <sub>2</sub> O	EtOH	Total volume
SS1	483	0.28 M	1	4.39	16.89	51.52	500
SS2	201	0.28 M	1	2.189	14.24	55.83	500
SS3	297	0.28 M	1	4.38	14.27	54.82	500
SS4	140	0.28 M	1	1.11	14.18	57.11	100
SS5	120	0.28 M	1	1.12	15.96	50.89	100

SS (synthesized silica)

### 3.3. Specifications of Commercial TiO<sub>2</sub>, Al<sub>2</sub>O<sub>3</sub> and ZrO<sub>2</sub> Powders

The specifications of the commercial titania, alumina and zirconia powders used in rheology measurements are given in Table 3.3. The densities of titania powders of rutile and anatase phases, alumina and zirconia were taken as 4.2, 3.83 3.98 and 6.03 g/cm<sup>3</sup> respectively in the calculations.

Table 3.3. The specifications of the commercial powders.

Code	Trademark	Phase
Commercial TiO <sub>2</sub> 1 (CT1)	Tiona RCL-535	Rutile
Commercial TiO <sub>2</sub> 2 (CT2)	Tiona 595	Rutile
Commercial TiO <sub>2</sub> 3 (CT3)	Hombitan LW	Anatase
Commercial TiO <sub>2</sub> 4 (CT4)	Horasan	Rutile
Commercial Al <sub>2</sub> O <sub>3</sub> 1 (AL1)	Alcoa CT 3000 SG	alpha
Commercial Al <sub>2</sub> O <sub>3</sub> 2 (AL2)	Sumitomo AKP-50	alpha
Commercial ZrO <sub>2</sub>	Tosoh TZ-3Y	cubic

### **3.4. Characterization Methods**

The CaCO<sub>3</sub>, TiO<sub>2</sub> and SiO<sub>2</sub> powders were characterized by X-Ray diffraction Analyzer (XRD-Philips Expert Pro), Scanning Electron Microscope (SEM-Philips XL-30S FEG), ZetaSizer 3000 HSA (Malvern Instruments) Thermal Gravimetric Analyzer, (TGA- Shimadzu, TG-51) and FTIR spectroscopy (FTIR-8400S, Shimadzu Co.). The rheological behaviors of the dispersions were determined by using a rotational rheometer (Haake Mars II, Advanced rheometer System).

The XRD patterns of the materials were measured between 20-80° of 2θ. The samples for SEM micrographs were prepared by dispersing the material in ethanol by using sonification. The dispersed material was dropped onto stamp and led to dry at room temperature. The powders were diluted in ethanol for particle size distributions analysis in ZetaSizer. The dispersion was subjected to ultrasonic treatment for half of hour and ultrasonic treatment was repeated if necessary. All rheological measurements were performed by using parallel plate measurement apparatus with a diameter of 35 mm and 1 mL of the dispersion was used for each experiment.

### **3.5. Rheological Methods**

The rheological behaviour of the dispersions was determined by steady shear and dynamic shear rheology measurements. The measurements were done at 20°C and repeated for three times. The average values of these three measurements were reported. The suspensions of the powders were prepared by mixing with ethylene glycol and surfactant if it is necessary in an agate mortar. In this manuscript, static viscosity is described as the viscosity calculated by steady state measurement. The data points are an average of viscosity measurements once steady state has been reached or the maximum time has been exceeded which is determined by user. Dynamic viscosity measurement is described as the measured viscosity in which the data point is collected regardless if the equilibrium is reached or not.

## CHAPTER 4

### RESULTS AND DISCUSSION

#### 4.1. Synthesis, Characterization and Rheological Behaviour of $\text{CaCO}_3$

##### 4.1.1. Synthesis of $\text{CaCO}_3$ Particles

##### 4.1.1.1. $\text{CO}_2$ -bubbling

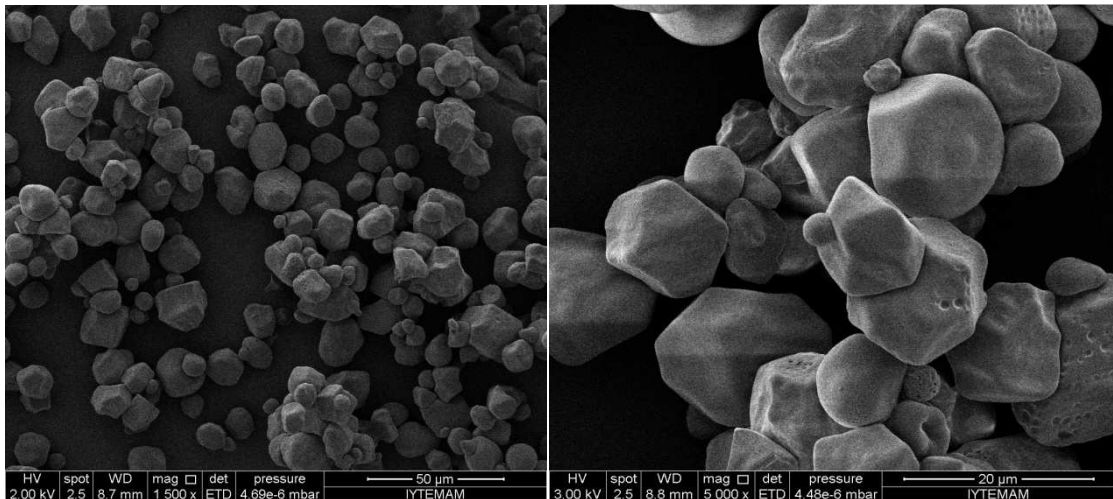


Figure 4.1. The SEM micrographs of corn starch.

The SEM micrographs of corn-starch which was used in the preparation of  $\text{CO}_2$  gas diffuser are given in Figure 4.1. The corn starch particles are seemed to be bimodal. The average size of the spherical granule of starch is approximately 10 µm.

The SEM micrographs show the starch-alumina diffuser after sintering process in Figure 4.2. It is evident that the pore size corresponds to approximately the size of the starch granules. There also seems to be alumina inside some pores as seen in Figure 4.2.

The XRD pattern of slaked lime which is the starting material of  $\text{CaCO}_3$  precipitation is given in Figure 4.3. It has the same diffraction pattern of standard  $\text{Ca(OH)}_2$  whose published diffraction pattern number is 76-0571. The main diffraction

peaks were located at 28.676, 34.101, 36.601, 47.144, 50.798, 54.356, 62.606, 64.3, and 71.808 of  $2\theta$ .

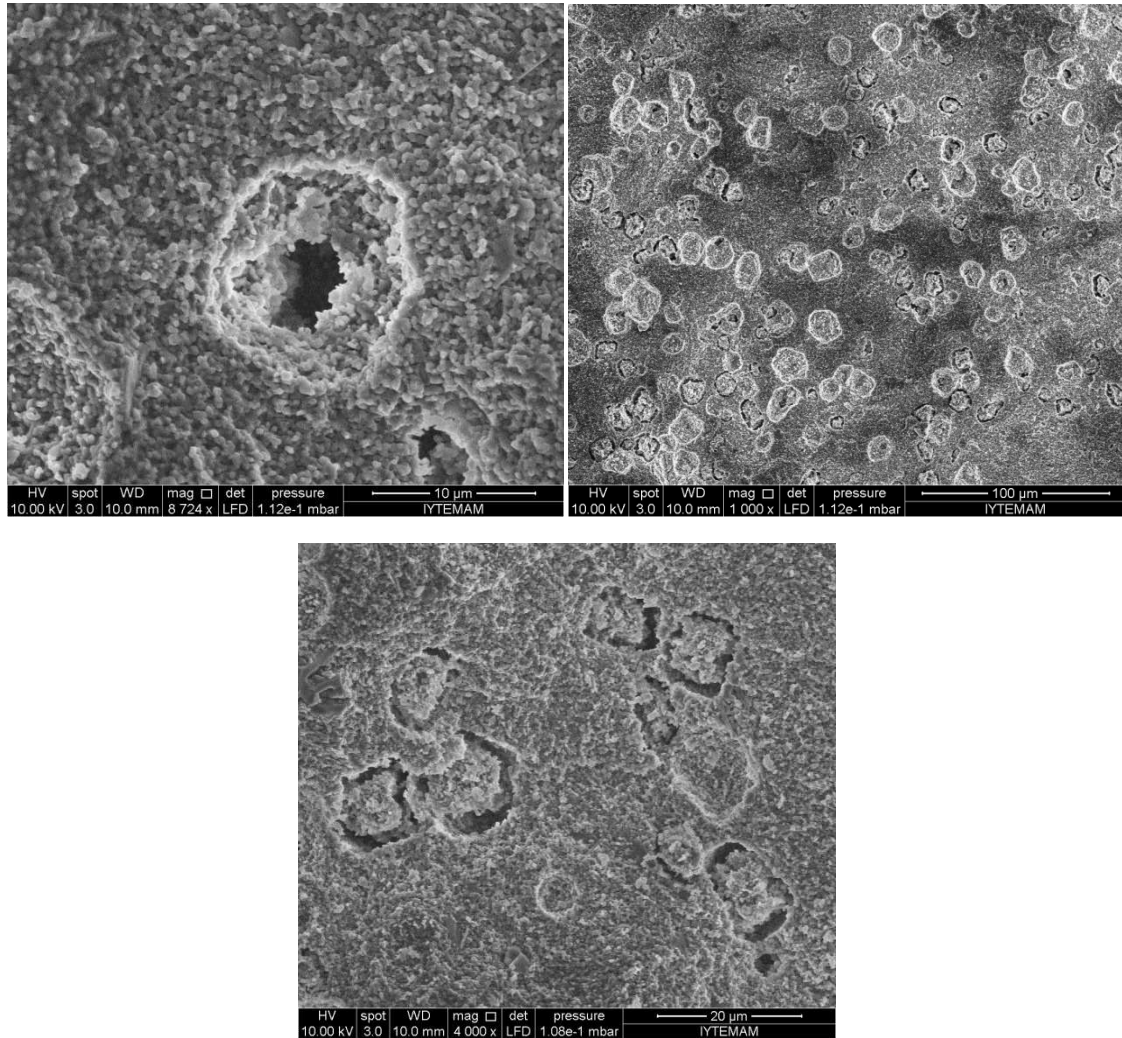


Figure 4.2. The SEM micrographs of ceramic gas-diffuser.

The FTIR bands of slaked lime are displayed in Figure 4.4. The strong band at  $3,643\text{ cm}^{-1}$  is related to the O–H bond. The intense and wide band at  $1,427\text{ cm}^{-1}$  corresponds to C–O bonds from carbonate. The band at  $875\text{ cm}^{-1}$  corresponds to Ca–O bonds. The wide and strong band at around  $500\text{ cm}^{-1}$  corresponds to the Ca–O bonds also (Galvan-Ruiz et al., 2009).

The TGA curve of slaked lime is given in Figure 4.5. Slaked lime lost 22.4 % of its weight when it is heated to  $1000^{\circ}\text{C}$ . The theoretical weight loss of  $\text{Ca}(\text{OH})_2$  to  $\text{CaO}$  is

calculated as 24.32%. The degradation after 500°C can be attributed to 11% CaCO<sub>3</sub>. There exists 2% moisture.

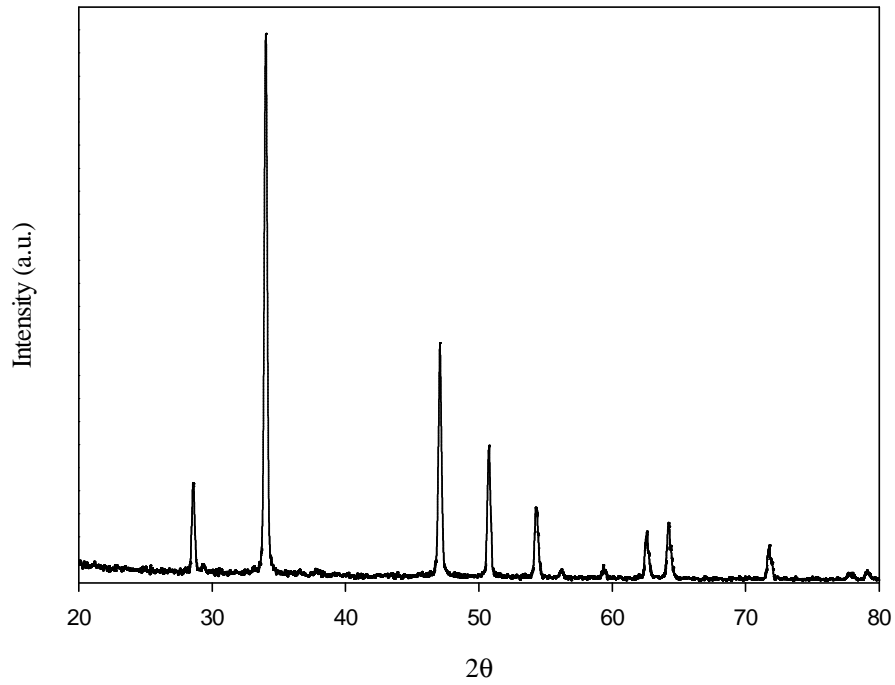


Figure 4.3. The XRD pattern of slaked lime.

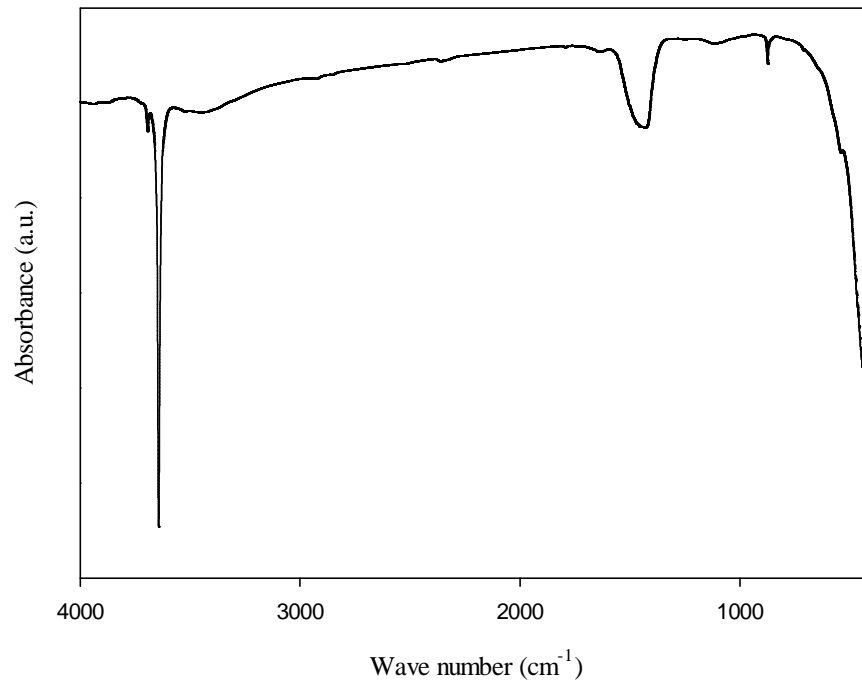


Figure 4.4. The FTIR spectra of slaked lime.

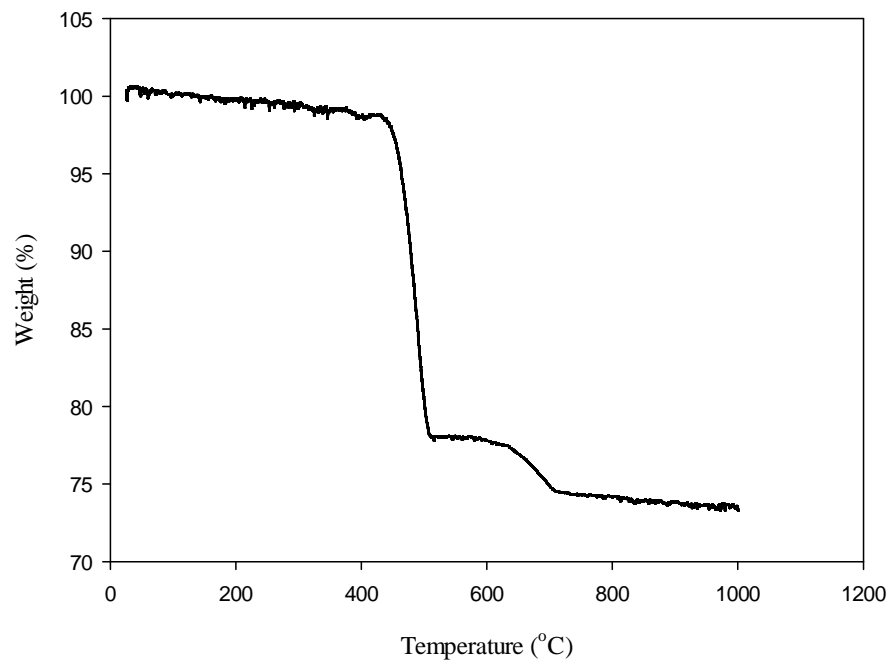


Figure 4.5. The TGA curve of slaked lime.

The SEM micrographs of slaked lime display that the shape of  $\text{Ca}(\text{OH})_2$  particles is hexagonal as in Figure 4.6.

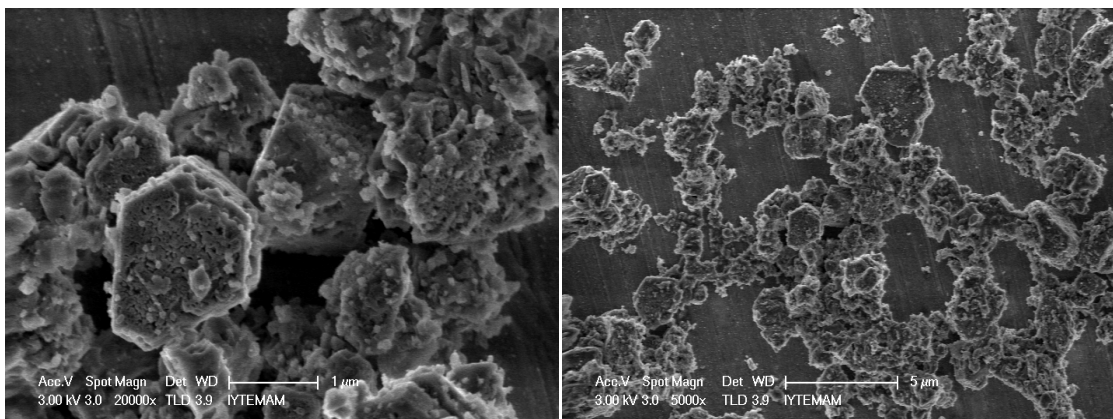
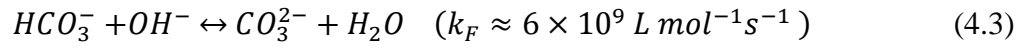
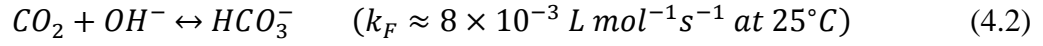
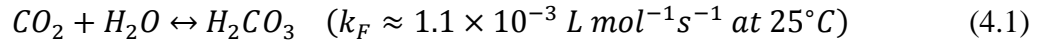


Figure 4.6. The SEM micrographs of slaked lime.

One common method of generating calcium carbonate is through the absorption and reaction of carbon dioxide with dissolved calcium hydroxide in an aqueous system. This reaction produces calcium carbonate, which has a much lower solubility than that

of either of the precursor components and thus precipitates out, usually in the form of small particles. The following equations summarize the processes involved (31).



The hydration of dissolved  $CO_2$  to form weak carbonic acid is described in Equation 4.1. The forward reaction rate for this reaction at  $25^\circ\text{C}$  is reported as  $8 \times 10^{-3} \text{ L mol}^{-1} \text{ s}^{-1}$ . This is described as a slow reaction in pure water, giving an equivalent first-order rate of  $0.06 \text{ sec}^{-1}$  for  $CO_2$  conversion, yielding low concentrations of  $H_2CO_3^*$  0.1% of dissolved  $CO_2$  at equilibrium. The bicarbonate ion  $HCO_3^-$  can be formed rapidly by the direct reaction of  $CO_2$  and  $OH^-$  at higher pH values, where there are significantly more hydroxyl ions as shown by Equation 4.2. The forward reaction rate for the formation of the carbonate ion, shown by Equation 4.3, is in the order of  $6 \times 10^9 \text{ L mol}^{-1} \text{ sec}^{-1}$ , leading to rapid equilibrium times between the ions. The dissociation of calcium hydroxide  $Ca(OH)_2$  into  $Ca^{2+}$  ions and  $OH^-$  ions is shown in Equation 4.4. In general this system is strongly dissociating and the majority of the calcium can be assumed to be in the form of  $Ca^{2+}$ . This results in liquid that is a strong base and will readily convert dissolved  $CO_2$  into bicarbonate and carbonate ions that can rapidly react with the calcium ions, to form calcium carbonate  $CaCO_3$ , as illustrated in Equation 4.5. The solubility of  $CaCO_3$  in water at room temperature is very low at between  $1.2 \times 10^{-5}$  and  $1.4 \times 10^{-5} \text{ kg/kg}$  and readily precipitates out of the liquid as fine particles. This removes ions from the system and lowers both the pH and conductivity of the solution. The slow production of carbonic acid through the route shown by Equation 4.1, after the complete conversion of the  $Ca(OH)_2$ , will continue to reduce the pH of the liquid and redissolve some of the  $CaCO_3$ , although this mechanism typically takes minutes and for short residence time processes it can be ignored.

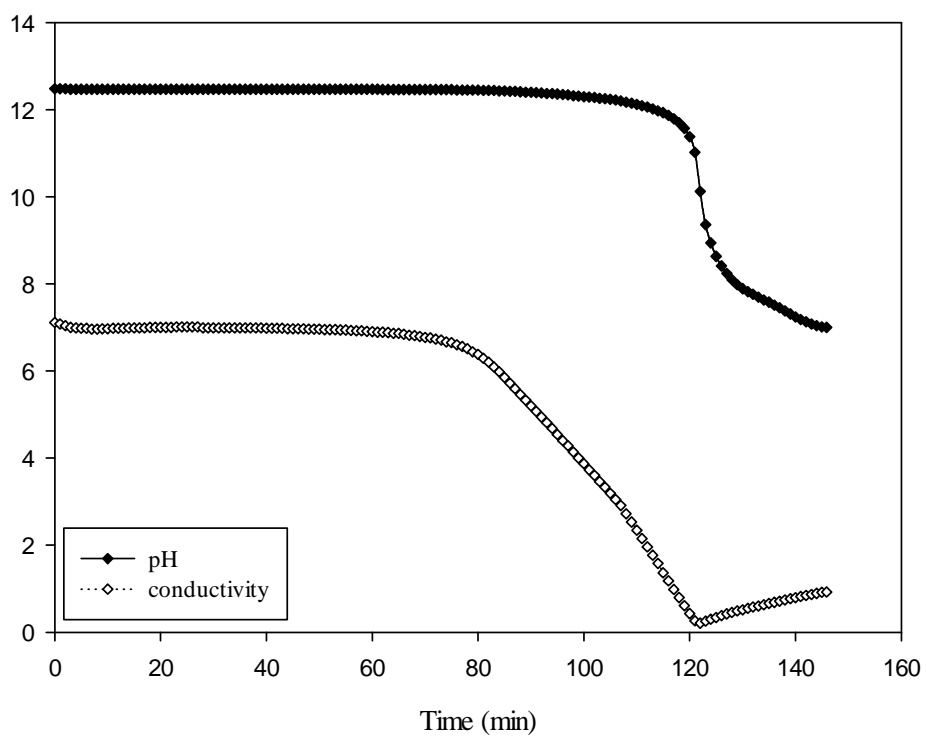


Figure 4.7. The pH and conductivity change during CaCO<sub>3</sub> synthesis reaction.

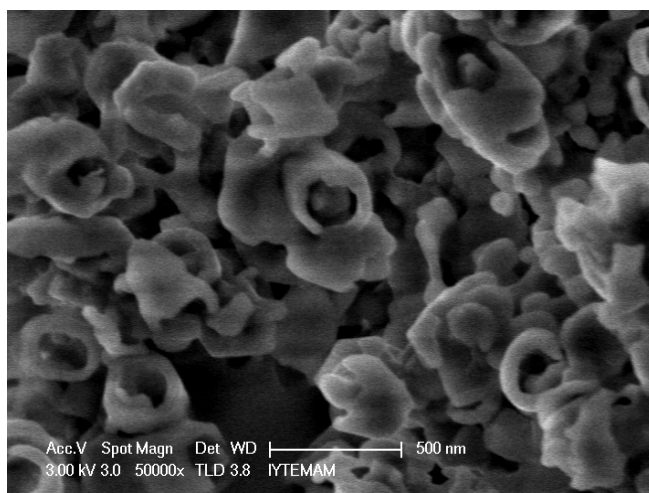


Figure 4.8. The SEM micrograph of sample taken at pH=12.45 from the reaction slurry

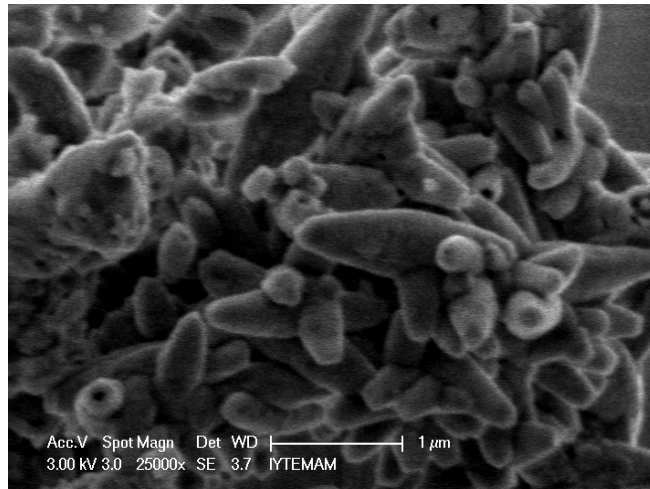


Figure 4.9. The SEM micrograph of sample taken at pH=12 from the reaction slurry

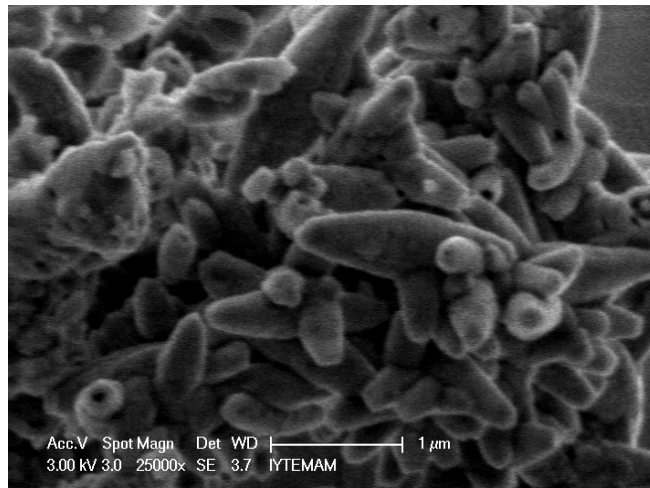


Figure 4.10. The SEM micrograph of sample taken at pH=11.52 from the reaction slurry

The pH and conductivity change during  $\text{CaCO}_3$  synthesis is displayed in Figure 4.7. The process led to the accumulation of an excess dissolved  $\text{Ca}(\text{OH})_2$  in the growth medium by maintaining constant  $\text{CO}_2$  flow rate when the pH and conductivity curves remained constant. The drop of conductivity curve indicates the consumption of calcium species. The reaction was stopped when the pH reached 7.

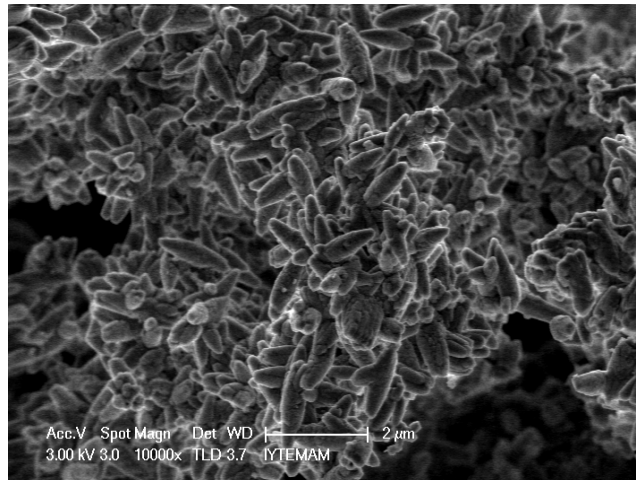


Figure 4.11. The SEM micrograph of sample taken at pH=9.67 from the reaction slurry

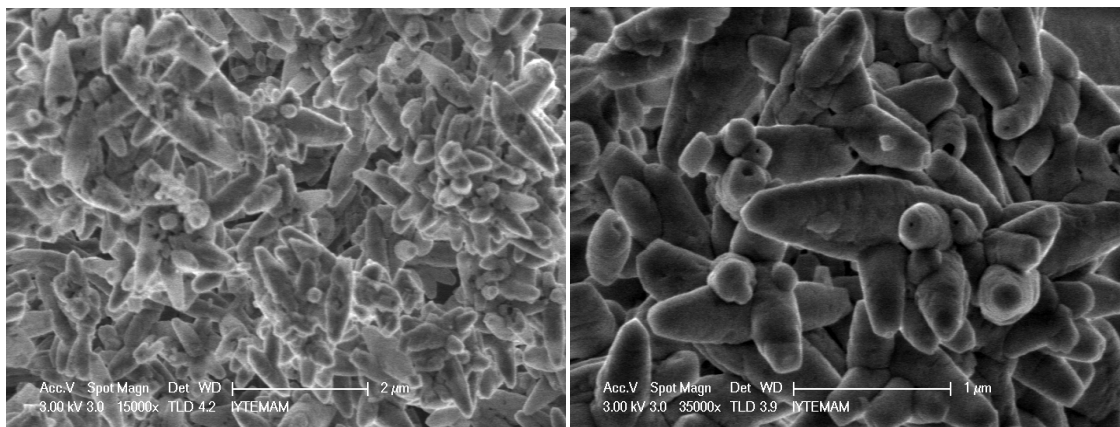


Figure 4.12. The SEM micrograph of sample taken at pH=7 from the reaction slurry

The SEM micrographs display the morphology of the powders prepared at different pH values during the reaction in Figures 4.8 through 4.12. The formation period of needle-like particles can be seen in the figures.

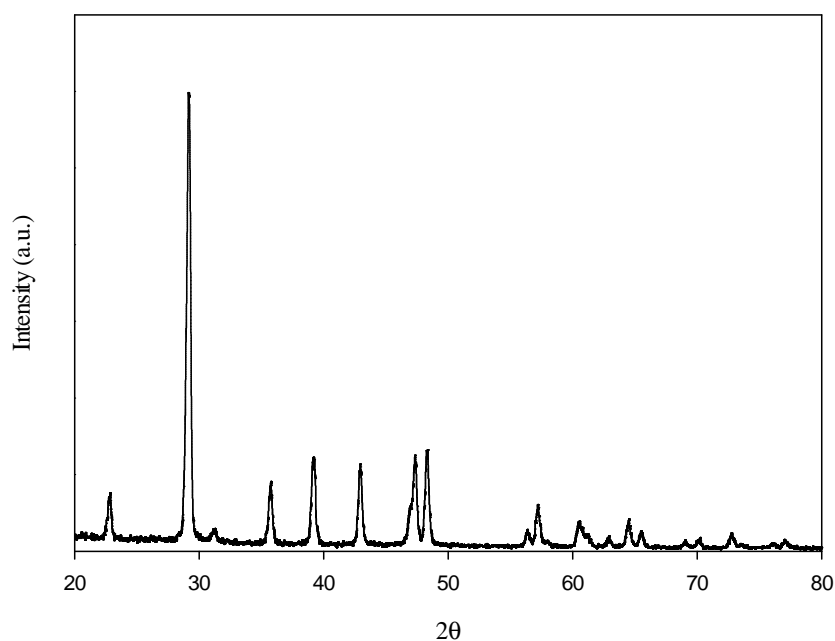


Figure 4.13. The XRD pattern of synthesized  $\text{CaCO}_3$  particles.

The XRD pattern of precipitated  $\text{CaCO}_3$  is given in Figure 4.13. The XRD pattern shows that its typical peaks relate with the calcite polymorph of  $\text{CaCO}_3$ . The pattern is similar to standard XRD diffraction pattern of calcite whose diffraction pattern number is 86-0174. The main peaks were located at 23.058, 29.399, 31.422, 35.981, 39.417, 43.171, 47.492, 48.505 and 56.582 of  $2\theta$ .

The Figure 4.14 shows the FTIR bands of precipitated  $\text{CaCO}_3$  particles. The absorption peaks at  $717\text{ cm}^{-1}$  and  $876\text{ cm}^{-1}$  can be attributed to calcite. The thin and intense band at  $1795\text{ cm}^{-1}$  is also associated to the carbonate  $\text{C=O}$  bonds. The very strong band at  $1,444\text{ cm}^{-1}$  is related to the carbonate  $\text{C-O}$  bonds (30).

The TGA curve of precipitated  $\text{CaCO}_3$  is given in Figure 4.15. Synthesized  $\text{CaCO}_3$  particles lost 45.914 % of its weight when it is heated to  $1000^\circ\text{C}$ . The theoretical weight loss of  $\text{CaCO}_3$  to  $\text{CaO}$  is 44%. The 1.91% difference can be due to the freely absorbed water onto the surface.

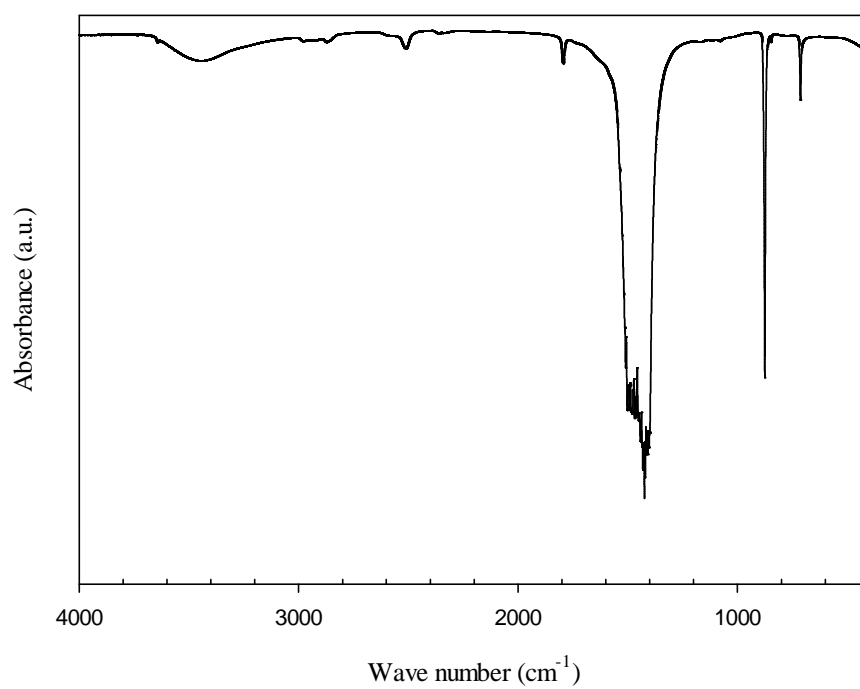


Figure 4.14. The FT-IR spectra of synthesized CaCO<sub>3</sub> particles.

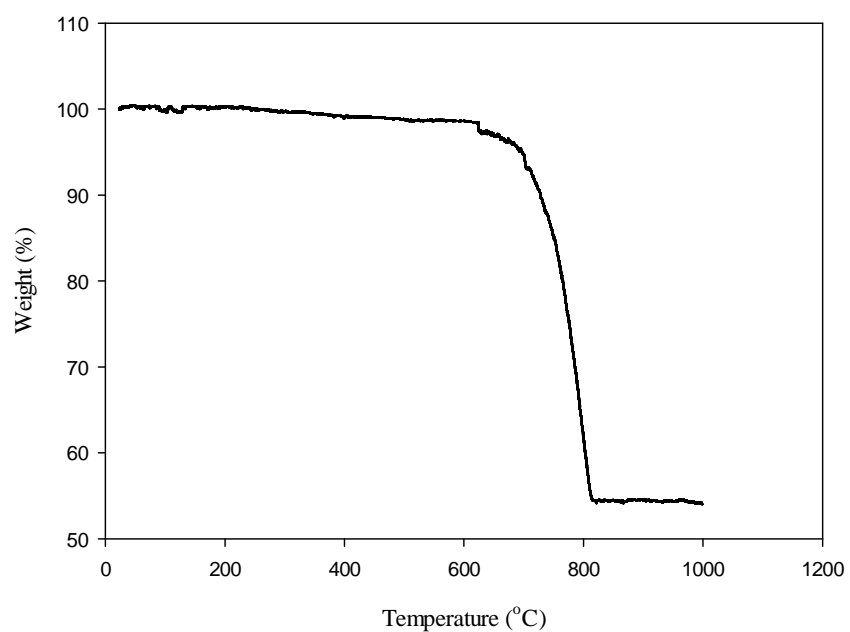


Figure 4.15. The TGA curve of synthesized CaCO<sub>3</sub> particles.

#### 4.1.1.2. Ballmilling Process

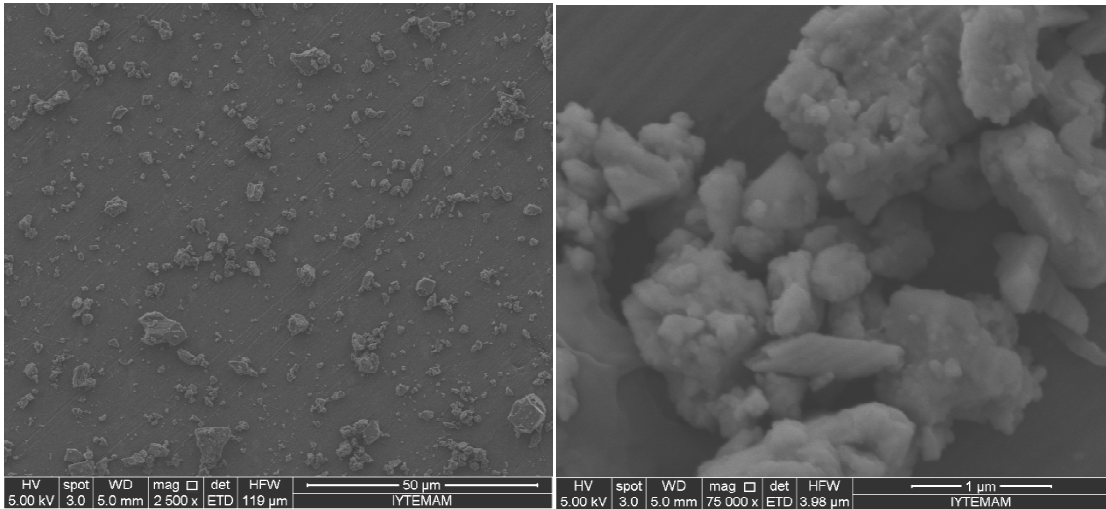


Figure 4.16. The SEM micrographs of natural CaCO<sub>3</sub> particles.

The natural CaCO<sub>3</sub> particles were used in grinding processes and the SEM micrographs are seen in Figure 4.16. The particles are not so uniform. The average particles size can be assumed as 1-2 µm.

The SEM micrographs of ballmilled natural CaCO<sub>3</sub> particles without surfactant after 5 hours are displayed in Figure 4.17 where the shape of the particles is seen as cubic. The slurry concentration was 30 wt% during the grinding process. There is a size reduction after grinding process with zirconia beads in the size of 2 mm and 10 mm. The particle size distributions of Ball1 at different time intervals during grinding process are shown in Figure 4.18. The particle size reduces to 640, 418, 443 and 320 nm by volume after 50, 100, 150, and 200 minutes of grinding process. The particle size distribution is given in Figure 4.19 at the end of the grinding process at the end of 250 minutes. There is a bimodal size distribution according to the graph. The average particle size by volume is 50.5 nm (23%) and 249 nm (76.9%). The average particle size by number is 48.8 nm (97.1%) and 232.4 nm (2.9%). The number of the particles below 100 nm is high; however, by volume they show up a little and the 249 nm particles dominate the volume of the suspension.

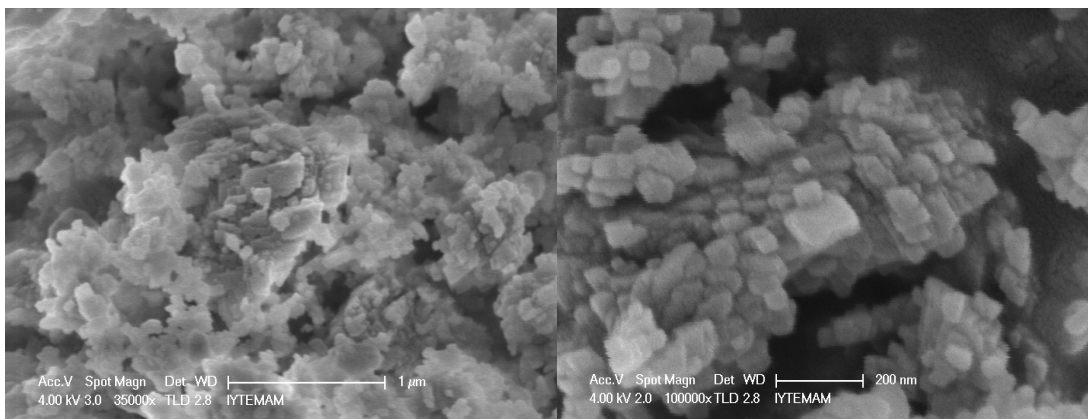


Figure 4.17. The SEM micrograph of Ball1.

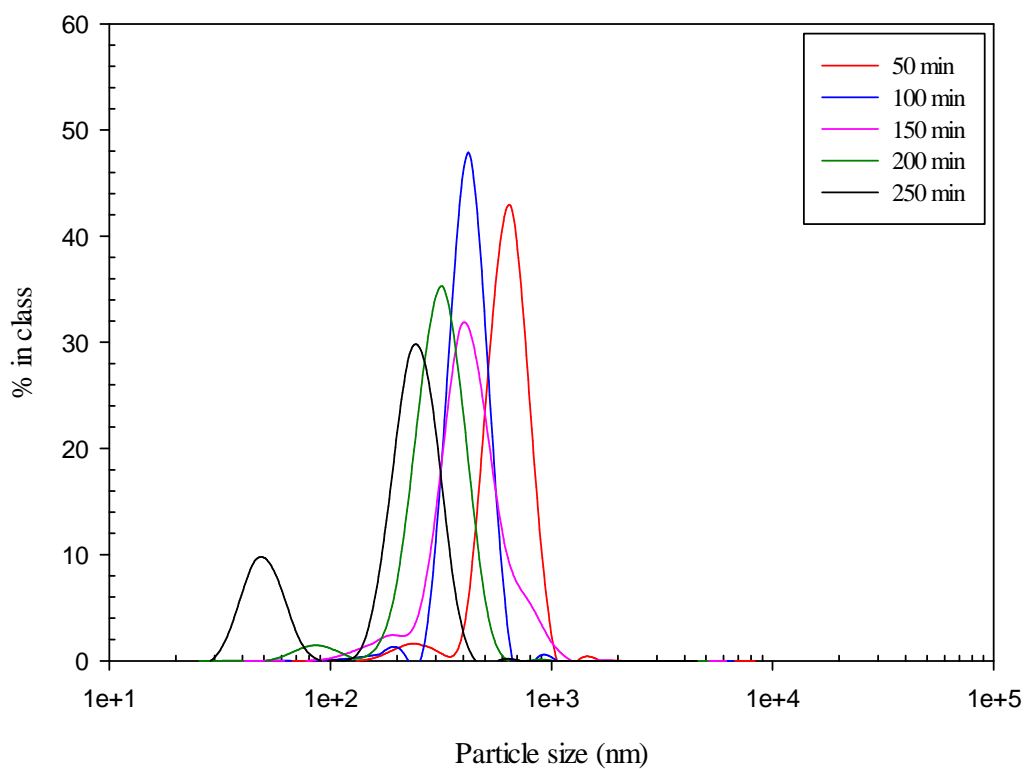


Figure 4.18. Particle size distribution of Ball1 at different time intervals.

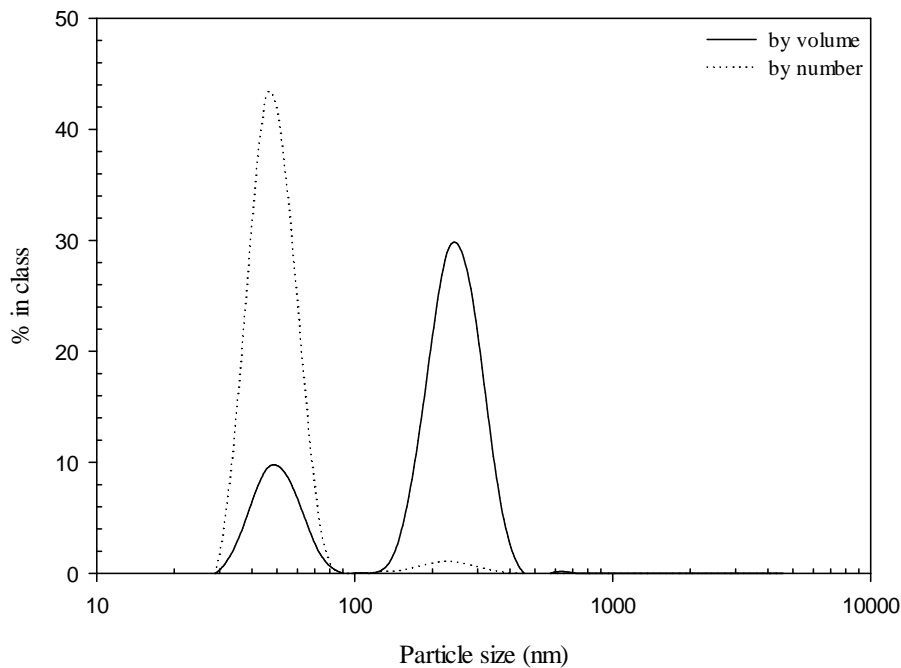


Figure 4.19. Particle size distribution of Ball1 at the end of 250 min.

Small zirconia beads were used in addition to the beads of 2 and 10 mm in Ball2 grinding process in order to reduce the size more as Jang et al. used the zirconia beads in the size of 30, 100 and 300  $\mu\text{m}$  (Jang et al., 2009). The slurry concentration was reduced to 15% (wt) and sodium polyacrylate was added as a surfactant in contrast to Ball1. The SEM micrographs of Ball2 are shown in Figure 4.21. The particle size distribution is given in Figure 4.22. The average particle size by volume is 40.6 nm (69%) and 195.2 nm (32%). The average particle size by number is 39.7 nm (99.6%). The 195.2 nm particles that show up in volume could be due to the attraction of nanoparticles which causes agglomeration. There is a significant size-reduction in  $\text{CaCO}_3$  particles with the help of small zirconia beads and surfactant when it is compared to Ball1. The size of most particles was reduced to 40 nm and the 40 nm particles obviously occupy in volume of Ball2.

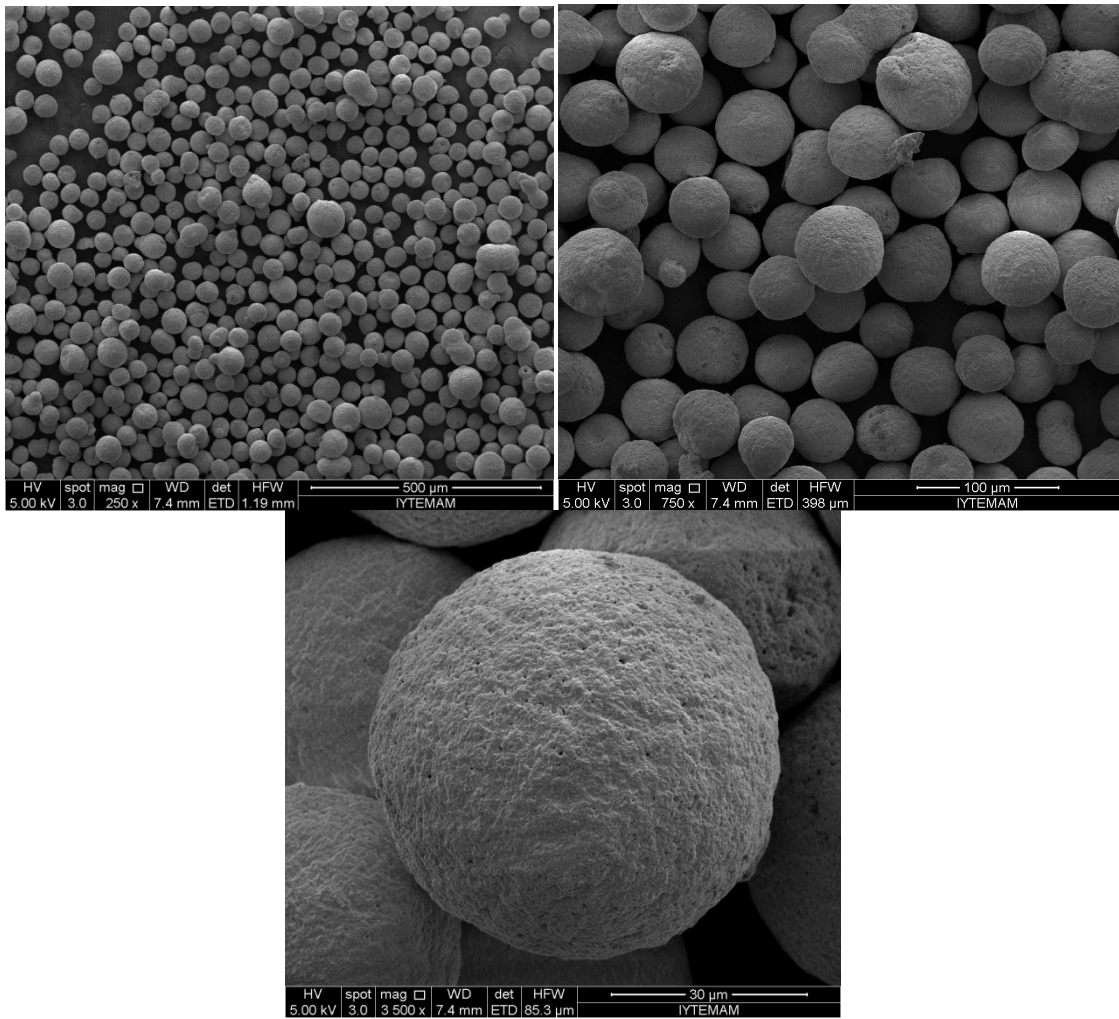


Figure 4.20. The SEM micrographs of small zirconia beads used in grinding.

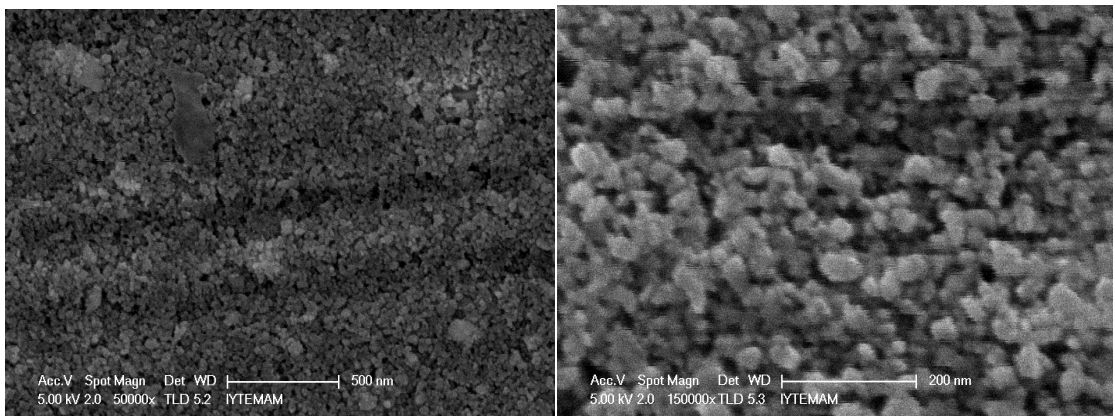


Figure 4.21. The SEM micrographs of Ball2.

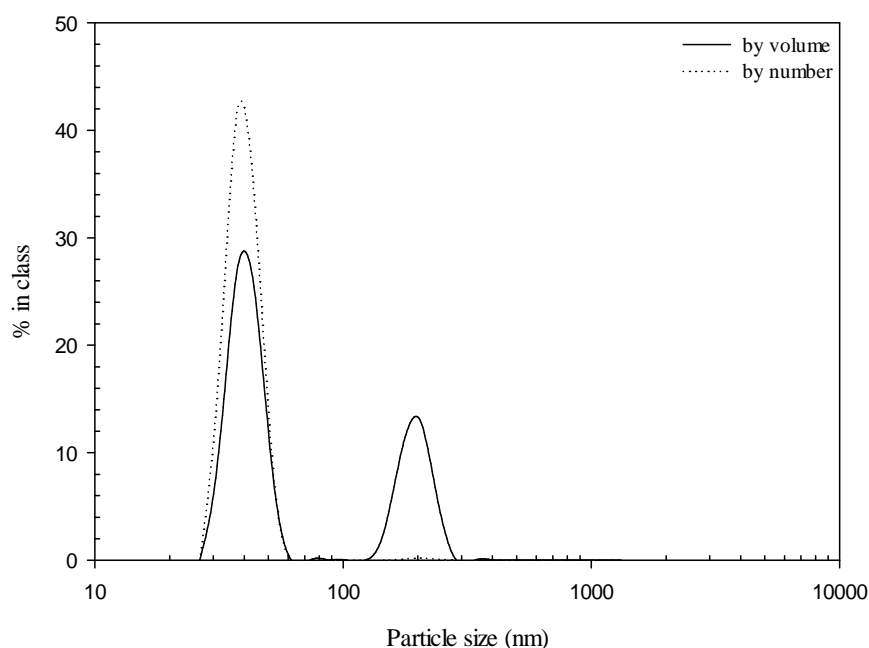


Figure 4.22. Particle size distribution of Ball2 at the end of grinding process.

#### 4.1.2. Rheological Behaviour of CaCO<sub>3</sub> Suspensions

The dynamic viscosity curve of 45 vol% suspension of precipitated CaCO<sub>3</sub> particles in ethylene glycol is given in Figure 4.23. An increase in viscosity was observed from 0.7113 to 15.16 Pa.s at shear rates between 0.4873 and 398.36 sec<sup>-1</sup>. The viscosity of the suspension starts to decrease slightly after that shear rate. The viscosity and flow curves look quite similar in the Figures 4.23 and 4.24. The fit of the data to Power was displayed in Figure 4.25. The  $n$  and  $K$  values were calculated as 2.62 and 1.27 with  $R^2$  value of 0.9786. The  $n$  value is greater than 1, so the 45 vol% suspension of precipitated CaCO<sub>3</sub> in ethylene glycol is shear-thickening according to the power law. The maximum volume fraction that we could reach was  $\Phi=0.45$  for the precipitated CaCO<sub>3</sub> particles without any surfactant in ethylene glycol.

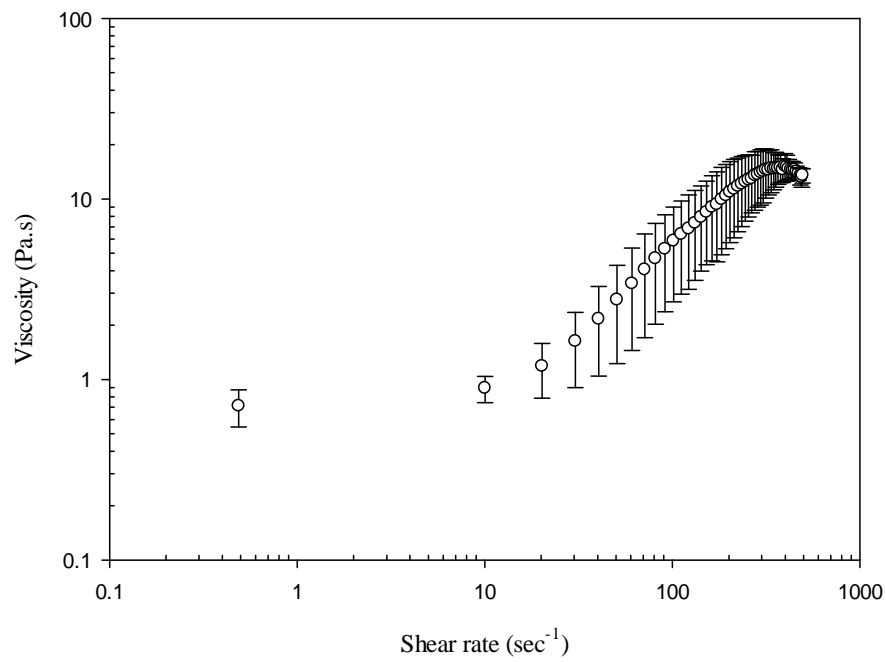


Figure 4.23. Dynamic viscosity curve of 45 vol% suspension of synthesized  $\text{CaCO}_3$  particles in ethylene glycol.

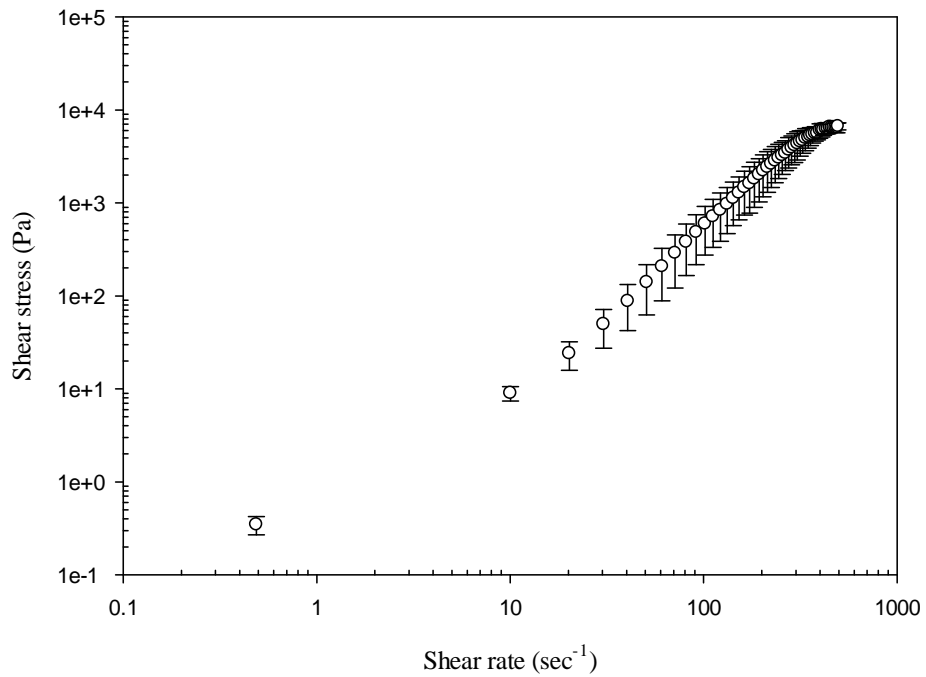


Figure 4.24. Flow curve of 45 vol% suspension of synthesized  $\text{CaCO}_3$  particles in ethylene glycol.

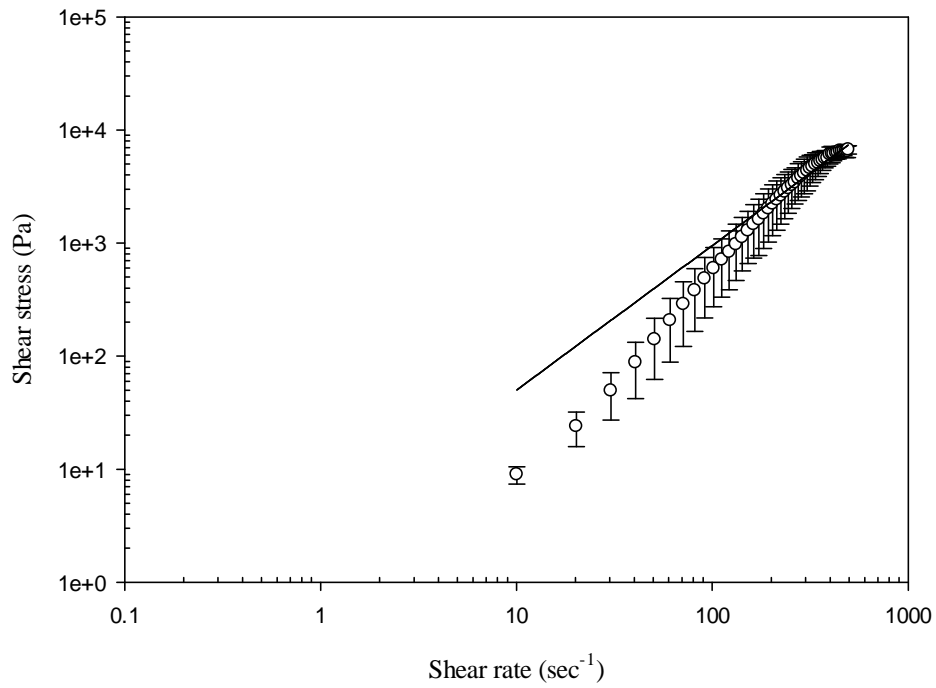


Figure 4.25. Flow curve of 45 vol% suspension of synthesized CaCO<sub>3</sub> particles in ethylene glycol (the solid line represents the power law model).

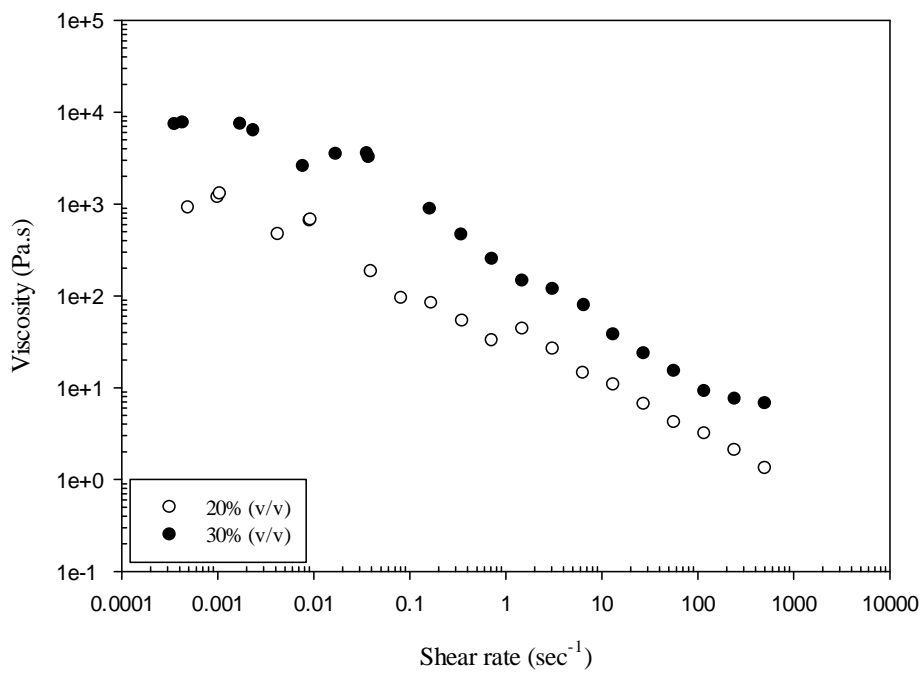


Figure 4.26. Static viscosity curves of the suspensions of Ball1 in ethylene glycol.

The static viscosity curves of Ball1 in ethylene glycol at volume fractions of  $\Phi=0.2$  and 0.3 are shown in Figure 4.26, where there is a linear decrease in the viscosity versus shear rate data.

The dynamic viscosity of Ball1 in ethylene glycol without any surfactant is displayed in Figure 4.27. The 20 vol% suspension shows a linear decrease in viscosity whereas the viscosity of 30 vol% suspension initially remains constant, slightly increases and then decreases sharply.

The flow curves of Ball1 in ethylene glycol are given in Figure 4.28 and the fit of data to power law on the flow curves is displayed in Figure 4.29. The  $n$  values are both smaller than 1, which indicate that the 20 vol% and 30 vol% suspensions of Ball1 in ethylene glycol are shear-thinning as seen in Table 4.1. The  $K$  value decreased from 51.75 to 28.19 when the suspension volume fraction is increased from 0.20 to 0.30.

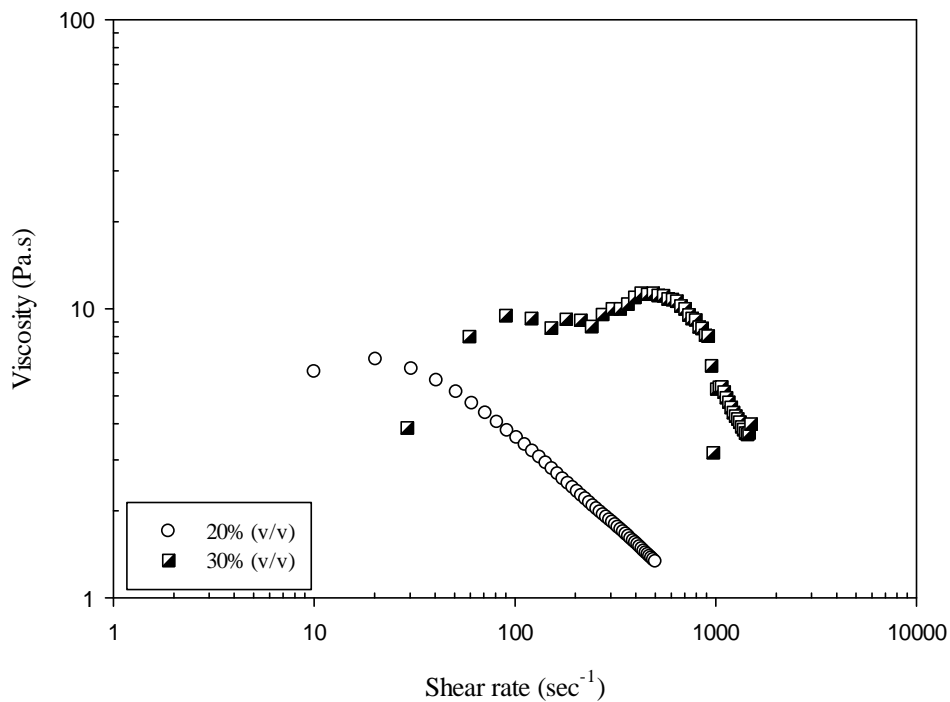


Figure 4.27. Dynamic viscosity curves of the suspensions of Ball1 in ethylene glycol.

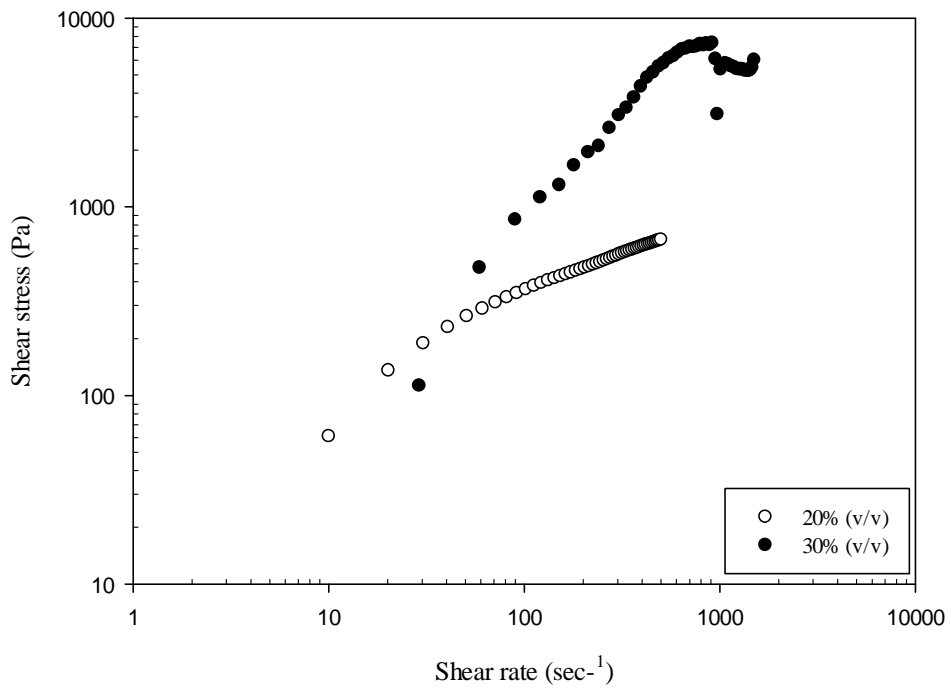


Figure 4.28. Flow curves of the suspensions of Ball1 in ethylene glycol.

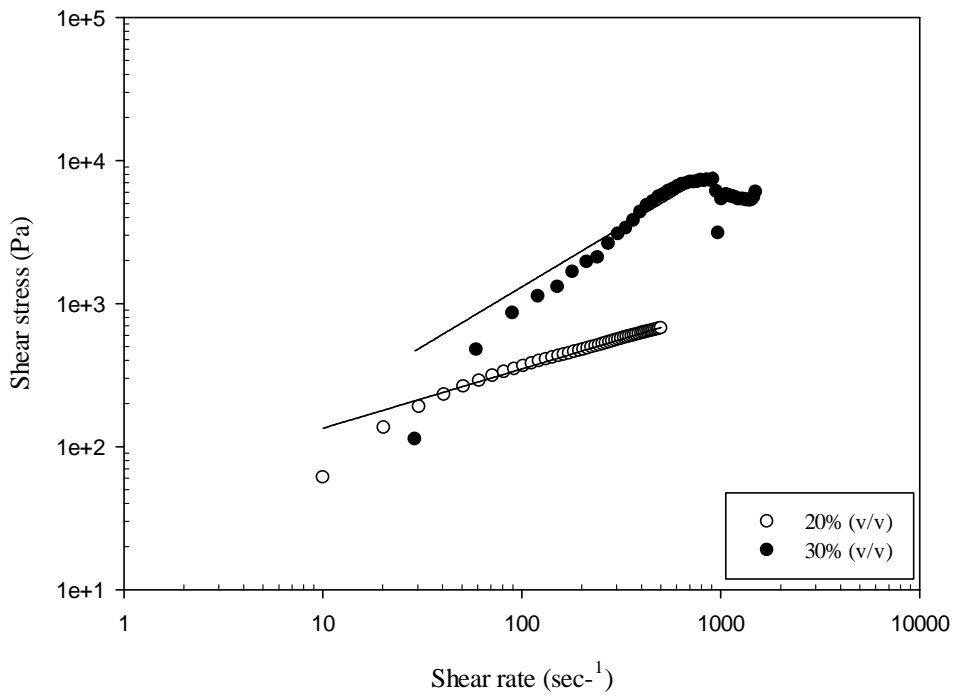


Figure 4.29. Flow curves of the suspensions of Ball1 in ethylene glycol (the solid lines represent the power law model).

Table 4.1. The model parameters of Power Law calculated for the suspensions of Ball1 in ethylene glycol.

$\Phi$	n value	K value	$R^2$
0.2	0.4	51.75	0.9898
0.3	0.8333	28.19	0.8333

The suspensions of Ball1 were prepared in ethylene glycol by ballmilling so that a well-dispersed suspension could be obtained. The static viscosity curves are given in Figure 4.30. The difference in the suspension preparation can be seen in the viscosity curves in Figure 4.32.

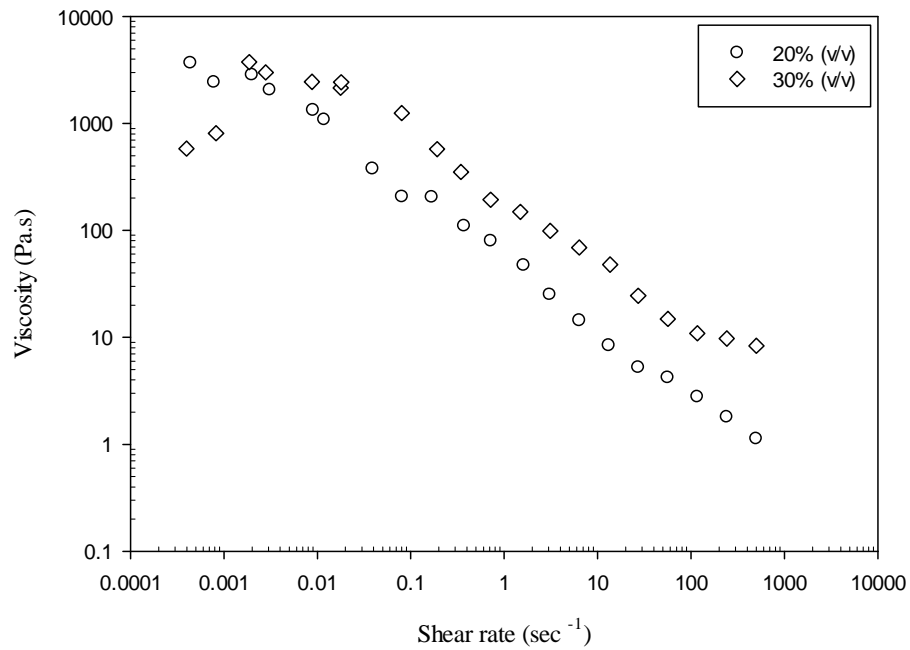


Figure 4.30. Static viscosity curves of the suspensions of Ball1 in ethylene glycol prepared by ballmilling.

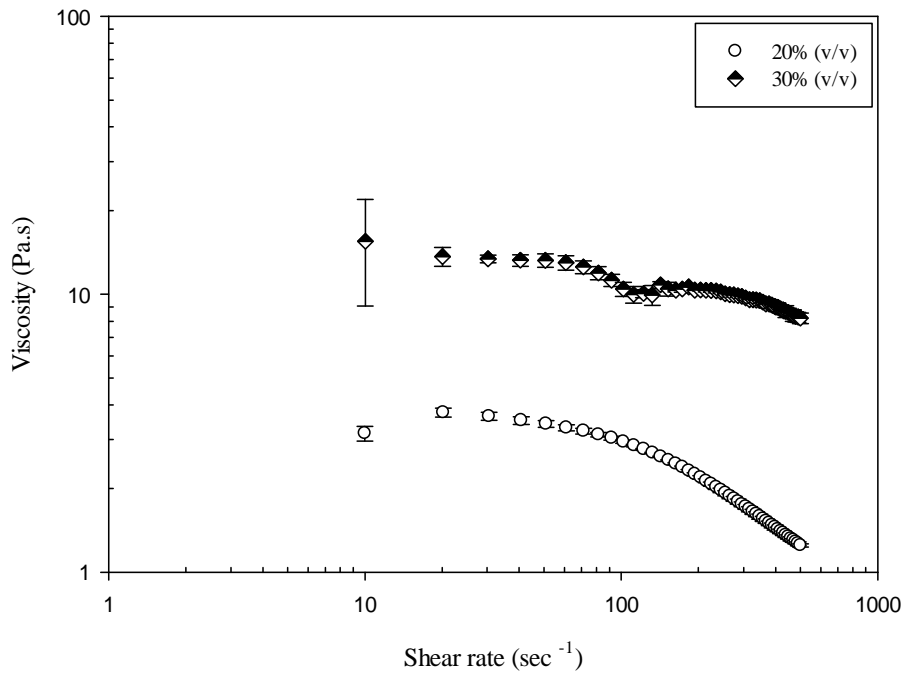


Figure 4.31. Dynamic viscosity curves of the suspensions of Ball1 in ethylene glycol prepared by ballmilling.

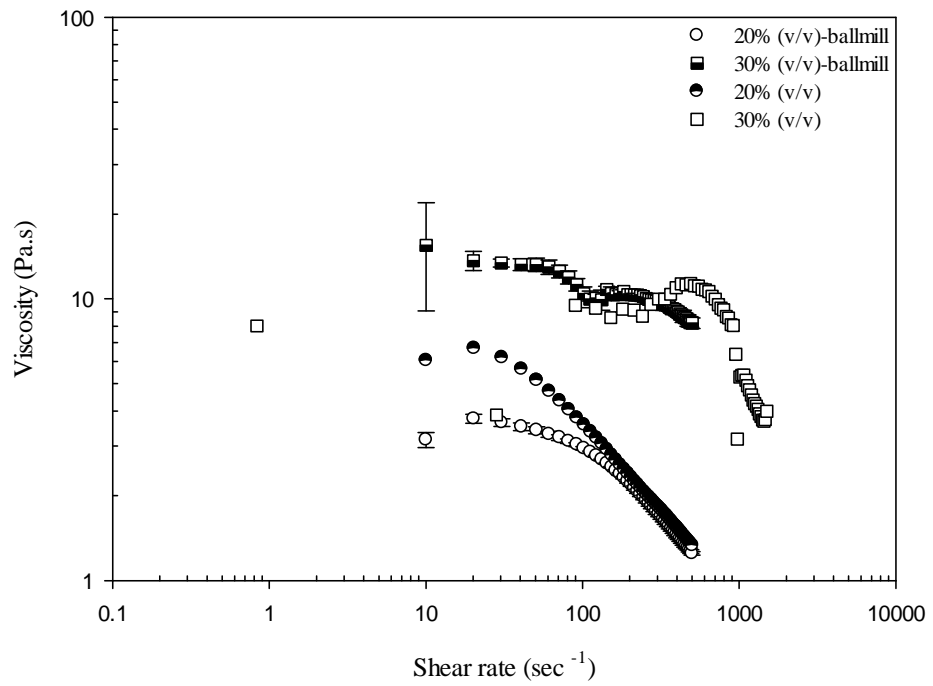


Figure 4.32. The comparison of dynamic viscosity curves of the suspensions of Ball1 in ethylene glycol.

The flow curves of Ball1 in ethylene glycol prepared by ballmilling are given in Figure 4.33 and the fit of data to power law is displayed in Figure 4.34. The  $n$  values are both found to be smaller than 1, which indicate that the 20 and 30 vol% suspensions of Ball1 in ethylene glycol prepared by ballmilling are also shear-thinning as seen in Table 4.2. The  $K$  value decreased from 30.43 to 29.99 when the suspension volume fraction is increased from 0.20 to 0.30. The  $K$  values are quite similar. There is a small variation in the  $K$  values given in Tables 4.1 and 4.2 although the parameter  $n$  stays almost constant.

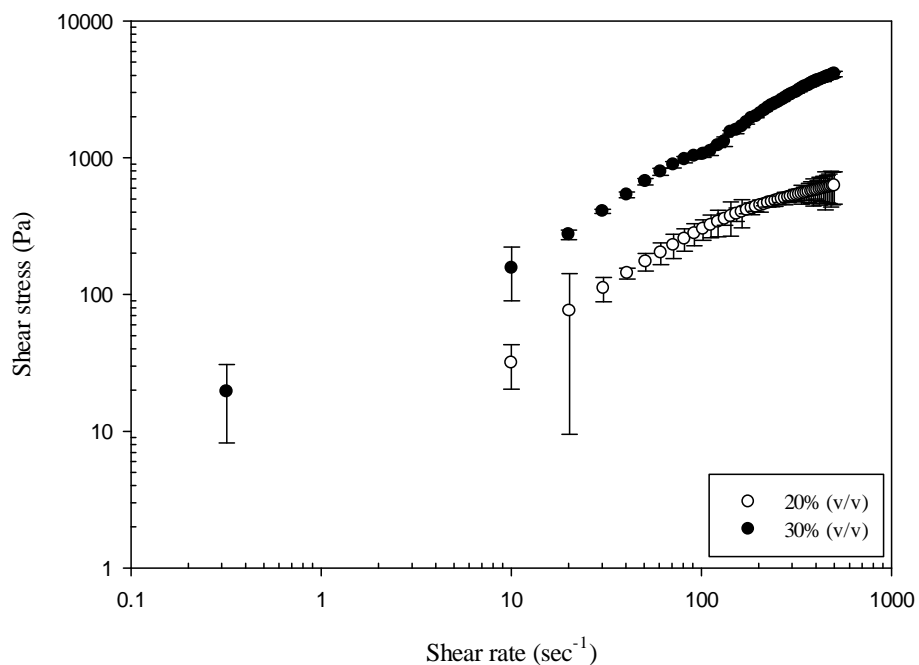


Figure 4.33. Flow curves of the suspensions of Ball1 in ethylene glycol prepared by ballmilling.

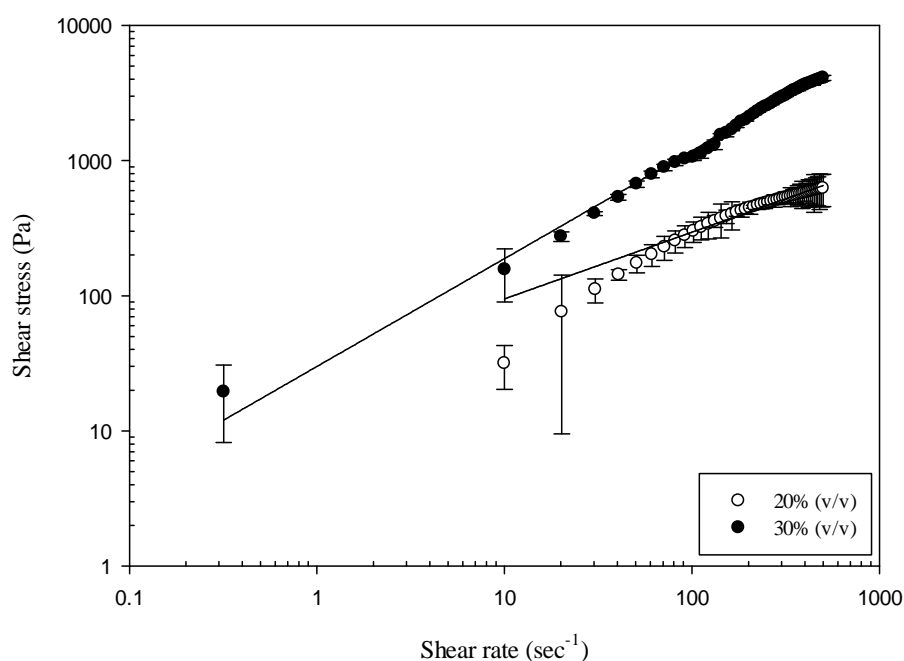


Figure 4.34. Flow curves of the suspensions of Ball1 in ethylene glycol prepared by ballmilling (the solid lines represent the power law model).

Table 4.2. The model parameters of Power Law of different calculated for the suspensions Ball1 in ethylene glycol prepared by ballmilling.

$\Phi$	n value	K value	$R^2$
0.2	0.4936	30.4344	0.9761
0.3	0.7976	29.9948	0.9955

## 4.2. Characterization and Rheological Behaviour of $TiO_2$

### 4.2.1. Characterization of Commercial $TiO_2$ Powders

The FT-IR spectra of the  $TiO_2$  powders are given in Figure 4.35. The bands at 800–400 and the region  $3400\text{ cm}^{-1}$  correspond to the O-H mode. The band in the region  $2500\text{ cm}^{-1}$  represent the  $CO_2$ . The presence of  $CO_2$  is due to the absorption of atmospheric  $CO_2$  (Sajan et al., 2011). The XRD patterns of the  $TiO_2$  powders are given in Figure 4.36. The diffraction pattern numbers for anatase and rutile phases of  $TiO_2$

that were matched to the samples are 71-1166 and 72-1148, respectively. The CT1, CT2 and CT4 powders

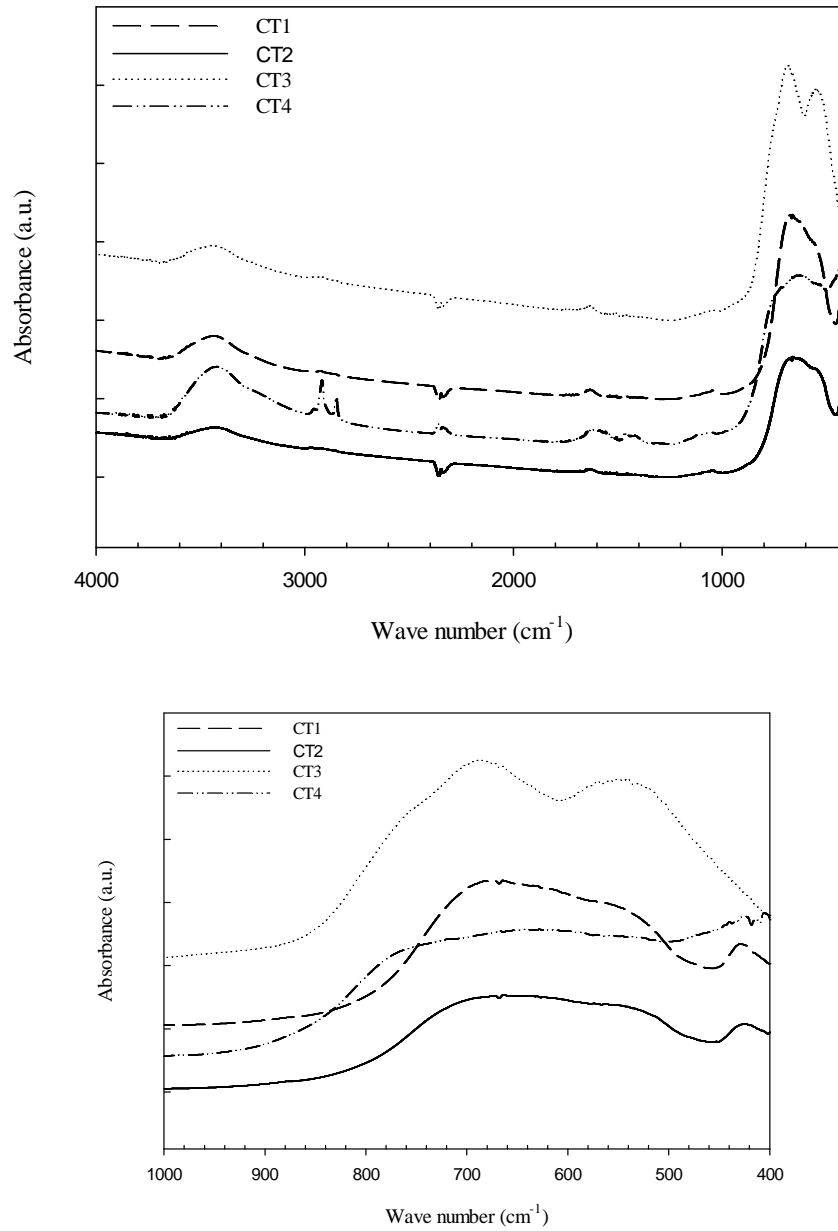


Figure 4.35. The FT-IR spectra of commercial  $\text{TiO}_2$  powders.

are in rutile phase, whereas CT3 powder is in anatase phase. There is also a small peak of rutile phase in the X-ray spectra of the sample CT3. The percentage of rutile phase is calculated as 4.2 % with Equation 4.6 (Sajan et al., 2011; Wu et al., 2008).

$$W_R(\%) = \frac{1}{1+0.8\left(\frac{I_A}{I_R}\right)} \times 100 \quad (4.6)$$

where  $W_R$  is the weight percentage of rutile in the  $\text{TiO}_2$  sample and  $I_A$  and  $I_R$  are the intensities of the anatase {101} and rutile {110} peaks, respectively.

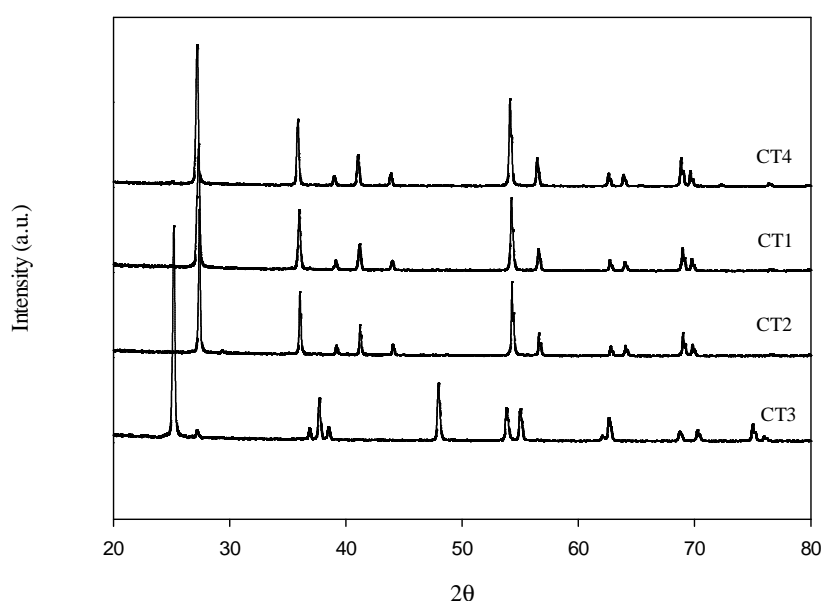


Figure 4.36. The XRD patterns of titania powders.

The TGA curves of  $\text{TiO}_2$  powders are given in Figure 4.37. The weight losses of the powders CT1, CT2, CT3 and CT4 during heating up to  $1000^\circ\text{C}$  are calculated as 2.009%, 2.251%, 2.582% and 3.774% respectively. There are no significant weight losses. These losses could be due to the adsorbed water onto the surface of  $\text{TiO}_2$  from atmosphere.

The particle size distribution of the powder CT1 is given in Figure 4.38 where it can be concluded that CT1 powder is polydisperse. 305 nm particles mostly occupy by volume, nevertheless there are particles at 145 nm but they do not occupy so much volume.

The particle size distribution of the powder CT1 is displayed in Figure 4.39. The average particle size is found as 335 nm. There are also 160 nm particles. The particle size distributions of CT1 and CT2 powders seem to be quite similar according to the Figure 4.2.1.8.

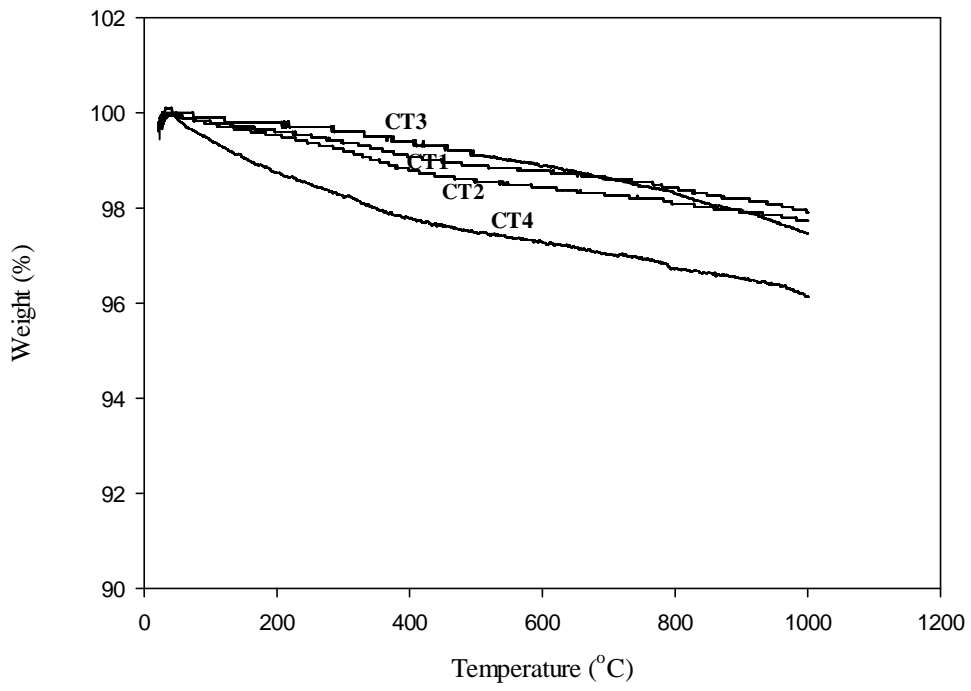


Figure 4.37. The TGA curves of TiO<sub>2</sub> powders.

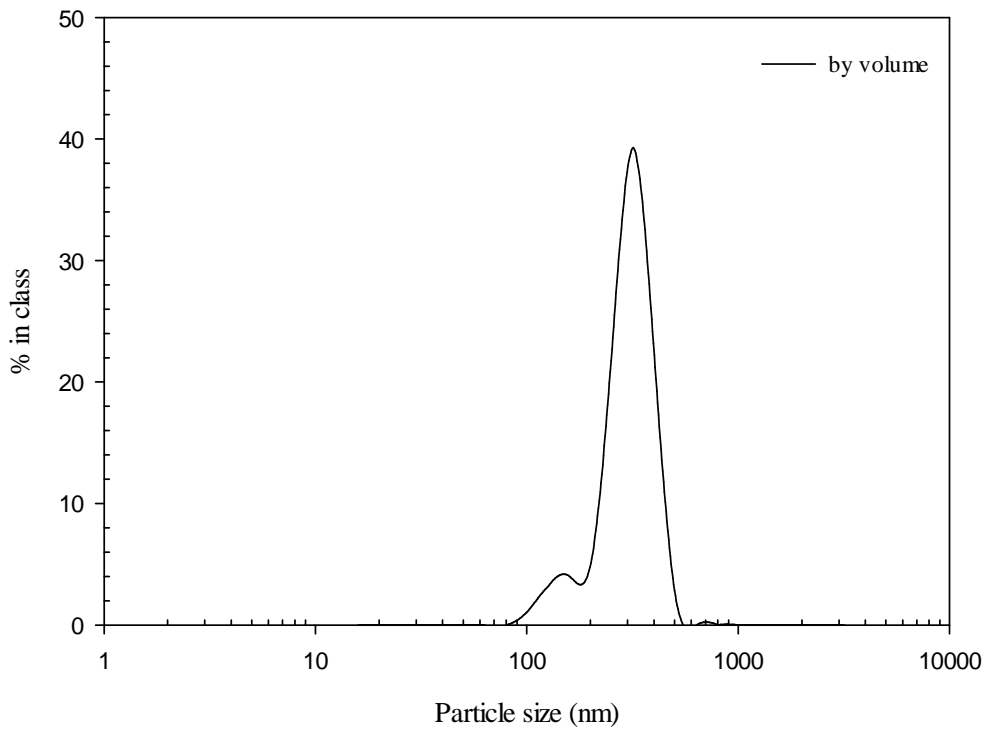


Figure 4.38. The particle size distribution of CT1.

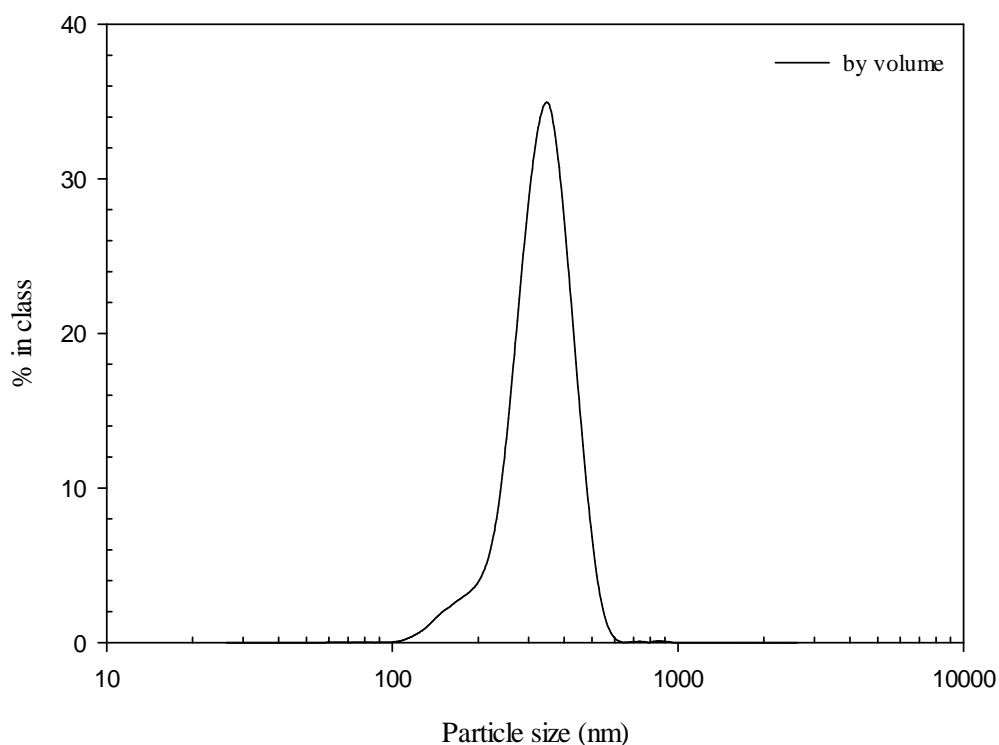


Figure 4.39. The particle size distribution of CT2.

The particle size distribution of the powder CT3 is given in Figure 4.40 which shows polydispersity. The dominant particle size by volume is 437 nm and 60 nm particles show up a little in area by volume although they exist nearly 78% in area by number.

The particle size distribution of the powder CT4 is shown in Figure 4.41. The average particle size is found as 390 nm.

The comparison of the particle size distributions of the titania powders is given in Figure 4.42. Nearly all the powders possess polydispersity. CT3 has the biggest particle size. CT1 and CT2 are quite similar. CT4 has also particles below 100 nm.

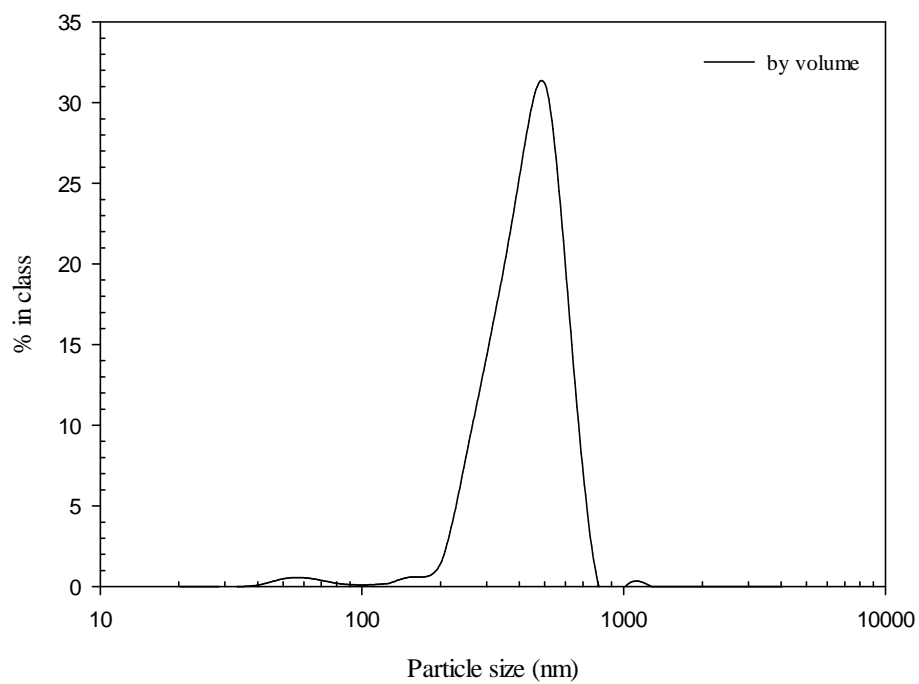


Figure 4.40. The particle size distribution of CT3.

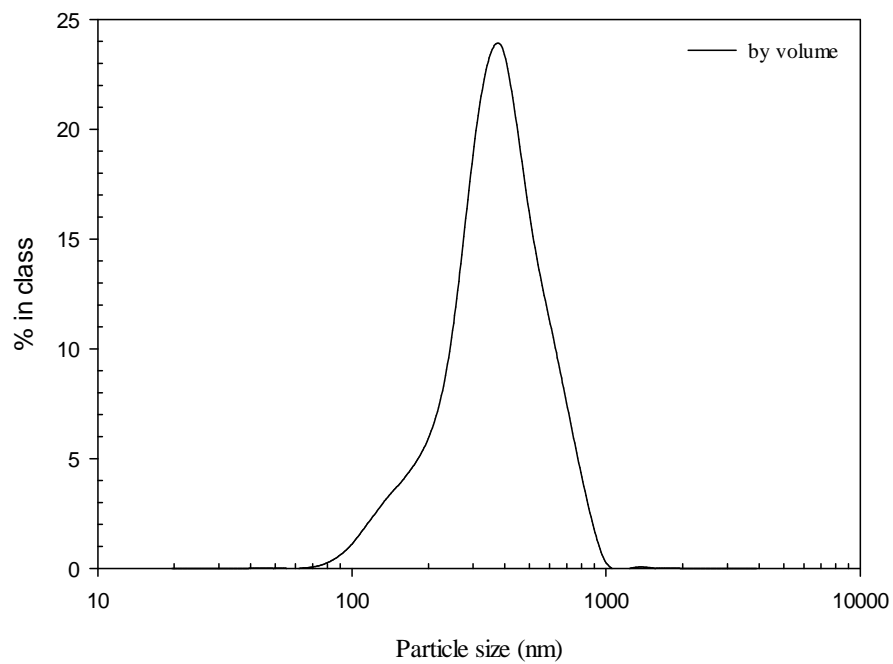


Figure 4.41. The particle size distribution of CT4.

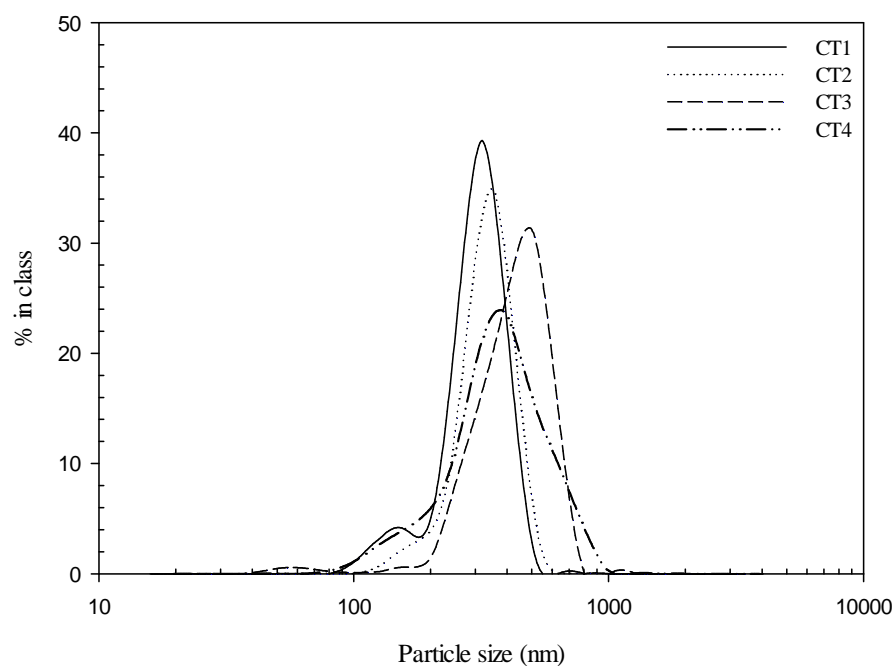


Figure 4.42. The comparison of the particle size distributions of titania powders.

The SEM pictures of the powders CT1, CT2, CT3 and CT4 are seen between Figures 4.43 and 4.46 respectively. The particles can be said to be polycrystalline according to the SEM pictures.

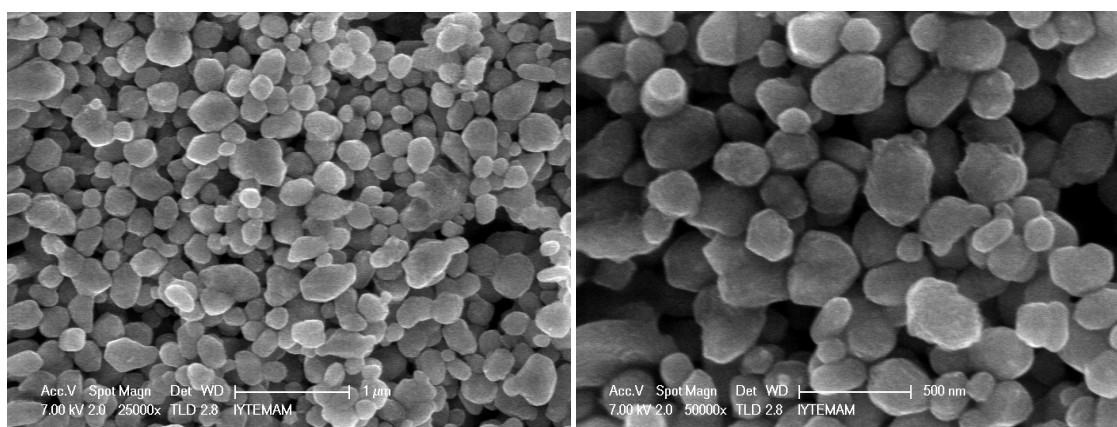


Figure 4.43. The SEM micrographs of powder CT1.

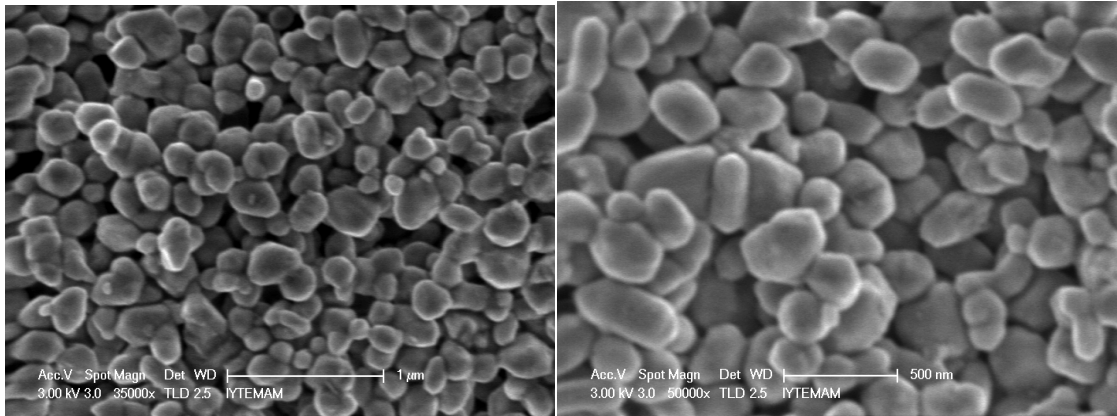


Figure 4.44. The SEM micrographs of powder CT2.

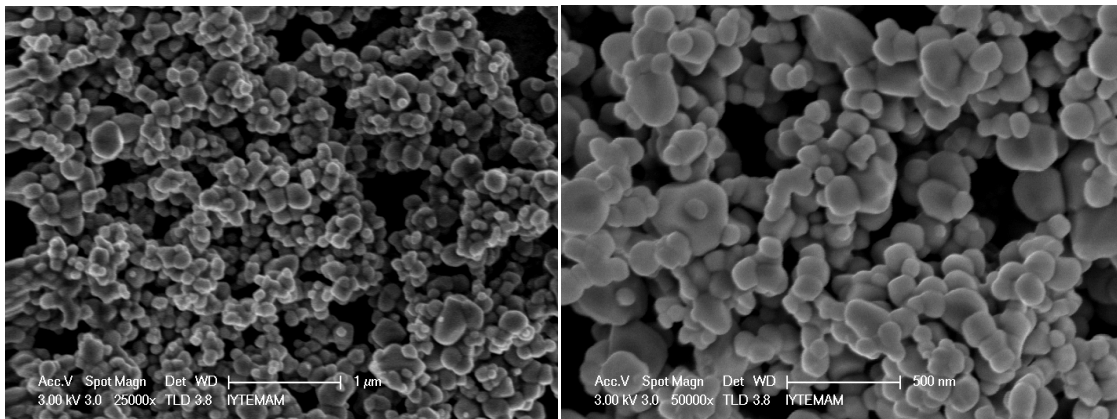


Figure 4.45. The SEM micrographs of powder CT3.

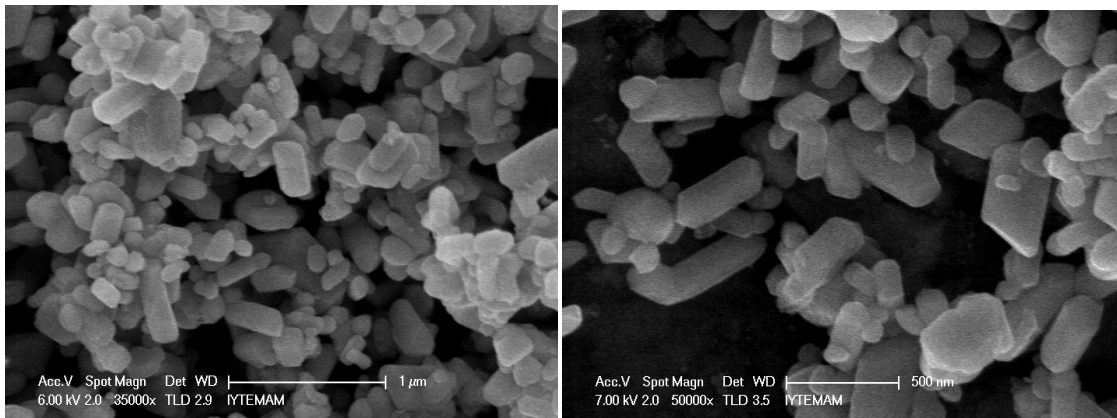


Figure 4.46. The SEM micrograph of powder CT4.

## 4.2.2. Rheological Behaviour of TiO<sub>2</sub> Suspensions

All the TiO<sub>2</sub> particles were dispersed in ethylene glycol which is a non-aqueous medium in order to prevent the evaporation of water in the applications of these suspensions. The flow and dynamic viscosity curves of pure ethylene glycol are given in the Figures 4.47 and 4.49. The dynamic viscosity of ethylene glycol was measured at 20°C as 0.03 Pa.s as seen in Figure 4.49 which is greater than the dynamic viscosity of water,  $1 \times 10^{-3}$  Pa.s.

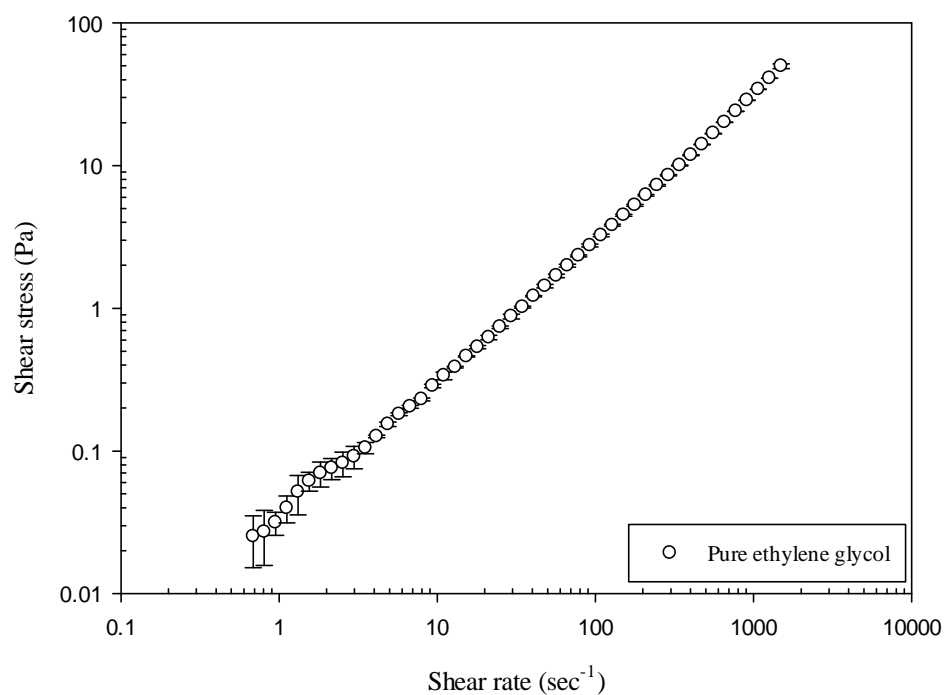


Figure 4.47. Flow curve of pure ethylene glycol.

The fit of the data to power law of pure ethylene glycol is displayed in Figure 4.48. The  $n$  value was found as 1 with a value of  $R^2 = 0.9997$  which indicates that pure ethylene glycol is a Newtonian fluid.

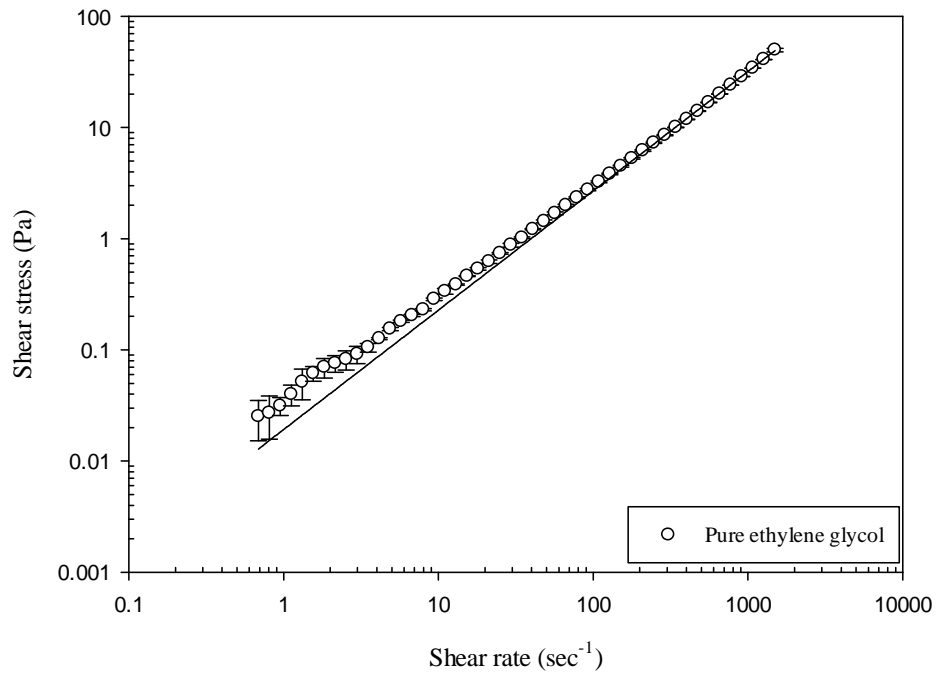


Figure 4.48. Flow curve of pure ethylene glycol (the solid line represents the power model).

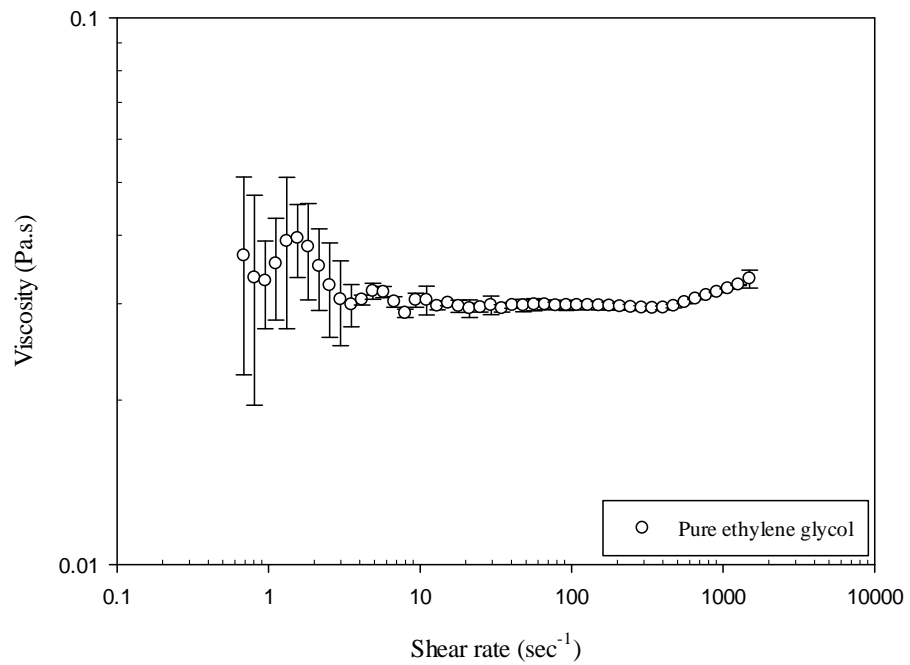


Figure 4.49. The Dynamic viscosity curve of pure ethylene glycol.

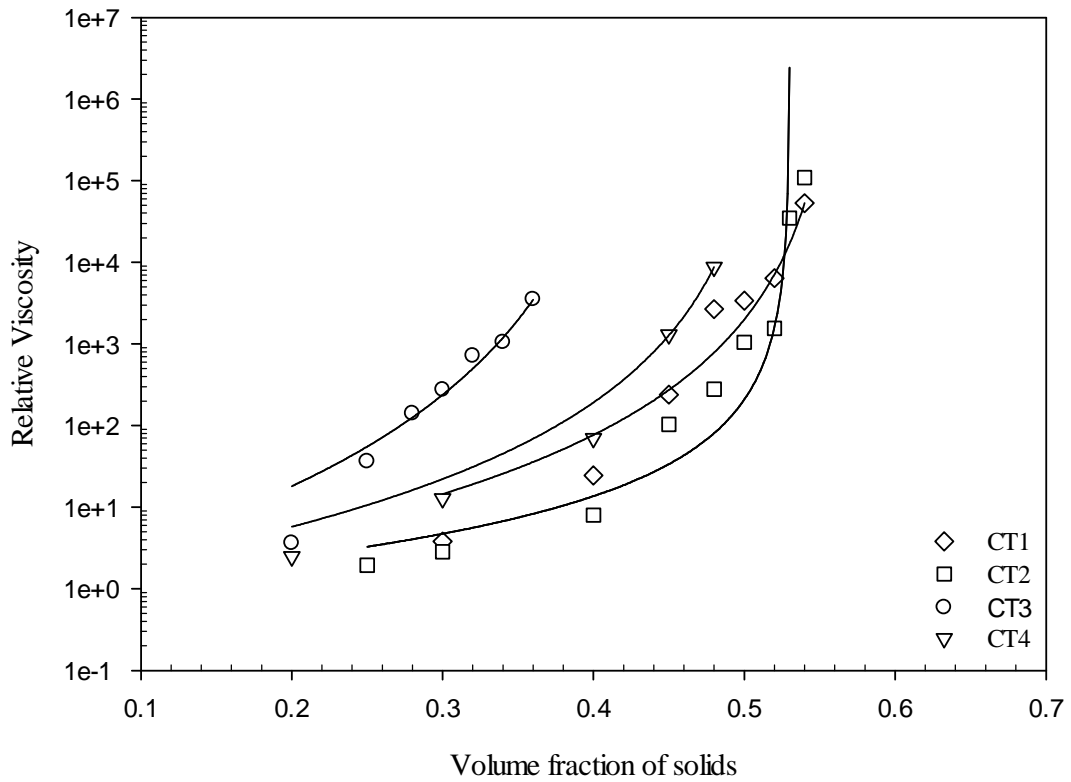


Figure 4.50. Relative high shear viscosity as a function of volume fraction of solids for the commercial TiO<sub>2</sub> powders

The relative viscosities were calculated with Equation 4.7 for all the TiO<sub>2</sub> powders and the experimental data were fitted to the modified Krieger-Dougherty model (see Equation 4.8) as seen in Figure 4.50 in order to find out the fitting parameters  $\Phi_m$  and  $n$  (Bergström, 1998; Bergström; 1996). The maximum volume fraction  $\Phi_m$  accounts for the approach to infinite viscosity (solid body) at some critical volume fraction of solids. The fitting parameter  $n$  is used to describe the increase in viscosity with particle concentration. The best fit of the experimental data to Equation 4.8 is given in the Table 4.2.1.

$$\eta_r = \frac{\eta_{suspension,max}}{\eta_{ethylene\ glycol}} \quad (4.7)$$

$$\eta_r = \left(1 - \frac{\phi}{\phi_m}\right)^{-n} \quad (4.8)$$

Table 4.3. The model parameters of modified Krieger-Dougherty model for the suspensions of titania powders.

	$\Phi_m$	n	$R^2$
CT1	0.56	3.5433	0.9973
CT2	0.53	1.8605	0.9996
CT3	0.44	4.7681	0.9923
CT4	0.52	3.6325	0.9997

The maximum volume fraction  $\Phi_m$  were found as 0.56, 0.53, 0.44 and 0.52 respectively for the powders of CT1, CT2, CT3 and CT4 as seen in Table 4.3.

The dynamic viscosity curves of powder CT1 are displayed in Figure 4.51. The  $\text{TiO}_2$  particles were suspended in ethylene glycol. The solid concentration changed from 5 to 35 vol%. The upper limit was 35 vol% for powder CT1 without surfactant. The viscosity of the suspension decreased as the shear rate increased. The flow curves of the powder CT1 in ethylene glycol was given in Figure 4.52. There is almost a linear increase in the shear stress versus shear rate data. The CT1 suspension in ethylene glycol showed shear-thinning behaviour up to  $1500 \text{ sec}^{-1}$ .

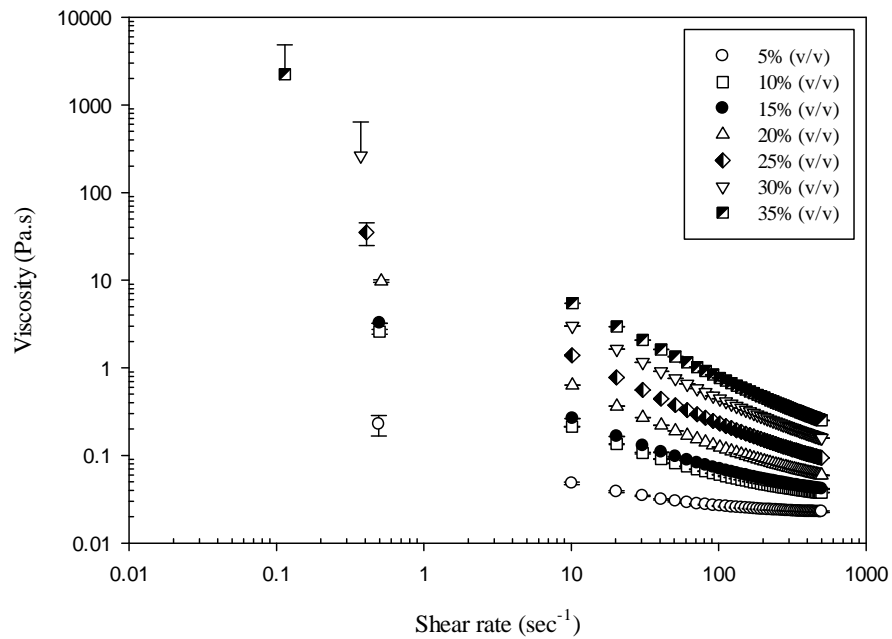


Figure 4.51. The dynamic viscosity curves of the suspensions CT1 in ethylene glycol at different solids contents without surfactant.

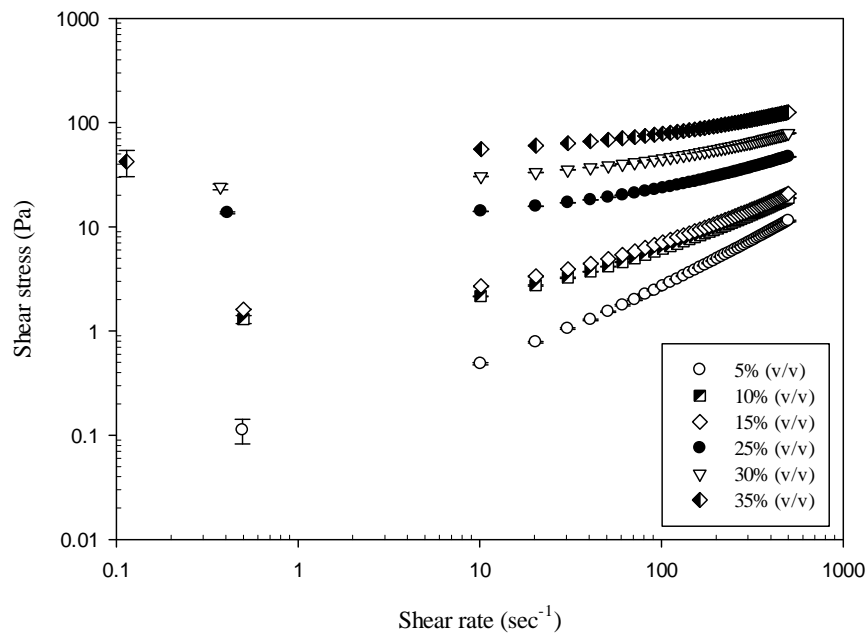


Figure 4.52. Flow curves of the suspensions CT1 in ethylene glycol at different solids contents without surfactant.

A sodium polyacrylate surfactant was used in order to prepare more concentrated suspensions of powder CT1 in ethylene glycol. The viscosity drops dramatically, often by 3 to 4 orders of magnitude as increasing amounts of dispersant are added to a flocculated system (Conley, 1996) which can be seen in the Figure 4.55. A 30 vol% suspension of CT1 powder was prepared in ethylene glycol in the presence and in the absence of the surfactant separately. The viscosity of the suspension without surfactant is nearly constant while there is a significant decrease in the suspension with surfactant. The optimum dispersant demand is attained at the minimum point on the plot of viscosity as a function of dispersant level for different solid loadings of powder CT1 in ethylene glycol in Figure 4.53. The minimum dispersant level was found as 0.4% surfactant weight per solid weight for all solid loadings. The amount of dispersant was assumed as the same value for the following rheology measurements for different solids contents of CT1 in ethylene glycol. The static viscosity curves of CT1 at different solids contents in ethylene glycol with optimized amount of surfactant are shown in Figure 4.54.

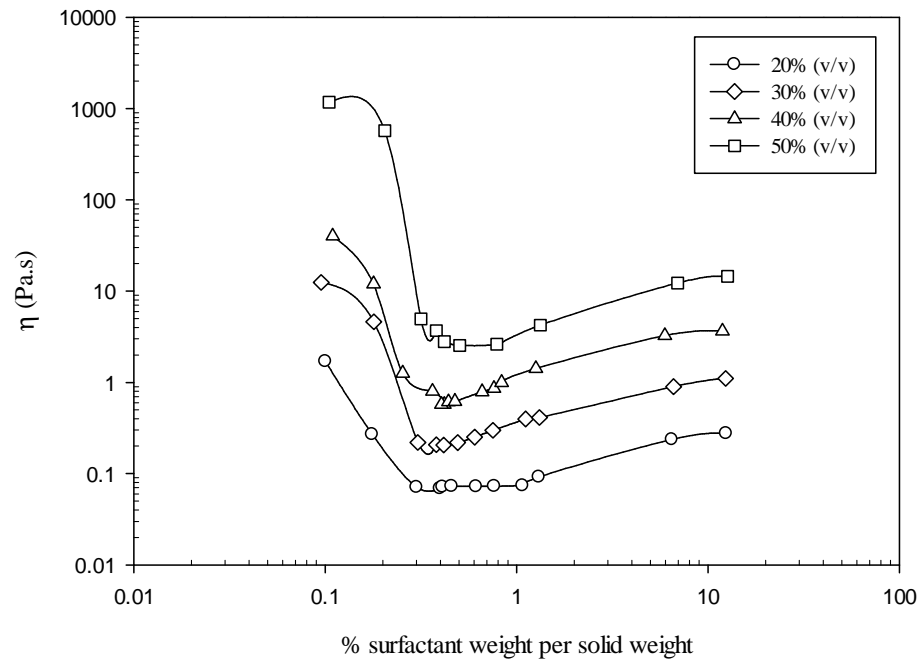


Figure 4.53. Viscosity versus the amount of surfactant added per CT1 weight at different solids contents.

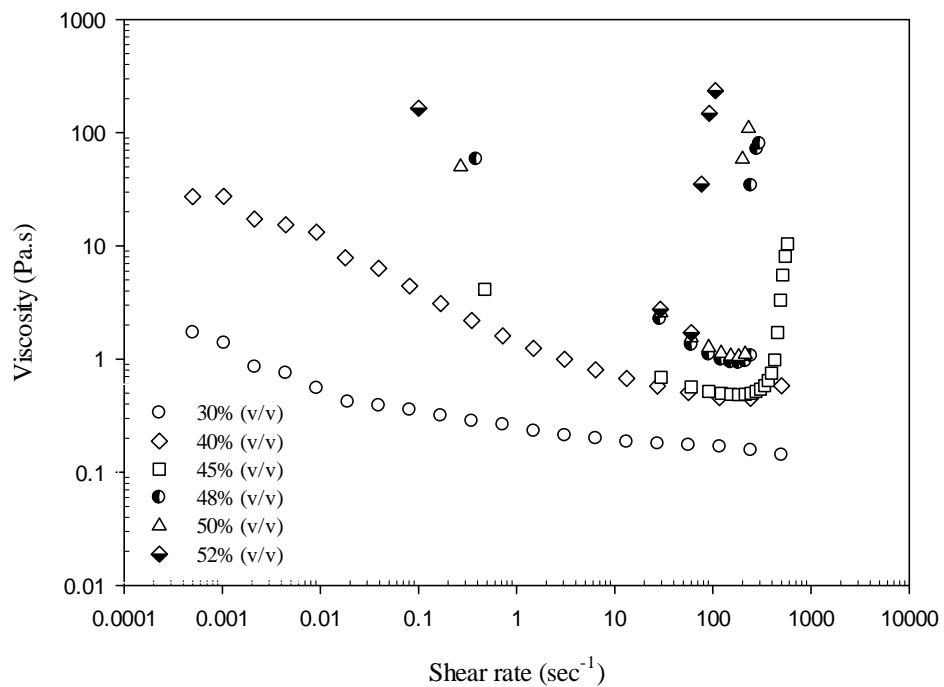


Figure 4.54. The static viscosity curves of the suspensions of CT1 in ethylene glycol at different solids contents with optimized amount of surfactant.

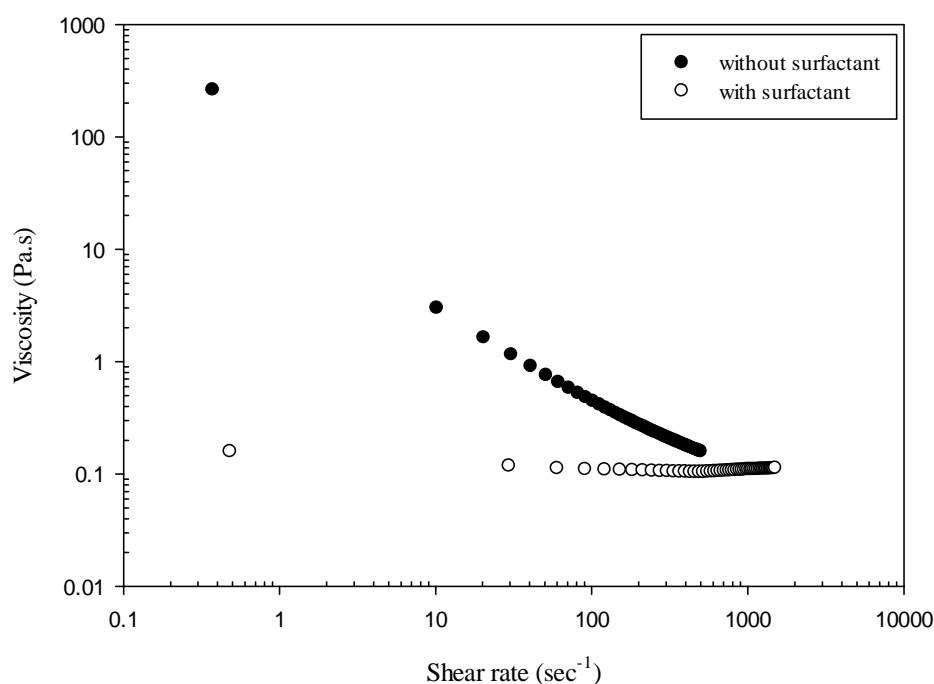


Figure 4.55. Comparison of the viscosity curves of 30 vol% suspension of CT1 in ethylene glycol with and without surfactant.

The rheology measurements of CT1 in ethylene glycol with optimized amount of surfactant were done in the range of solids contents from 30 to 54 vol%. The shear thickening behaviour was firstly seen in the volume fraction  $\Phi=0.4$ . The shear stress is no longer linear at the high shear rates and the viscosity increases with shear rate, which shows resistance to flow in the suspension in the Figures 4.56 and 4.57.

The Table 4.4 gives information about the zero, critic and maximum values of viscosity, shear rate and shear stress of CT1-ethylene glycol suspensions in the presence of surfactant. The values of  $\eta_c$ ,  $\sigma_c$ ,  $\eta_{max}$ , and  $\sigma_{max}$  also increase, whereas the values of  $\gamma_c$  and  $\gamma_{max}$  decrease when  $\Phi$  increases as seen in the table.

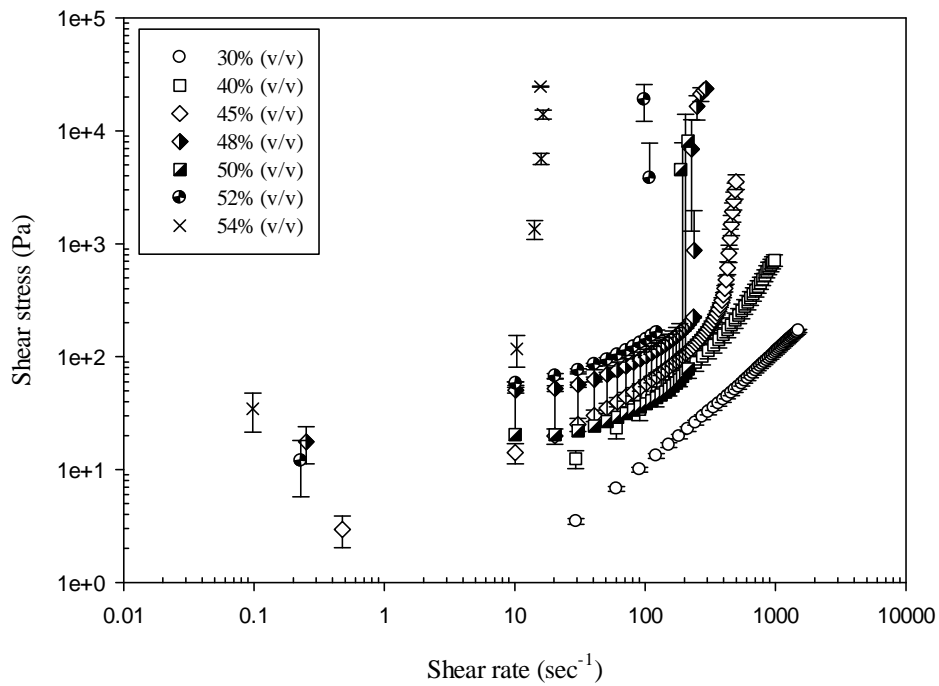


Figure 4.56. Flow curves of the suspensions of CT1 in ethylene glycol at different solids contents with optimized amount of surfactant.

The fit of shear stress versus shear rate data to Power Law was applied on the plot in Figure 4.58. The dependence of  $S$  on  $\dot{\gamma}$  can usually be represented by the Power Law (see Equation 4.9) (Hunter, 2001).

$$S = K\dot{\gamma}^n \quad (4.9)$$

The calculated  $K$ ,  $n$  and  $R^2$  values were listed in Table 4.5. The Power law was utilised separately for shear-thinning and shear-thickening regions. The results show the  $n$  values are smaller than 1 for shear-thinning region and bigger than 1 for shear-thickening region. Therefore, the Power law model is said to be valid for the suspension of CT1 in ethylene glycol with optimum amount of surfactant.

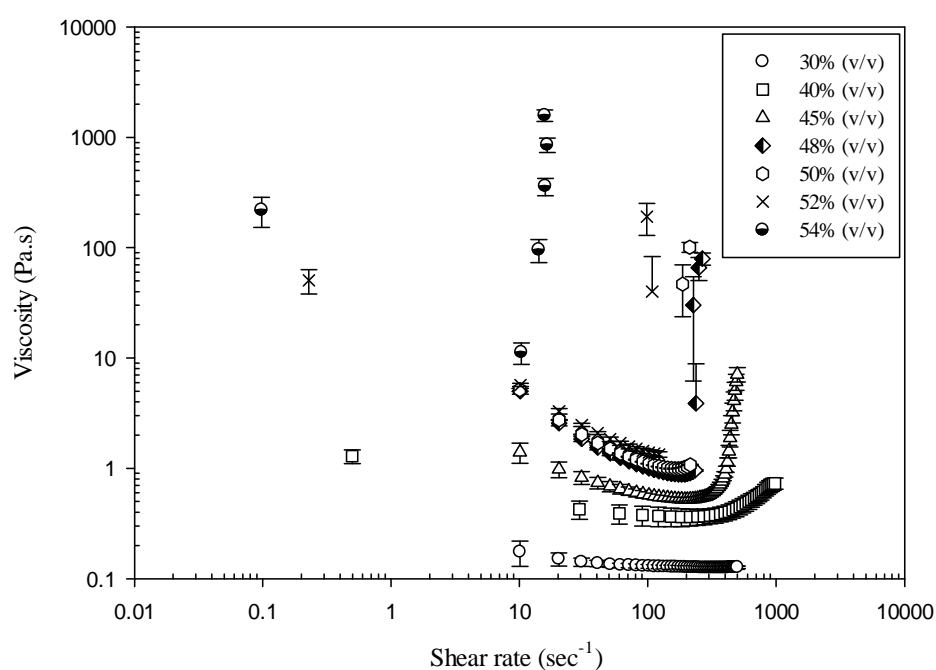


Figure 4.57. The dynamic viscosity curves of the suspensions powder CT1 in ethylene glycol at different solids contents with optimized amount of surfactant.

Table 4.4. The zero, critic and maximum values of viscosity, shear rate and shear stress of CT1-ethylene glycol suspensions with optimum amount of surfactant.

$\Phi$	$\eta_0$	$\sigma_0$	$\gamma_0$	$\eta_c$	$\sigma_c$	$\gamma_c$	$\eta_{max}$	$\sigma_{max}$	$\gamma_{max}$
0.3	0.1588	0.0780	0.48	0.1038	50.79	488.26	0.1130	169.33	1499
0.4	1.2880	0.6410	0.49	0.3637	77.44	213.06	0.7303	714.50	978
0.45	6.2033	2.9537	0.47	0.5240	106.93	203.96	7.1233	3550.6	498
0.48	69.323	17.61	0.25	0.8803	161.50	183.43	79.576	21193	266
0.5	47.693	39.786	0.30	0.9920	55.058	163	101.01	8157.1	213
0.52	50.576	11.935	0.22	1.3380	163.53	122	190.46	18903.	98
0.54	219.00	34.566	0.097	11.242	117.35	10.33	1580.3	24670	15.8

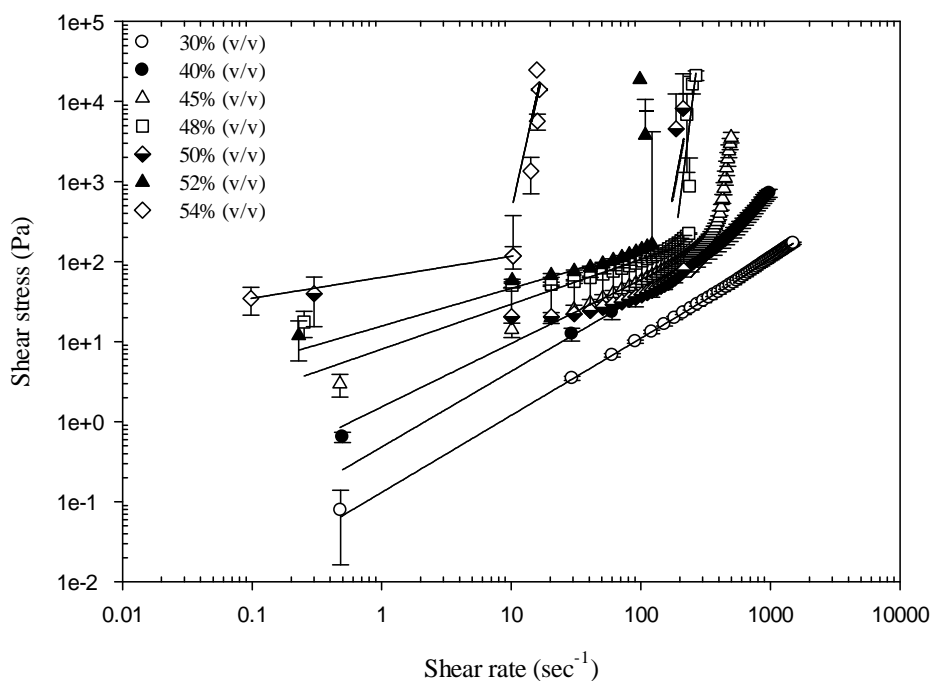


Figure 4.58. Flow curves of the suspensions of CT1 in ethylene glycol with optimized amount of surfactant (the solid lines represent the power law model).

Table 4.5. The model parameters of Power Law for the suspensions of CT1 in ethylene glycol with optimized amount of surfactant.

vol %	Shear-thinning region			Shear-thickening region		
	$K_I$	$n_I$	$R^2$	$K_{II}$	$n_{II}$	$R^2$
30	0.1308	0.9625	1.0000	0.0672	1.0706	1.0000
40	0.4830	0.9459	0.9998	0.0046	1.7349	0.9962
45	1.5299	0.7929	0.9959	5.2881E-025	10.3179	0.9838
48	8.0442	0.5612	0.9585	5.0266E-028	13.0523	0.8077
50	11.6695	0.2658	0.2712	3.8065E-017	8.5638	0.1200
52	15.6514	0.4708	0.9805	7625.8208	4.4046E-019	-2.9310E-014
54	63.6091	0.2623	1.0000	2.2105E-005	7.2908	0.4424

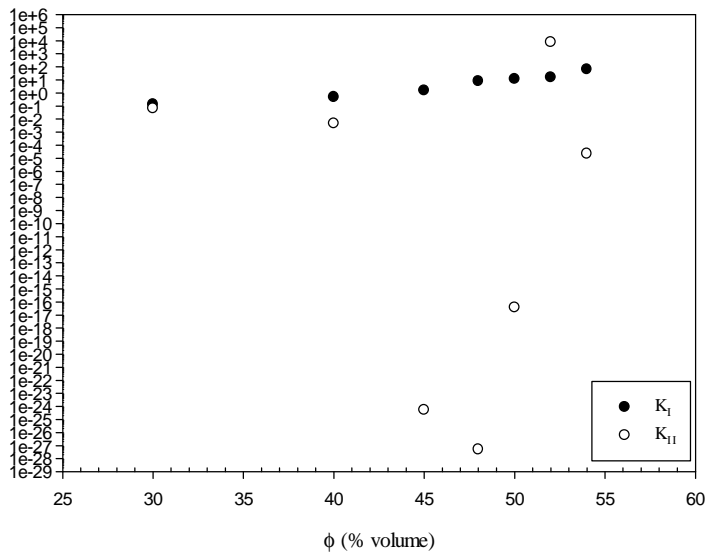


Figure 4.59. Calculated  $K_I$  and  $K_{II}$  values of the Power law model for the suspensions of CT1 in ethylene glycol with optimized amount of surfactant at different solids contents.

The comparison of  $K_I$  and  $K_{II}$  values is displayed in Figure 4.59.  $K_I$  values increase with increasing  $\Phi$  and  $K_{II}$  values initially decrease and then increase at high  $\Phi$  values (0.5, 0.52, 0.54) having low values of  $R^2$ .

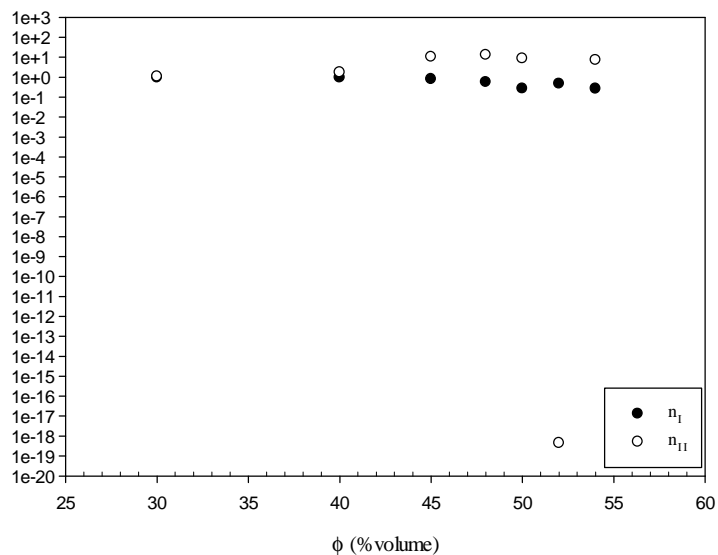


Figure 4.60. Calculated  $n_I$  and  $n_{II}$  values of the modified Power law model for the suspensions of CT1 in ethylene glycol with optimized amount of surfactant at different solids contents.

The comparison of  $n_I$  and  $n_{II}$  values is displayed in Figure 4.60. The  $n_I$  values are smaller than 1 which proves that this region is shear-thinning. The  $n_{II}$  values are just like the symmetry of  $n_I$  values above 1. The  $n_I$  and  $n_{II}$  values are almost 1 at  $\Phi=0.3$  which can be assumed as a Newtonian fluid. The  $n_I$  values decrease whereas  $n_{II}$  values increase as the solids contents increase in the suspension.

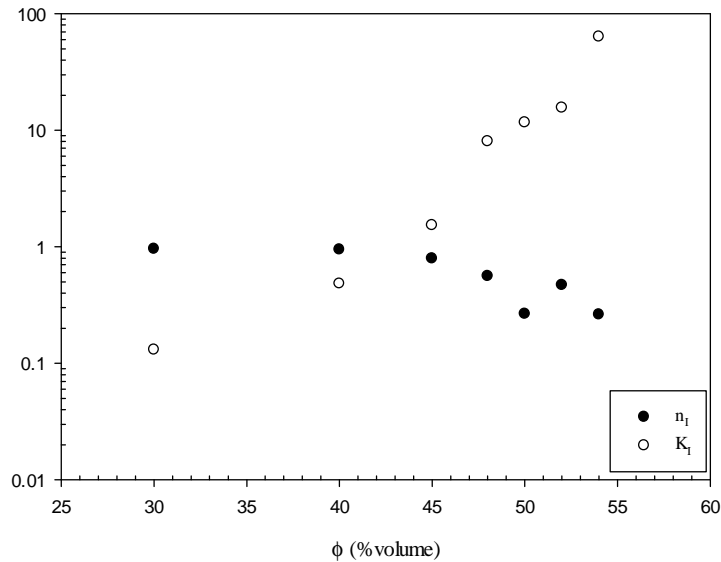


Figure 4.61. Calculated  $n_I$  and  $K_I$  values of Power law model for the suspensions of CT1 in ethylene glycol with optimized amount of surfactant at different solids contents.

The  $n_I$  values decrease with increasing solids contents whereas  $K_I$  values increase as seen in Figure 4.61. The  $n_{II}$  values increase with increasing solids contents while  $K_{II}$  values decrease for the values of  $\Phi=0.3, 0.4, 0.45$  and  $0.48$  as seen in Figure 4.62.

The modified Cross Model viscosity function which was proposed by Galindo-Rosales et al. for shear thickening behaviour was used as a shear-thickening model. This function (see Equation 4.11) was able to cover the three regions characteristic of the general viscosity curve exhibited by shear thickening fluids as seen in the Equation.4.10. There is no zone III in our data which is characterised by a steep shear thinning behaviour for values of  $\gamma > \gamma_{max}$ . The second shear-thinning region is not seen in our data because the maximum torque capacity of the rheometre was not capable for analyzing third region.

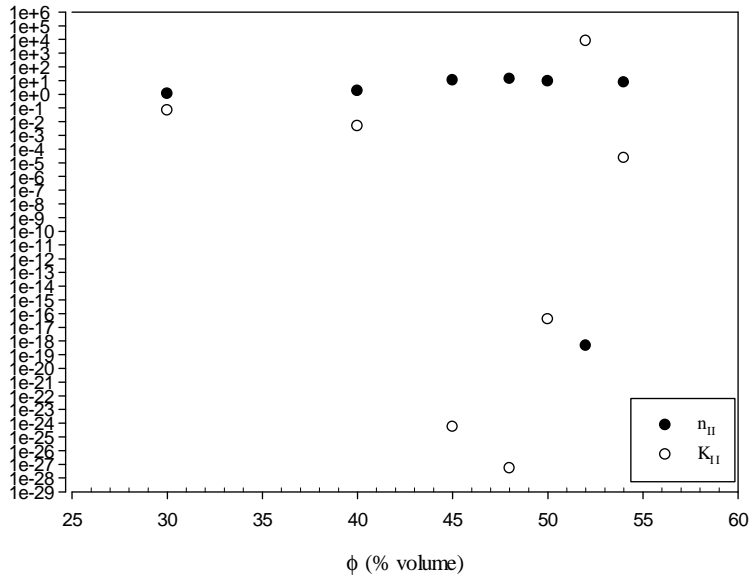


Figure 4.62. Calculated  $n_{II}$  and  $K_{II}$  values of Power law model for the suspensions of CT1 in ethylene glycol with optimized amount of surfactant at different solids contents.

This model was applied to zone I, where a slight shear thinning behaviour exists up to a critical shear rate and zone II, in which shear thickening takes place between  $\dot{\gamma}_c$  and a higher critical value  $\dot{\gamma}_{max}$ , where the apparent viscosity takes its maximum value.

$$\eta(\dot{\gamma}) = \begin{cases} \eta_I(\dot{\gamma}) & \text{for } \dot{\gamma} \leq \dot{\gamma}_c \\ \eta_{II}(\dot{\gamma}) & \text{for } \dot{\gamma}_c < \dot{\gamma} \leq \dot{\gamma}_{max} \\ \eta_{III}(\dot{\gamma}) & \text{for } \dot{\gamma}_{max} < \dot{\gamma} \end{cases}$$

(4.10)

$$\eta(\dot{\gamma}) = \begin{cases} \eta_I(\dot{\gamma}) = \eta_c + \frac{\eta_0 - \eta_c}{1 + [K_I(\dot{\gamma}^2 / (\dot{\gamma} - \dot{\gamma}_c))]^{n_I}} & \text{for } \dot{\gamma} \leq \dot{\gamma}_c \\ \eta_{II}(\dot{\gamma}) = \eta_{max} + \frac{\eta_c - \eta_{max}}{1 + [K_{II}((\dot{\gamma} - \dot{\gamma}_c) / (\dot{\gamma} - \dot{\gamma}_{max}))\dot{\gamma}]^{n_{II}}} & \text{for } \dot{\gamma}_c < \dot{\gamma} \leq \dot{\gamma}_{max} \\ \eta_{III}(\dot{\gamma}) = \frac{\eta_{max}}{1 + [K_{III}(\dot{\gamma} - \dot{\gamma}_{max})]^{n_{III}}} & \text{for } \dot{\gamma}_{max} < \dot{\gamma} \end{cases} \quad (4.11)$$

The fit of the viscosity versus shear rate data to the modified Cross Model can be seen on the plot of in Figure 4.63 and the calculated  $K$ ,  $n$  and  $R^2$  values for both shear-thinning and shear-thickening regions were listed in Table 4.2.4. The fitting could

not be applied on the data of the suspensions 54 vol% in zone I and 52 vol% in zone II due to the lack of data. The curves do not seem to fit well to the data although the  $R^2$  values are close to 1 in the shear-thinning region, which could be because of the zero-shear rate viscosity values. On the other hand, the curves seem to fit well in the shear-thickening region.

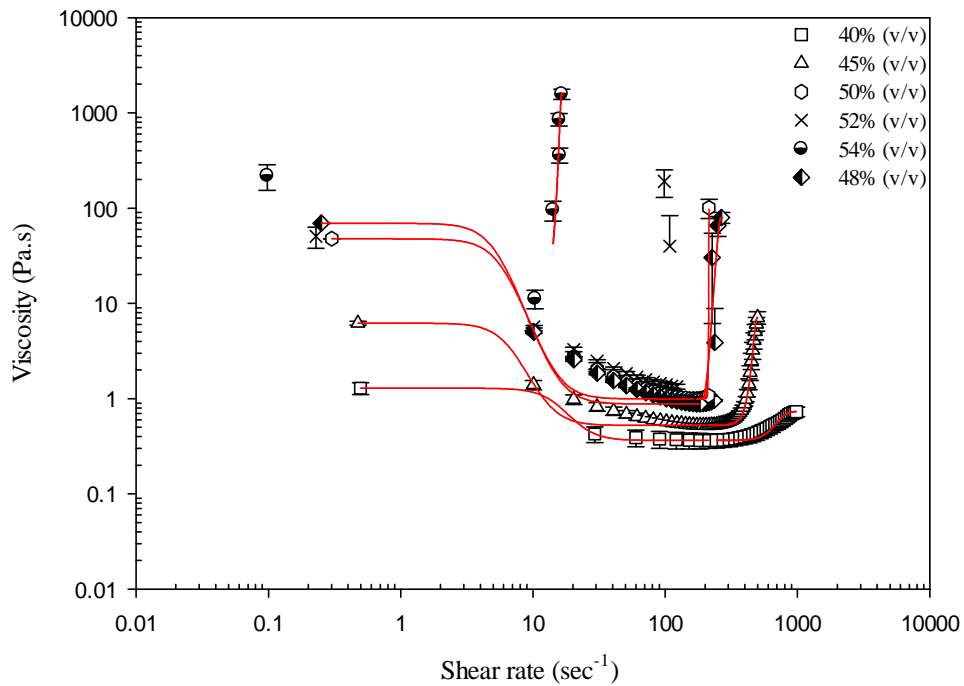


Figure 4.63. Dynamic viscosity curves of the suspensions of CT1 in ethylene glycol with optimized amount of surfactant (the solid lines represent the modified cross model).

Table 4.6. The model parameters of the modified Cross Model for the suspensions of CT1 in ethylene glycol with optimized amount of surfactant

Solids content	Shear-thinning region			Shear-thickening region		
	$K_I$	$n_I$	$R^2$	$K_{II}$	$n_{II}$	$R^2$
40 vol %	0.7907	2	0.9990	0.0009	2	0.9176
45 vol %	4.3566	2	0.9882	0.0003	2	0.9920
48 vol %	6.5762	2	0.9991	0.0013	2	0.8432
50 vol %	4.7597	2	0.9978	3.1679E-005	2	0.9969
52 vol %	3.4331	2	0.9976	-	-	-
54 vol %	-	-	-	0.0060	2	0.8424

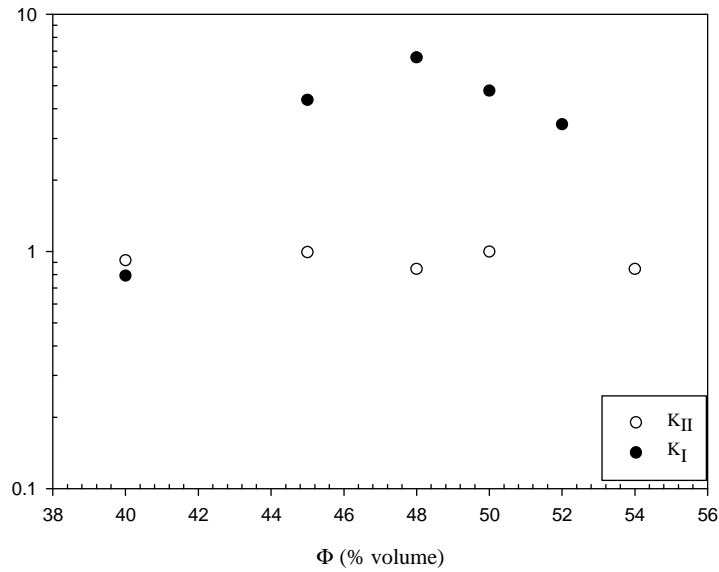


Figure 4.64. Calculated  $K_I$  and  $K_{II}$  values of the modified Cross model for the suspensions of CT1 in ethylene glycol with optimized amount of surfactant.

The calculated  $K_I$  and  $K_{II}$  values of the modified Cross model are displayed in Figure 4.64. The values of  $K_I$  are greater than  $K_{II}$ . The  $n$  values are constant which is equal to 2 as seen in the Table 4.6.

The static viscosity curves of the suspensions of CT2 in ethylene glycol at different solids contents are given in Figure 4.65.

The rheology measurements of the suspensions of CT2 in ethylene glycol without any surfactant were done in the range of volume percentages from 25 to 54 vol%. The shear thickening behaviour was firstly seen at  $\Phi = 0.4$ . The shear stress is no longer linear at the high shear rates and the viscosity increases with increasing shear rate, which shows resistance to flow in the suspension as seen in the Figure 4.66 and 4.67.

The Table 4.7 gives information about the zero, critic and maximum values of viscosity, shear rate and shear stress of CT2-ethylene glycol suspensions. As seen in the table when  $\Phi$  increases, the values of  $\eta_c$ ,  $\sigma_c$ ,  $\eta_{max}$ , and  $\sigma_{max}$  also increase, whereas the values of  $\gamma_c$  decrease.

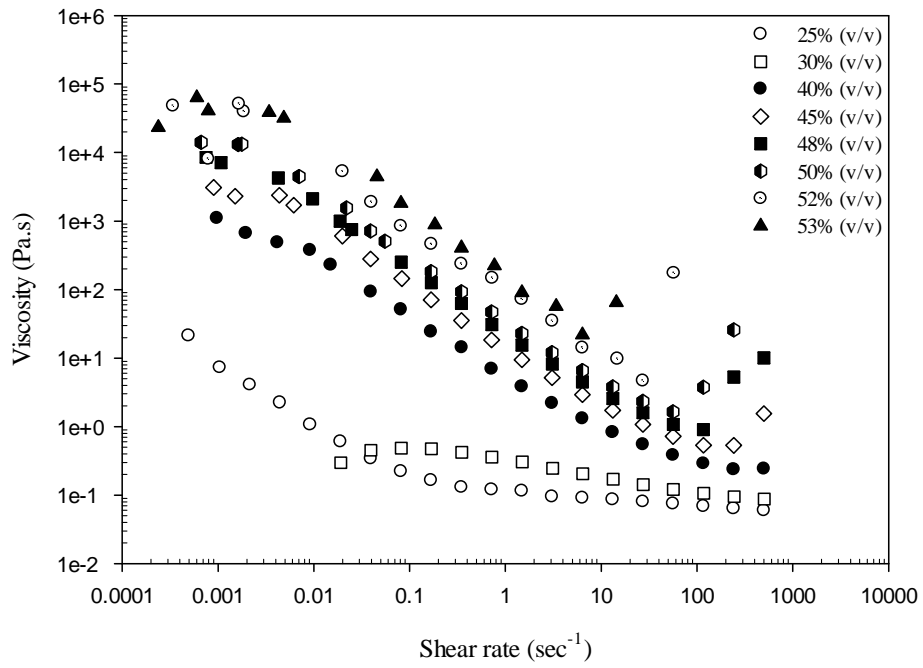


Figure 4.65. Static viscosity curves of the suspensions CT2 in ethylene glycol at different solids contents.

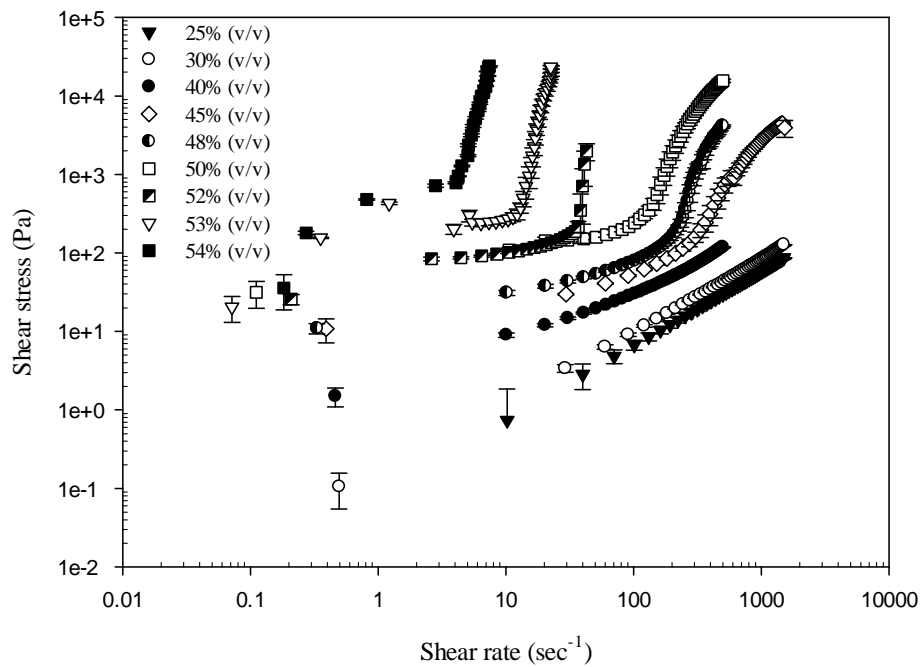


Figure 4.66. Flow curves of the suspensions of CT2 in ethylene glycol at different solids contents.

The fit of shear stress versus shear rate data to Power Law was applied on the plot in Figure 4.68. The calculated  $K$ ,  $n$  and  $R^2$  values were listed in Table 4.8. The Power law was utilised separately for shear-thinning and shear-thickening regions. The results show the  $n$  values are smaller than 1 for shear-thinning region and bigger than 1 for shear-thickening region for the  $\Phi$  values between 0.4 and 0.54. The 25 and 30 vol% suspensions show a Newtonian fluid behaviour because  $n$  values are almost 1. The validity of Power law model can be concluded for the suspension of CT2 in ethylene glycol.

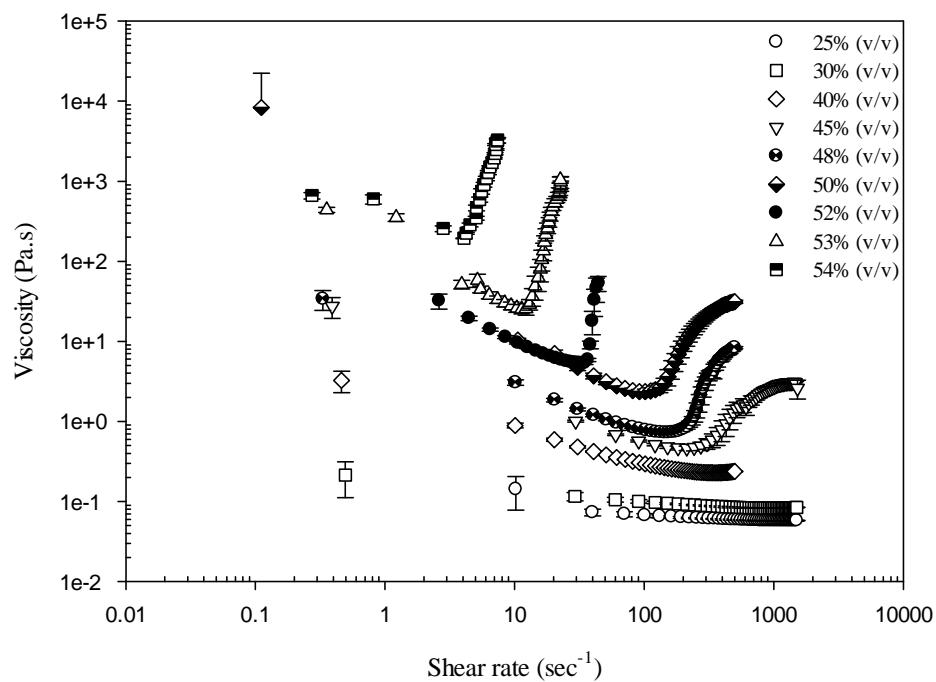


Figure 4.67. Dynamic viscosity curves of the suspensions of powder CT2 in ethylene glycol at different solids content.

Table 4.7. The zero, critic and maximum values of viscosity, shear rate and shear stress of CT2-ethylene glycol suspensions.

$\Phi$	$\eta_0$	$\sigma_0$	$\gamma_0$	$\eta_c$	$\sigma_c$	$\gamma_c$	$\eta_{max}$	$\sigma_{max}$	$\gamma_{max}$
0.25	0.1415	0.7368	10.240	0.057	67.386	1173	0.057	85.510	1479
0.30	0.2127	0.1055	0.4950	0.082	86.180	1041	0.084	126.76	1502
0.40	3.2513	1.4953	0.4623	0.228	81.540	356.9	0.237	118.86	499
0.45	27.306	10.806	0.3913	0.462	98.610	213.03	3.087	4439	1438

(cont. on next page)

Table 4.7. (cont.)

0.48	33.793	10.939	0.3317	0.725	110.83	152.86	8.327	4160	499
0.50	8317.6	31.603	0.1109	2.359	240.16	101.80	31.26	15603	499
0.52	122.70	25.646	0.2083	5.317	174.66	32.846	53.23	1973	44
0.53	439.66	155.66	0.3553	25.30	287.03	11.346	1038	23286	22.5
0.54	661.50	179.76	0.2727	192.3	780.30	4.0570	3259	24040	7.41

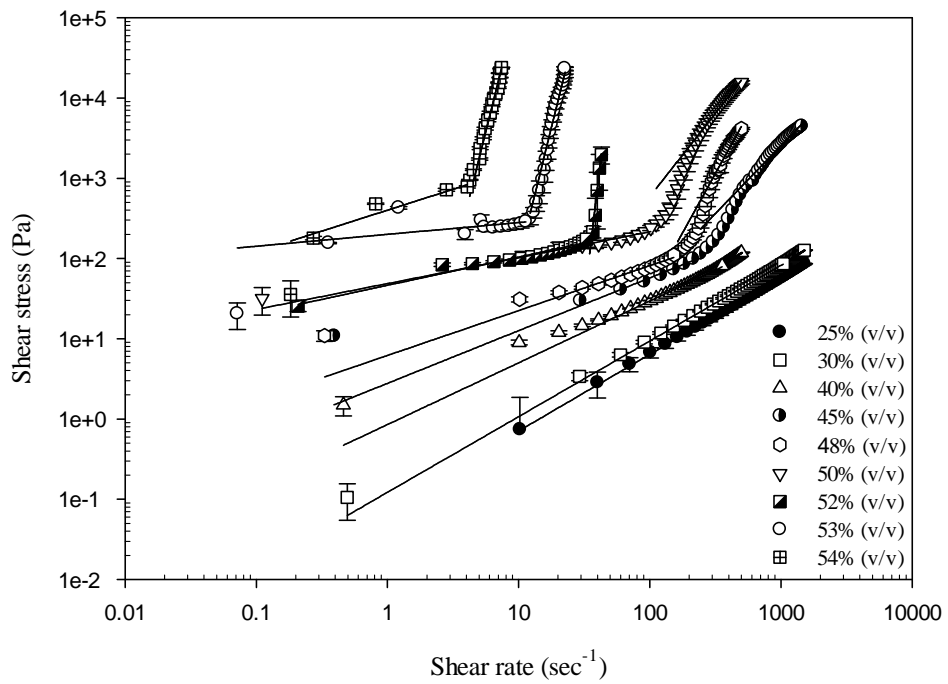


Figure 4.68. Flow curves of the suspensions of CT2 in ethylene glycol at different solids contents (the solid lines represent the power law model).

Table 4.8. The model parameters of Power law model calculated for the suspensions of CT2 in ethylene glycol.

Solids contents	Shear-thinning region			Shear-thickening region		
	$K_I$	$n_I$	$R^2$	$K_{II}$	$n_{II}$	$R^2$
25 vol %	0.0785	0.9548	0.9999	0.0480	1.0253	0.9999
30 vol %	0.1220	0.9427	0.9998	0.0554	1.0573	0.9999
40 vol %	0.8523	0.7697	0.9945	0.1043	1.1318	0.9993
45 vol %	2.7819	0.6570	0.9758	0.0212	1.6930	0.9891
48 vol %	6.1884	0.5595	0.9738	4.6252E-005	2.9575	0.9863
50 vol %	48.6680	0.3227	0.9531	0.0408	2.0791	0.9879
52 vol %	46.3497	0.3516	0.9437	2.4595E-020	14.0472	0.9874
53 vol %	199.7283	0.1472	0.3095	2.5933E-005	6.5708	0.9793
54 vol %	399.6772	0.5211	0.9163	0.0454	6.5691	0.9837

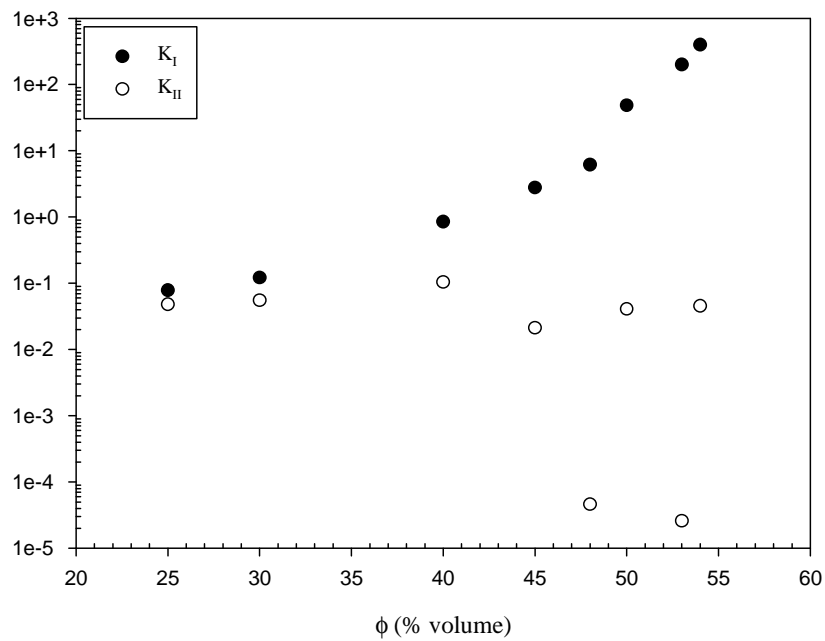


Figure 4.69. Calculated  $K_I$  and  $K_{II}$  values of Power law model for the suspensions of CT2 in ethylene glycol.

The comparison of  $K_I$  and  $K_{II}$  values is displayed in the Figure 4.69. The  $K_I$  values increase with increasing  $\Phi$  values while  $K_{II}$  values almost remain constant with exception of  $\Phi$  values of 0.48 and 0.52.

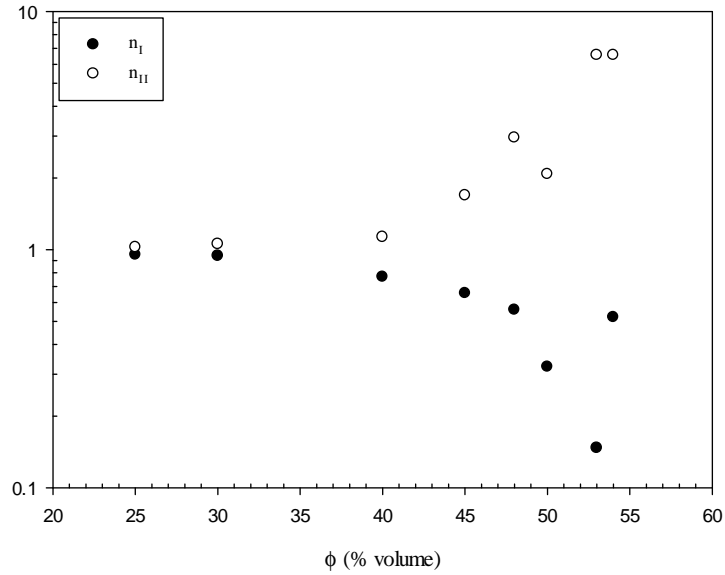


Figure 4.70. Calculated  $n_I$  and  $n_{II}$  values of Power law model for the suspensions of CT2 in ethylene glycol.

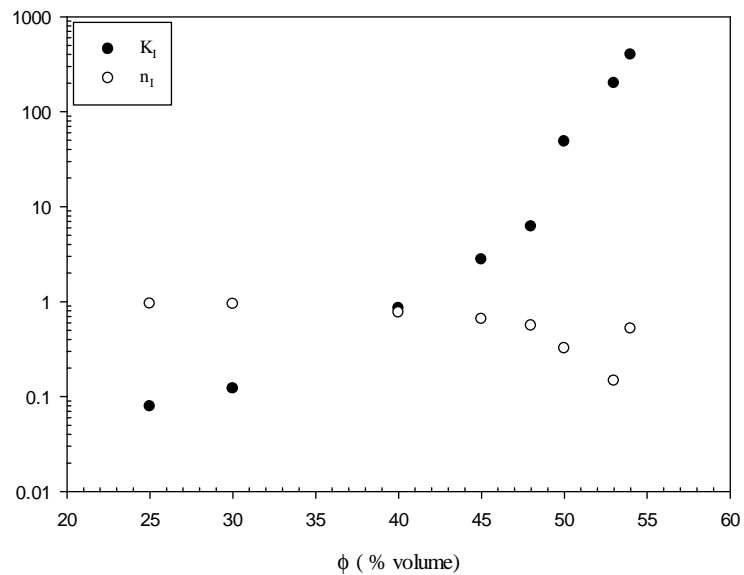


Figure 4.71. Calculated  $n_I$  and  $K_I$  values of Power law model for the suspensions of CT2 in ethylene glycol.

The comparison of  $n_I$  and  $n_{II}$  values is displayed in Figure 4.70. The  $n_I$  values are smaller than 1 which proves that this region is shear-thinning. The  $n_{II}$  values are just like the symmetry of  $n_I$  values above 1. The  $n_I$  and  $n_{II}$  values are almost 1 at  $\Phi=0.25$  and 0.30 which shows a Newtonian fluid behaviour. The  $n_I$  values decrease whereas  $n_{II}$  values increase with increasing solids contents in the suspension. The  $n_I$  values decrease with increasing solids contents while  $K_I$  values increase as seen in Figure 4.71.

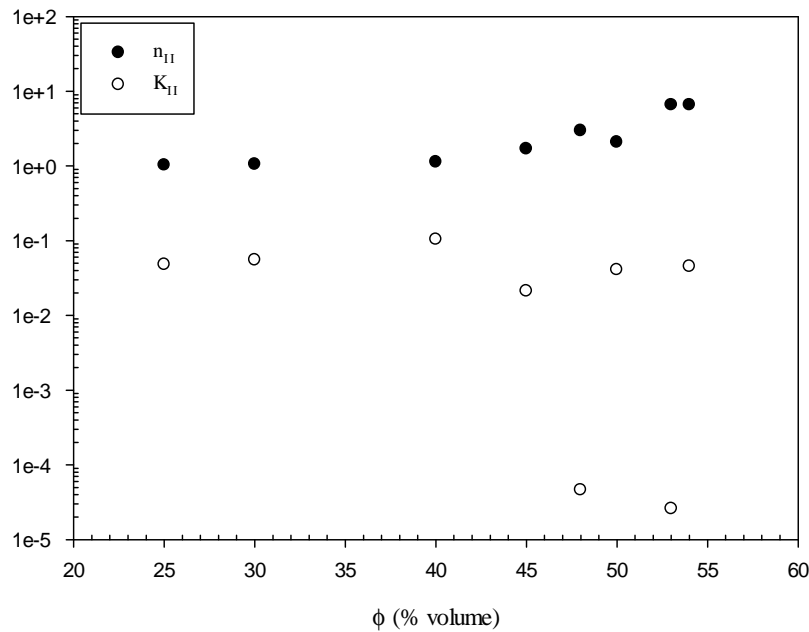


Figure 4.72. Calculated  $n_{II}$  and  $K_{II}$  values of Power law model for the suspensions of CT2 in ethylene glycol.

The  $n_{II}$  values increase with increasing solids contents; however,  $K_{II}$  values remain nearly constant except the  $\Phi=0.48$  and 0.52 as seen in the Figure 4.72.

The fit of viscosity versus shear rate data to the modified Cross Model can be seen on the plot for the suspensions of CT2 in Figure 4.73 and the calculated  $K$ ,  $n$  and  $R^2$  values for both shear-thinning and shear-thickening regions were listed in Table 4.9. The curves do not seem to fit well to the data in the shear-thinning region, although the  $R^2$  values are close to 1. The zero-shear rate viscosity values could lead to this. The curves seem to fit well in the shear-thickening region.

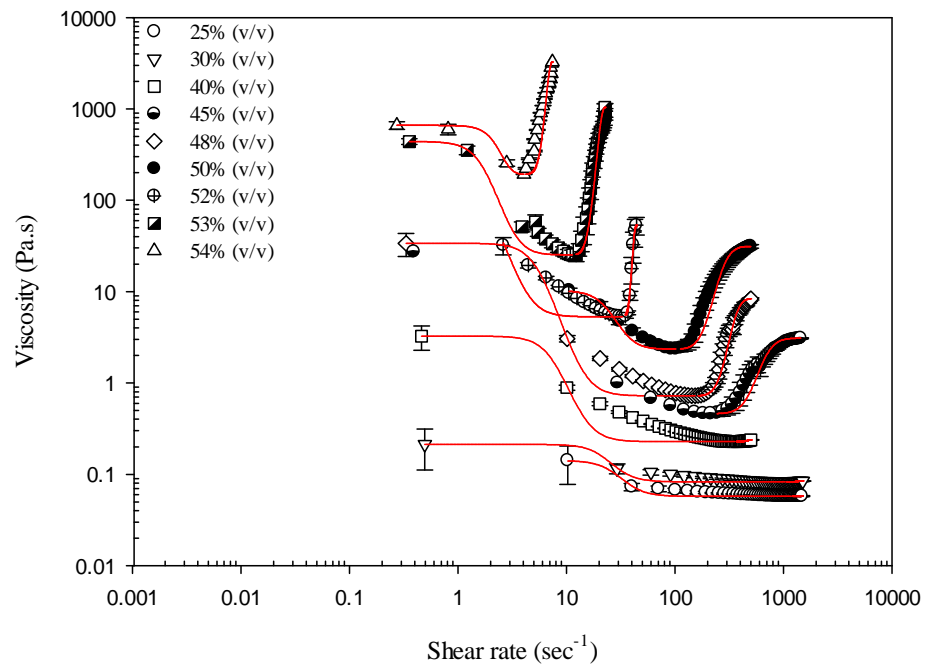


Figure 4.73. Dynamic viscosity curves of the suspensions of CT2 in ethylene glycol at different solids contents (the solid lines represent Modified Cross model).

Table 4.9. The model parameters of the modified Cross Model for the suspensions of CT2 in ethylene glycol

Solids contents	Shear-thinning region			Shear-thickening region		
	$K_I$	$n_I$	$R^2$	$K_{II}$	$n_{II}$	$R^2$
25 vol %	1.3898	2	0.9367	0.0001	2	0.4729
30 vol %	1.9353	2	0.9129	0.0004	2	0.7702
40 vol %	6.2155	2	0.9697	0.0011	2	0.8886
45 vol %	1.4499	2	0.9999	0.0026	2	0.9303
48 vol %	4.9466	2	0.9982	0.0023	2	0.955
50 vol %	0.1355	2	0.9676	0.0050	2	0.9318
52 vol %	7.7643	2	0.6795	0.0091	2	0.9972
53 vol %	3.4275	2	0.9915	0.0150	2	0.8357
54 vol %	0.4107	2	0.9795	0.0428	2	0.8512

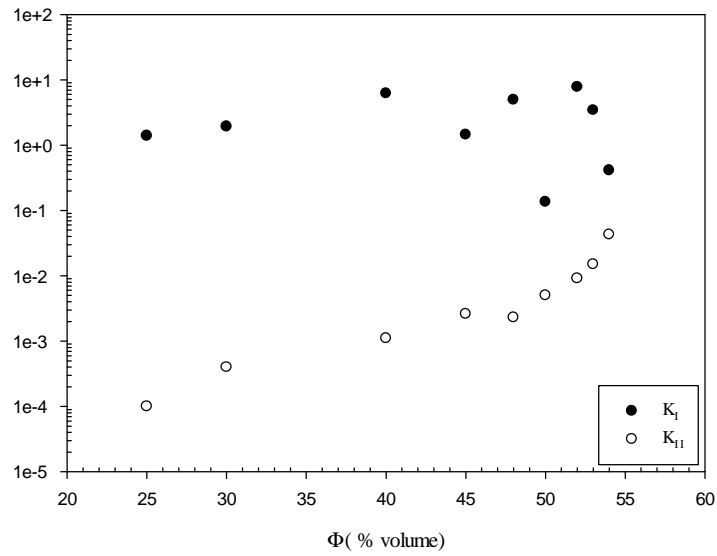


Figure 4.74. Calculated  $K_I$  and  $K_{II}$  values of the modified Cross model for the suspensions of CT2 in ethylene glycol.

The calculated  $K_I$  and  $K_{II}$  values of the modified Cross model are displayed in the Figure 4.74.  $K_I$  values are greater than  $K_{II}$ . The  $n$  values are constant which is equal to 2 as seen in the Table 4.9.

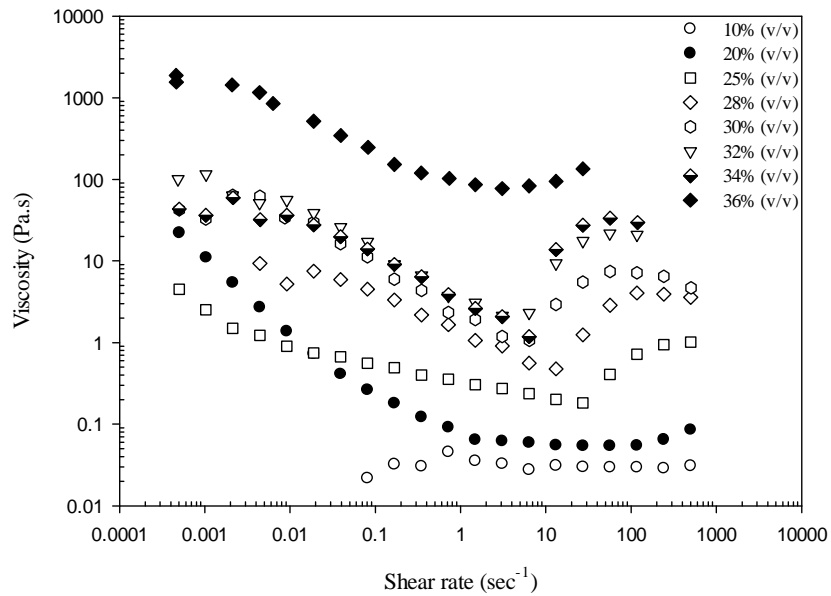


Figure 4.75. Static viscosity curves of the suspensions of CT3 in ethylene glycol at different solids content.

The static viscosity curves of the suspensions CT3 in ethylene glycol at different solids contents is given are shown in Figure 4.75. Table 4.2.8 gives information about the zero, critic and maximum values of viscosity, shear rate and shear stress of CT3-ethylene glycol suspensions. As seen in the table when  $\Phi$  increases, the values of  $\eta_c$ ,  $\sigma_c$ ,  $\eta_{max}$ , and  $\sigma_{max}$  also increase, whereas the values of  $\gamma_c$  and  $\gamma_{max}$  decrease.

The rheology measurements of the suspensions of CT3 in ethylene glycol without any surfactant were done in the range of volume percentages from 10 to 36. The shear thickening behaviour was slightly seen at  $\Phi= 0.2$ . The shear stress is no longer linear at the high shear rates and the viscosity increases with increasing shear rate, which shows resistance to flow in the suspension as seen in the Figures 4.76 and 4.77.

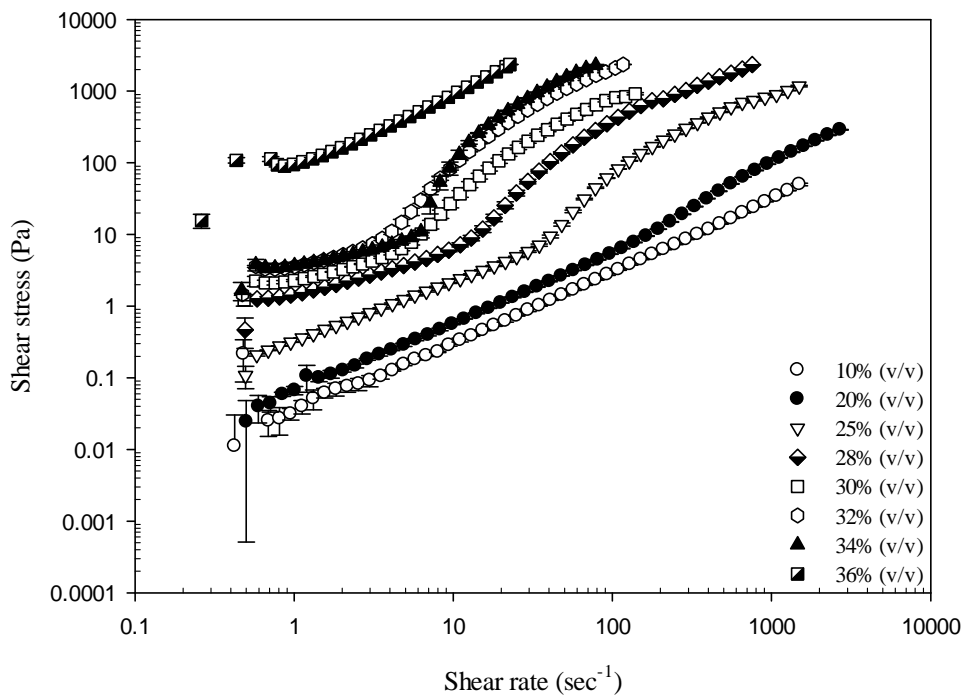


Figure 4.76. Flow curves of the suspensions of CT3 contents in ethylene glycol at different solids.

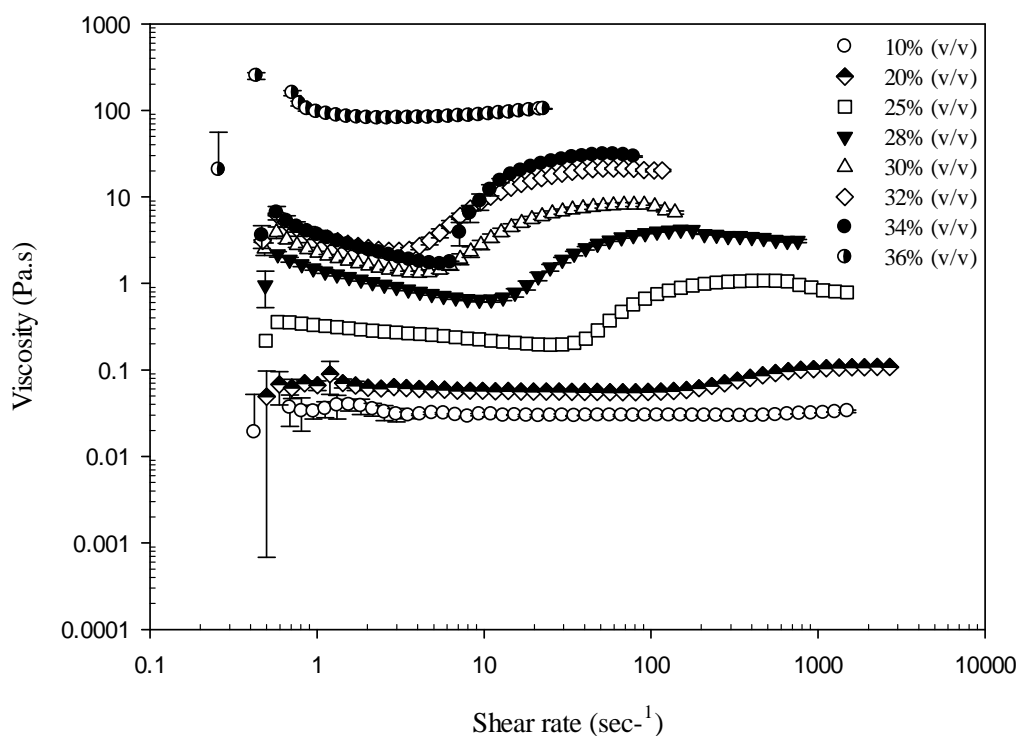


Figure 4.77. Dynamic viscosity curves of the suspensions CT3 in ethylene glycol at different solids contents.

Table 4.10. The zero, critic and maximum values of viscosity, shear rate and shear stress of CT3-ethylene glycol suspensions.

$\Phi$	$\eta_0$	$\sigma_0$	$\gamma_0$	$\eta_c$	$\sigma_c$	$\gamma_c$	$\eta_{max}$	$\sigma_{max}$	$\gamma_{max}$
0.2	0.06	0.0244	0.5936	0.0552	4.4513	80.6200	0.1077	289	2691
0.25	0.35	0.1077	0.5817	0.1950	4.8737	24.9767	1.0777	509	473
0.28	2.17	0.4683	0.5823	0.6470	6.0583	9.3653	4.1787	628	150
0.30	3.91	1.2217	0.5717	1.3193	5.4093	4.1007	8.1583	645	79
0.32	6.27	1.4620	0.5720	2.3723	7.3530	3.0997	21.270	1096	51.5
0.34	6.60	1.6727	0.5730	1.6677	9.0713	5.4397	31.076	1841	59
0.36	251	15.643	0.432	81.350	213.06	2.6190	104.06	2356	22.6

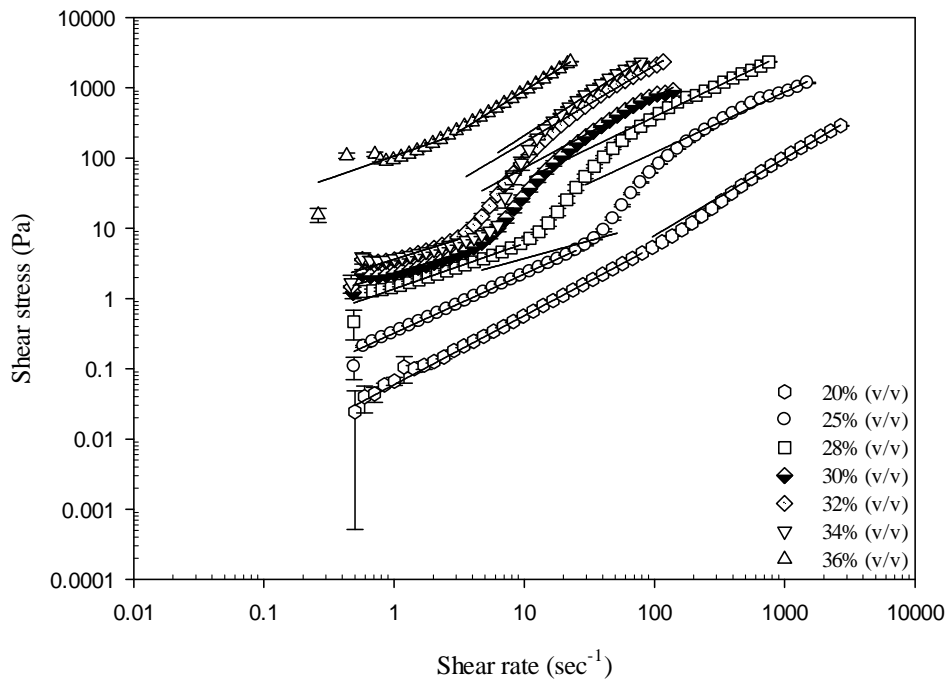


Figure 4.78. Flow curves of the suspensions of CT3 in ethylene glycol (the solid lines represent the power law model).

Table 4.11. The model parameters of Power law model calculated for the suspensions of CT3 in ethylene glycol.

Solids contents	Shear-thinning region			Shear-thickening region		
	$K_I$	$n_I$	$R^2$	$K_{II}$	$n_{II}$	$R^2$
20 vol%	0.0593	0.9831	0.9999	0.0494	1.1012	0.9982
25 vol%	0.3211	0.8416	0.9997	2.2511	0.8620	0.9838
28 vol%	1.3679	0.6466	0.9889	6.2072	0.8971	0.9941
30 vol%	2.2977	0.5617	0.9595	7.1820	1.0037	0.9782
32 vol%	3.6134	0.5745	0.9175	13.6016	1.0914	0.9918
34 vol%	3.6303	0.5036	0.9546	13.2103	1.1991	0.9855
36 vol%	106.6289	0.6415	0.8372	63.0670	1.1585	0.9997

The fit of shear stress versus shear rate data to Power Law was applied on the plot in Figure 4.78. The calculated  $K$ ,  $n$  and  $R^2$  values were listed in Table 4.11. Power law was utilised separately for shear-thinning and shear-thickening regions. The results show the  $n$  values are smaller than 1 for shear-thinning region and some them are bigger than 1 for shear-thickening region at  $\Phi$  values of 0.2, 0.34 and 0.36. The 20 vol% suspension of CT3 shows a Newtonian fluid behaviour because  $n$  values are almost 1 for both shear thinning and shear thickening region.

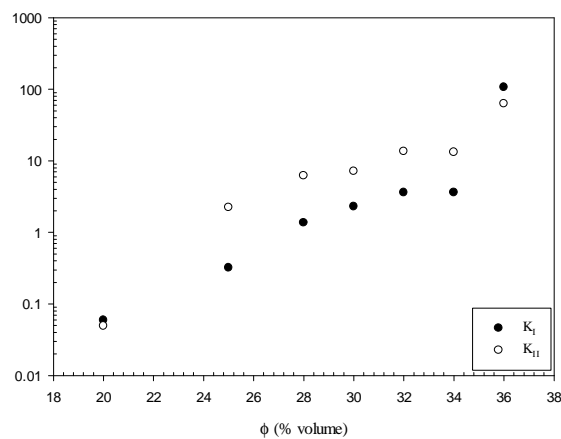


Figure 4.79. Calculated  $K_I$  and  $K_{II}$  values of Power law model for the suspensions of CT3 in ethylene glycol.

The comparison of  $K_I$  and  $K_{II}$  values is displayed in the Figure 4.79. The  $K_I$  and  $K_{II}$  values both increase with increasing  $\Phi$  value,

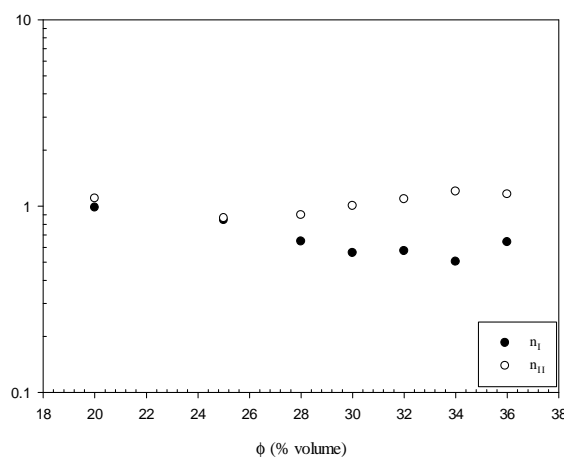


Figure 4.80. Calculated  $n_I$  and  $n_{II}$  values of Power law model for the suspensions of CT3 in ethylene glycol.

The comparison of  $n_I$  and  $n_{II}$  values is displayed in Figure 4.80. The  $n_I$  values are smaller than 1 which proves that this region is shear-thinning. The  $n_{II}$  values are very close to 1. The  $n_{II}$  values are only greater than 1 at  $\Phi=0.32, 0.34$  and  $0.36$ . The  $n_I$  values decrease whereas  $n_{II}$  values slightly increase as the solids contents increase in the suspension.

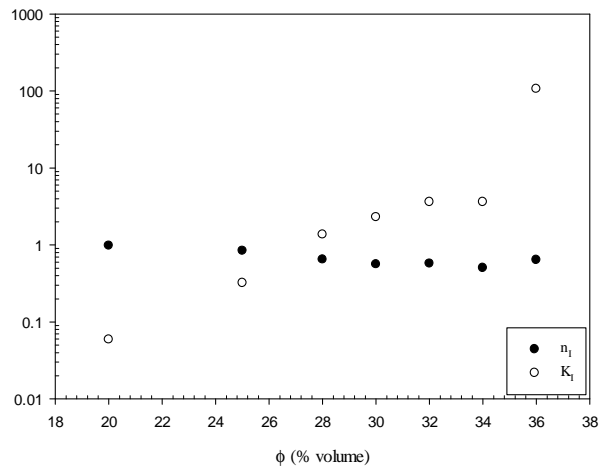


Figure 4.81. Calculated  $n_I$  and  $K_I$  values of Power law model for the suspensions of CT3 in ethylene glycol.

The  $n_I$  values decrease with increasing solids contents while  $K_I$  values increase as seen in Figure 4.81.

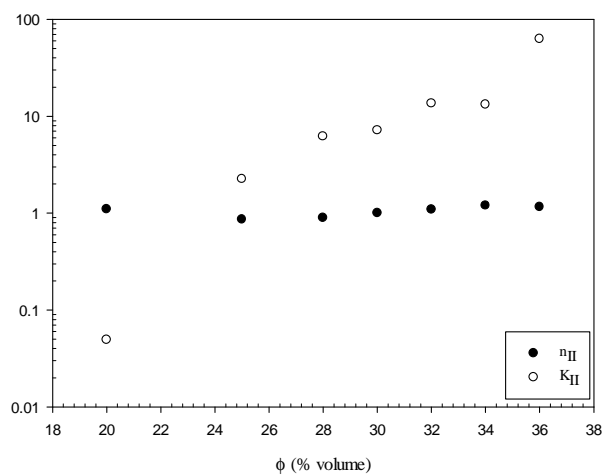


Figure 4.82. Calculated  $n_{II}$  and  $K_{II}$  values of Power law model for the suspensions of CT3 in ethylene glycol.

The  $n_{II}$  values nearly remain constant with increasing solids contents; however,  $K_{II}$  values increase as seen in the Figure 4.82.

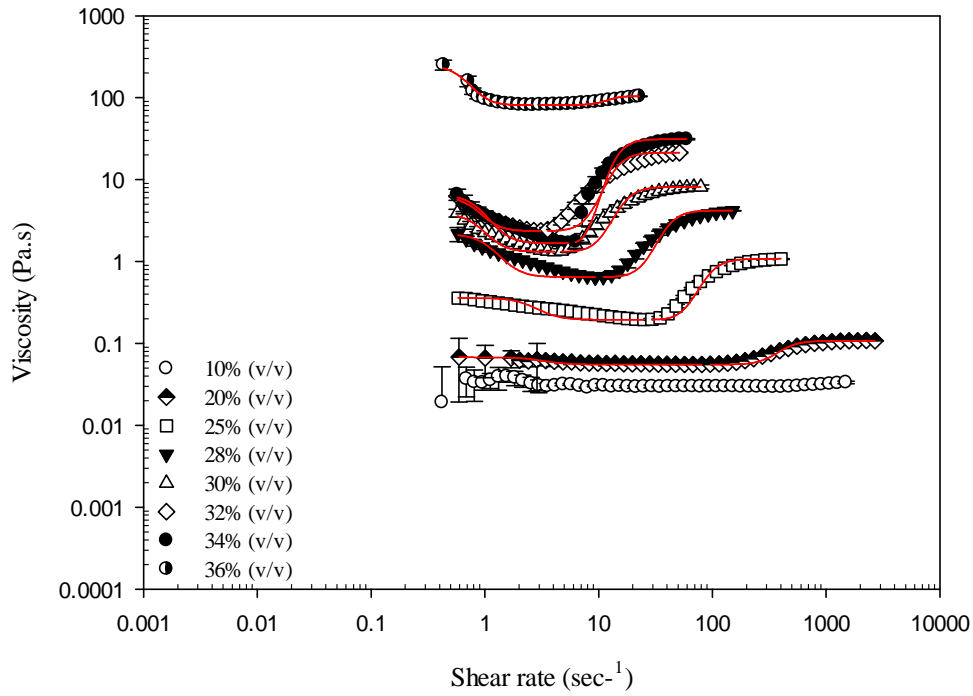


Figure 4.83. Dynamic viscosity curves of the suspensions of CT3 in ethylene glycol at different solids contents (the solid lines represent modified cross model).

Table 4.12. The model parameters of the modified Cross model calculated for the suspensions of CT3 in ethylene glycol

Solids contents	Shear-thinning region			Shear-thickening region		
	$K_I$	$n_I$	$R^2$	$K_{II}$	$n_{II}$	$R^2$
20 vol%	7.4064	2	0.8096	0.0178	2	0.9550
25 vol%	3.1213	2	0.6820	0.0670	2	0.9414
28 vol%	6.1496	2	0.8430	0.1005	2	0.9111
30 vol%	4.0585	2	0.9170	0.3390	2	0.9087
32 vol%	3.3273	2	0.9373	0.2864	2	0.8761
34 vol%	5.2414	2	0.8806	0.4074	2	0.8900
36 vol%	4.5890	2	0.9663	0.0982	2	0.8683

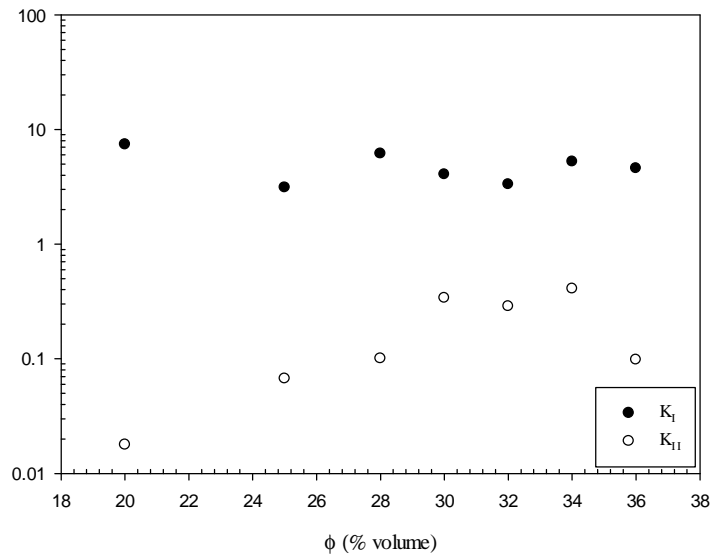


Figure 4.84. Calculated  $K_I$  and  $K_{II}$  values of the modified Cross model for the suspensions of CT3 in ethylene glycol.

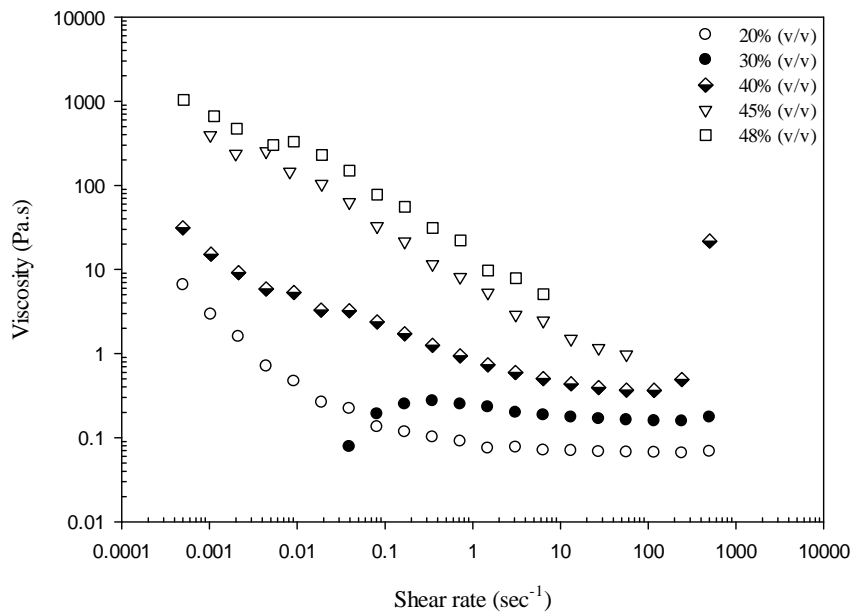


Figure 4.85. Static viscosity curves of the suspensions of CT4 in ethylene glycol at different solids contents.

The fit of viscosity versus shear rate data to the modified Cross Model can be seen on the plot in Figure 4.83 and the calculated  $K$ ,  $n$  and  $R^2$  values for both shear-

thinning and shear-thickening regions were listed in Table 4.12. The curves do seem to fit well to the data in the shear-thinning region. The curves seem to fit well in the shear-thickening region too.

The calculated  $K_I$  and  $K_{II}$  values of the modified Cross model are displayed in the Figure 4.84.  $K_I$  values are greater than  $K_{II}$ . The  $n$  values are constant which is equal to 2 as seen in the Table 4.12.

The static viscosity curves of powder CT4 at different solids contents in ethylene glycol is given in Figure 4.85.

The Table 4.13 gives information about the zero, critic and maximum values of viscosity, shear rate and shear stress of CT4-ethylene glycol suspensions. The values of  $\eta_c$ ,  $\sigma_c$ ,  $\eta_{max}$ , and  $\sigma_{max}$  also increase with increasing  $\Phi$  values whereas the values of  $\gamma_c$  and  $\gamma_{max}$  decrease as seen in the table.

The rheology measurements of CT4 in ethylene glycol with sodium polyacrylate surfactant were done in the range of volume percentages from 20 to 48 vol%. The shear thickening behaviour was seen firstly slightly in the particle volume  $\Phi= 0.3$ . The shear stress is no longer linear at the high shear rates and the viscosity increases with shear rate, which shows resistance to flow in the suspension in the Figure 4.86 and 4.87.

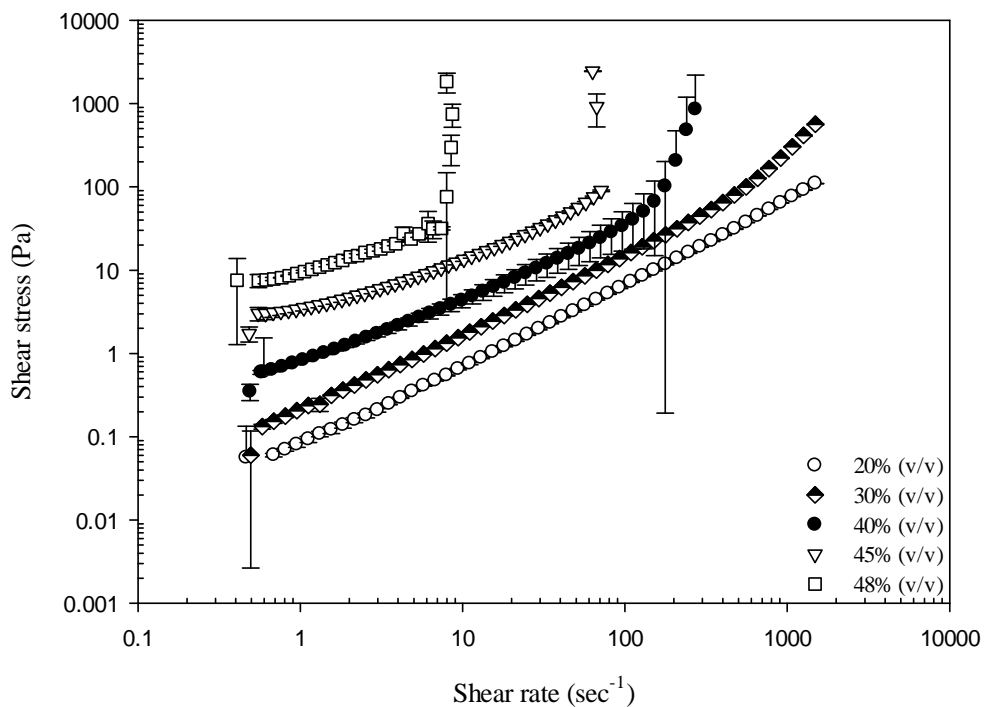


Figure 4.86. Flow curves of the suspensions of CT4 in ethylene glycol at different solids contents.

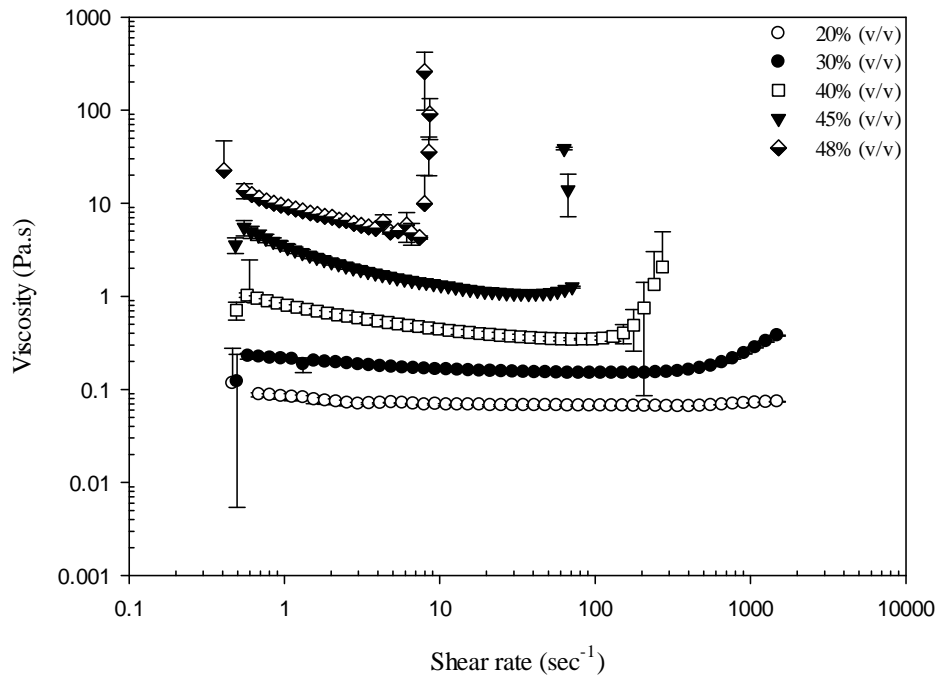


Figure 4.87. Dynamic viscosity curves of the suspensions of CT4 in ethylene glycol at different solids contents.

Table 4.11. The zero, critic and maximum values of viscosity, shear rate and shear stress of CT4-ethylene glycol suspensions.

$\Phi$	$\eta_0$	$\sigma_0$	$\gamma_0$	$\eta_c$	$\sigma_c$	$\gamma_c$	$\eta_{max}$	$\sigma_{max}$	$\gamma_{max}$
0.2	0.11	0.055	0.463	0.065	22.433	341.26	0.0739	109.83	1486.3
0.3	0.12	0.059	0.494	0.149	26.483	177.33	0.3787	563.23	1487.6
0.4	0.71	0.348	0.490	0.346	24.296	70.773	2.0683	850.56	271.73
0.45	3.56	1.727	0.483	1.068	39.776	37.220	38.6767	2444.3	73.5
0.48	22.5	7.528	0.407	4.904	23.586	4.8103	259.7667	1834.6	8.9770

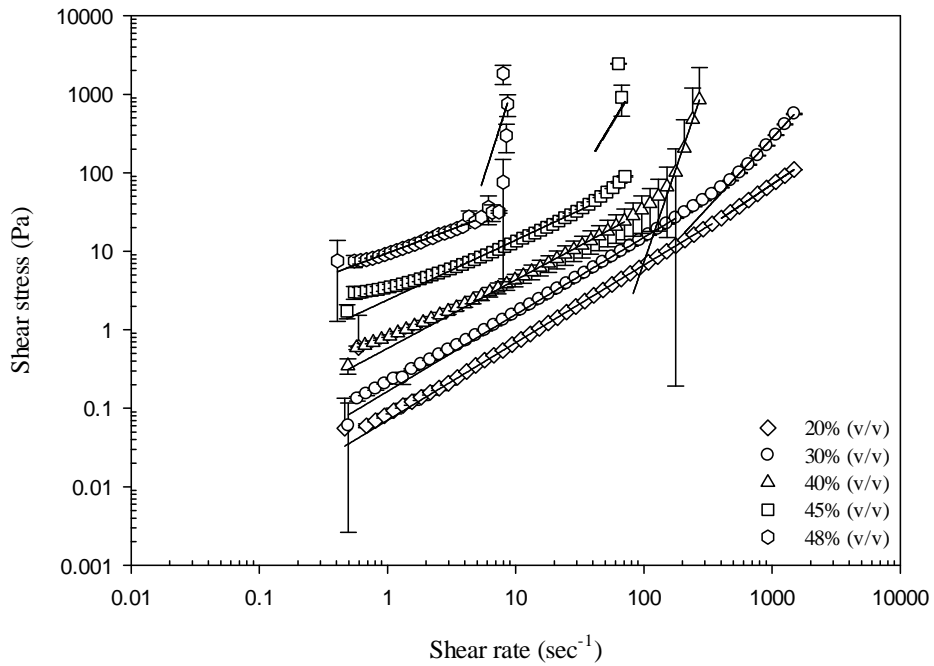


Figure 4.88. Flow curves of the suspensions of CT4 in ethylene glycol at different solids contents (the solid lines represent the power law model).

Table 4.2.12. The model parameters of Power law model calculated for the suspensions of CT4 in ethylene glycol

Solids contents	Shear-thinning region			Shear-thickening region		
	$K_I$	$n_I$	$R^2$	$K_{II}$	$n_{II}$	$R^2$
20 vol%	0.0704	0.9884	0.9998	0.0374	1.0933	1.0000
30 vol%	0.1641	0.9805	0.9999	0.0014	1.7596	0.9962
40 vol%	0.5800	0.8713	0.9988	2.1638E-009	4.7630	0.9943
45 vol%	2.3999	0.7616	0.9931	0.0083	2.6936	0.0983
48 vol%	9.4791	0.6059	0.9568	0.0122	5.1247	0.2114

The fit of shear stress versus shear rate data to Power Law was applied on the plot in Figure 4.88. The calculated  $K$ ,  $n$  and  $R^2$  values were listed in Table 4.14. The Power law was utilised separately for shear-thinning and shear-thickening regions. The

results indicate that the  $n$  values are smaller than 1 for shear-thinning region and bigger than 1 for shear-thickening. The 20 vol% suspension shows a Newtonian fluid behaviour because  $n$  values are almost 1 for both shear thinning and shear thickening region.

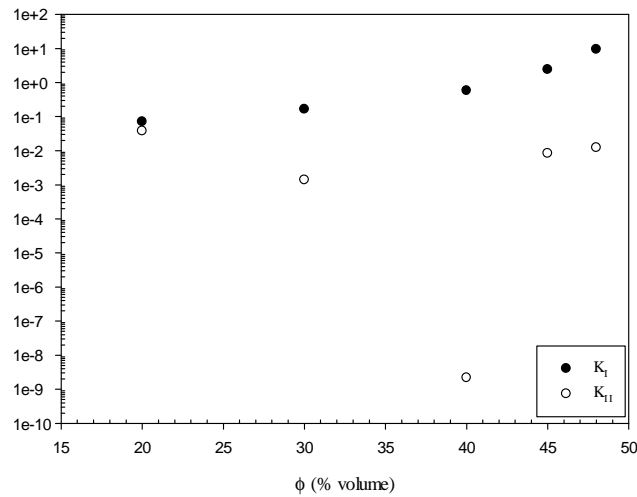


Figure 4.89. Calculated  $K_I$  and  $K_{II}$  values of the Power law for the suspensions of CT4 in ethylene glycol.

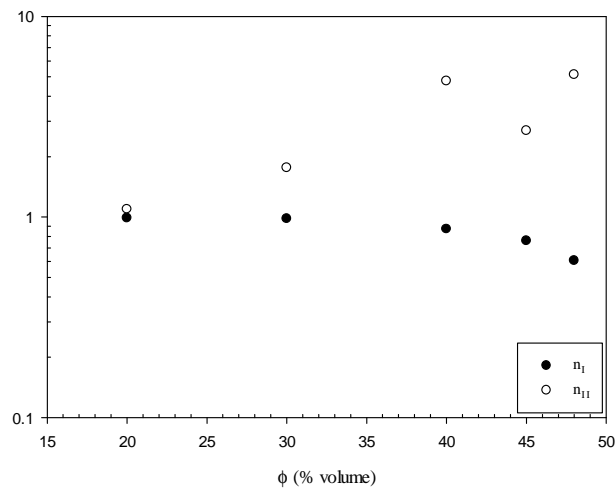


Figure 4.90. Calculated  $n_I$  and  $n_{II}$  values of Power law for the suspension of CT4 in ethylene glycol.

The comparison of  $K_I$  and  $K_{II}$  values is displayed in the Figure 4.89. The  $K_I$  values increase and  $K_{II}$  first seem to decrease then increase with increasing  $\Phi$  values. The comparison of  $n_I$  and  $n_{II}$  values is displayed in Figure 4.90. The  $n_I$  values are

smaller than 1 which proves that this region is shear-thinning. The  $n_{II}$  values are greater than 1 which proves that this region is shear-thickening. The  $n_I$  and  $n_{II}$  values of  $\Phi=0.2$  are almost 1, which shows a Newtonian fluid behaviour. The  $n_I$  values decrease whereas  $n_{II}$  values increase as the solids contents increase in the suspension. The  $n_I$  values decrease and  $K_I$  values increase with increasing solids contents as seen in Figure 4.91. The  $n_{II}$  values nearly remain constant; however,  $K_{II}$  values first decrease then increase as the solids contents increase as seen in Figure 4.92.

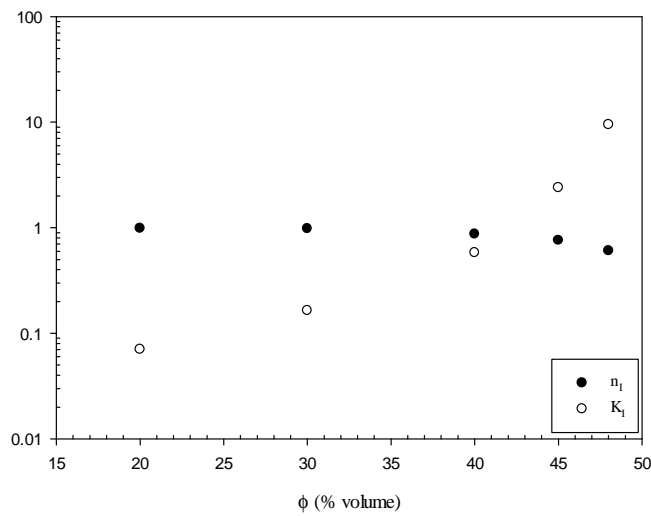


Figure 4.91. Calculated  $n_I$  and  $K_I$  values of Power law for the suspensions of CT4 in ethylene glycol.

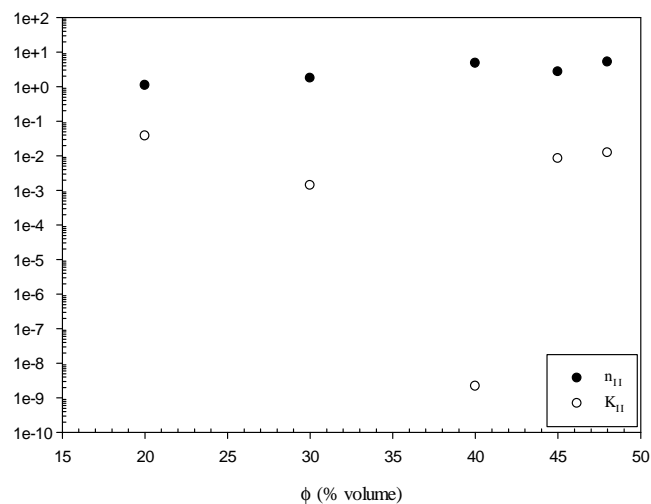


Figure 4.92. Calculated  $n_{II}$  and  $K_{II}$  values of Power law for the suspensions of CT4 in ethylene glycol.

The fit of viscosity versus shear rate data to the modified Cross Model can be seen on the plot in Figure 4.93 and the calculated  $K$ ,  $n$  and  $R^2$  values for both shear-thinning and shear-thickening regions were listed in Table 4.15. The curves seem to fit well in the shear-thickening region but do not fit so good in shear-thinning region due to the zero-shear rate viscosity values.

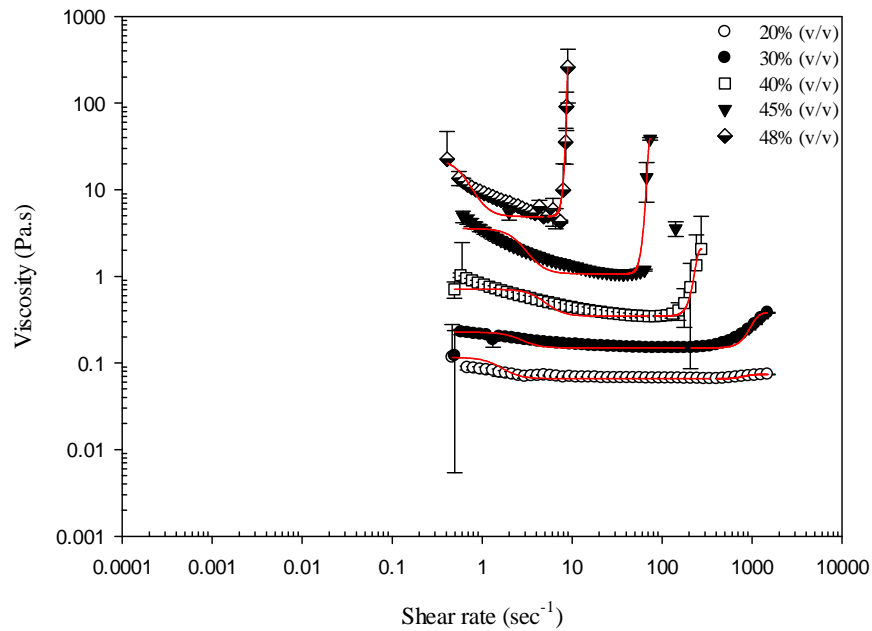


Figure 4.93. Dynamic viscosity curves of the suspensions of CT4 in ethylene glycol (the solid lines represent the modified cross model).

Table 4.15. The model parameters of the modified Cross model calculated for the suspensions of CT4 in ethylene glycol.

Solids contents	Shear-thinning region			Shear-thickening region		
	$K_I$	$n_I$	$R^2$	$K_{II}$	$n_{II}$	$R^2$
20 vol%	141.7730	2	0.0717	0.0019	2	0.8911
30 vol%	25.8582	2	0.2908	0.0007	2	0.9205
40 vol%	3.0638	2	0.7591	0.0010	2	0.9892
45 vol%	4.7766	2	0.6499	0.0020	2	0.9812
48 vol%	10.2418	2	0.7592	0.0071	2	0.9970

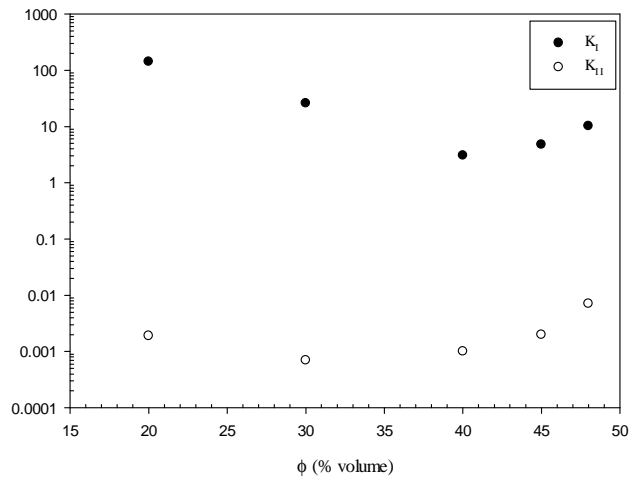


Figure 4.94. Calculated  $K_I$  and  $K_{II}$  values of the modified Cross model for the suspensions of CT4 in ethylene glycol.

The calculated  $K_I$  and  $K_{II}$  values of the modified Cross model are displayed in Figure 4.94.  $K_I$  values are greater value than  $K_{II}$ . The  $n$  values are constant which is equal to 2 as seen in the Table 4.15.

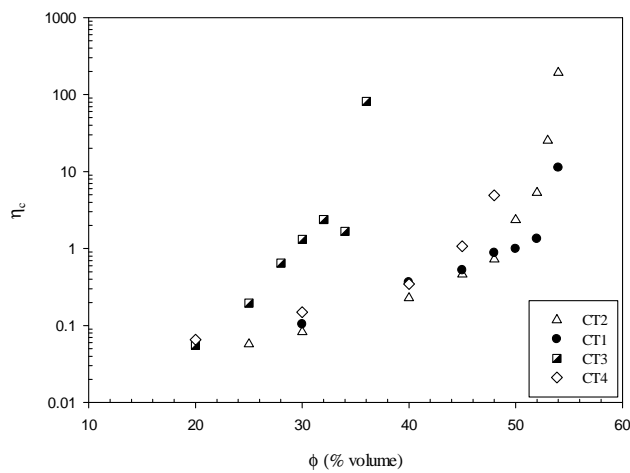


Figure 4.95. Comparison of  $\eta_c$  values of the suspensions of  $TiO_2$  powders at different solids contents.

The comparison of  $\eta_c$ ,  $\gamma_c$ ,  $\sigma_c$ ,  $\eta_{max}$ , and  $\sigma_{max}$  values of the suspensions of CT1, CT2, CT3 and CT4 at different  $\Phi$  values is given between Figures 4.95 and 4.100. The  $\eta_c$  values increase as the value  $\Phi$  increases. CT3 has the greatest value of  $\eta_c$  and  $\eta_c$

values of the other powders are smaller at  $\Phi=0.3$  according to Figure 4.95. CT4 and CT1 almost have the same critical viscosity value and value of CT2 is a bit smaller than those at  $\Phi=0.4$ . The  $\eta_c$  values of CT4 become greater than CT1 and CT2 when  $\Phi$  becomes 0.45 and 0.48. The  $\eta_c$  values are close to each other up to  $\Phi=48$ . The  $\eta_c$  values of CT2 become greater after this  $\Phi$  value. CT3 and CT4 have greater  $\eta_c$  values at some  $\Phi$  values. This could be due to the polydispersity of these powders. The decrease of  $\gamma_c$  values of the  $\text{TiO}_2$  powders with the increase in solids contents is given in Figure 4.96.

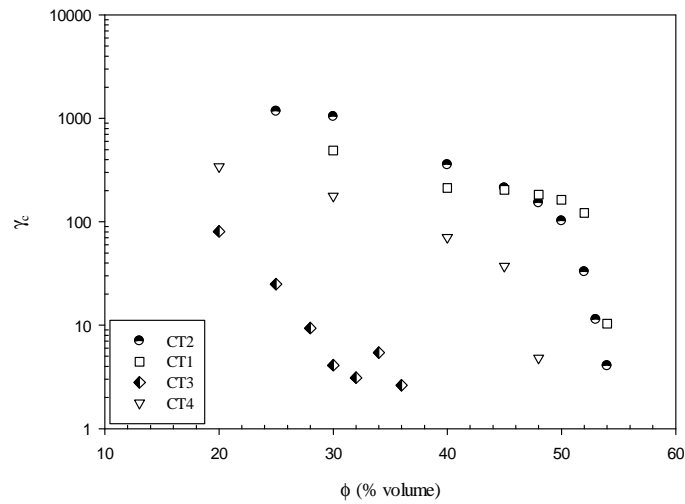


Figure 4.96. Comparison of  $\gamma_c$  values of the suspensions of the suspensions of  $\text{TiO}_2$  powders at different solid contents.

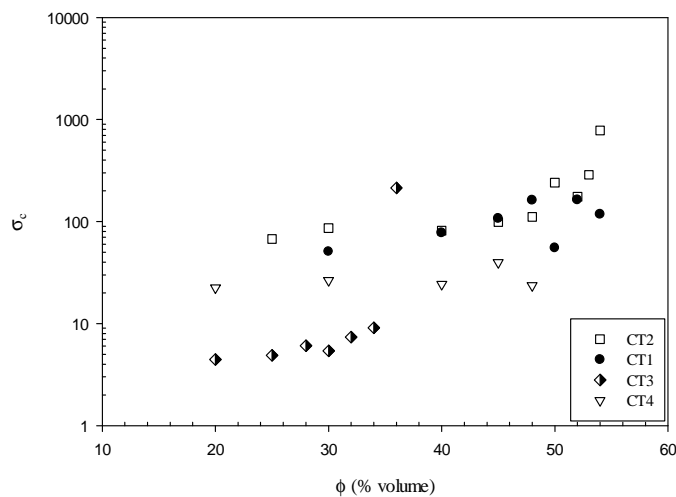


Figure 4.97. Comparison of  $\sigma_c$  values of the suspensions of  $\text{TiO}_2$  powders at different solids contents.

The change of  $\sigma_c$  values of the  $\text{TiO}_2$  powders with the increase in solids contents is seen in Figure 4.97. CT2 reaches the highest  $\sigma_c$  value among the powders. The CT2 has the greatest  $\eta_{\text{max}}$  value compared to CT1 at high solids contents according to Figure 4.98. CT3 has the greatest value at low solids contents such as  $\Phi=0.3$ .  $\sigma_{\text{max}}$  values increase with increasing solids content according to Figure 4.100. CT1 and CT2 reach the highest  $\sigma_{\text{max}}$  at high solid loadings.

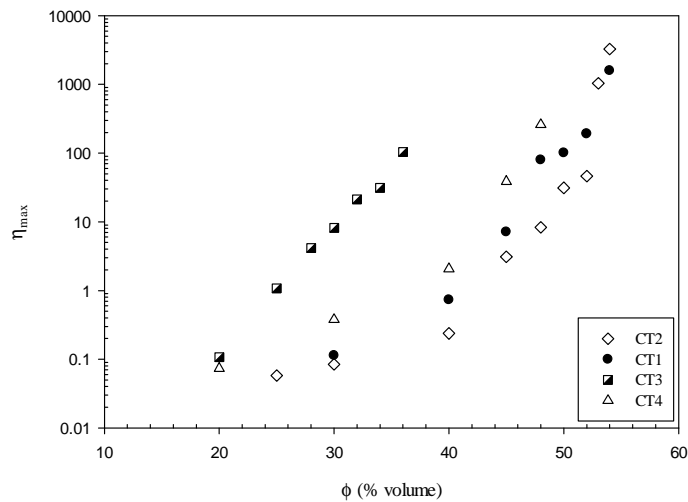


Figure 4.98. Comparison of  $\eta_{\text{max}}$  values of the suspensions of  $\text{TiO}_2$  powders at different solids contents.

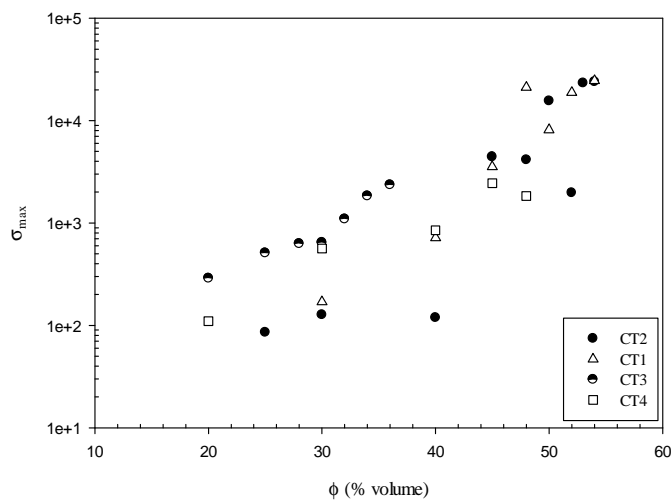


Figure 4.100. Comparison of  $\sigma_{\text{max}}$  values of the suspensions of  $\text{TiO}_2$  powders at different solids contents.

### **4.3. Synthesis, Characterization and Rheological Behaviour of SiO<sub>2</sub>**

#### **4.3.1. Characterization of synthesized SiO<sub>2</sub> particles**

The size of the silica spheres was controlled by changing the NH<sub>3</sub> to alkoxide molar ratio in the range of 4.4 to 1.1 and water to alkoxide molar ratio of 17-14. The reactions were conducted at total TEOS molarities of 0.28.

The SEM micrographs of SS1 are shown in Figure 4.101. The synthesized silica particles are in spherical shape. Figure 4.102 displays a very sharp particle size distribution for SS1 which proves the monodispersity of the synthesized silica spheres. The average particle size by volume is 483 nm. The NH<sub>3</sub> to alkoxide and water to alkoxide molar ratios were 4.39 and 16.89 which were the highest amounts used in silica preparation in this work.

The size of the silica spheres is also increased when the initial NH<sub>3</sub> molar ratio is increased, (Harris et al., 1997; Bogush, 1988). The diameter of monodispersed silica spheres is mainly affected by the relative contribution of nucleation and growth processes. Hydrolysis and condensation reactions provide precursor species and the necessary supersaturation for the formation of particles. The increase in ammonia concentration leads to an increase in both hydrolysis and condensation reactions. Intermediate concentration will be increased rapidly due to high hydrolysis rate while the consumption rate also fast through the condensation reaction after reaching the supersaturation and this might shorten the nucleation period that causes the decrease in the total number of nuclei formed and the final sphere size will be relatively larger.

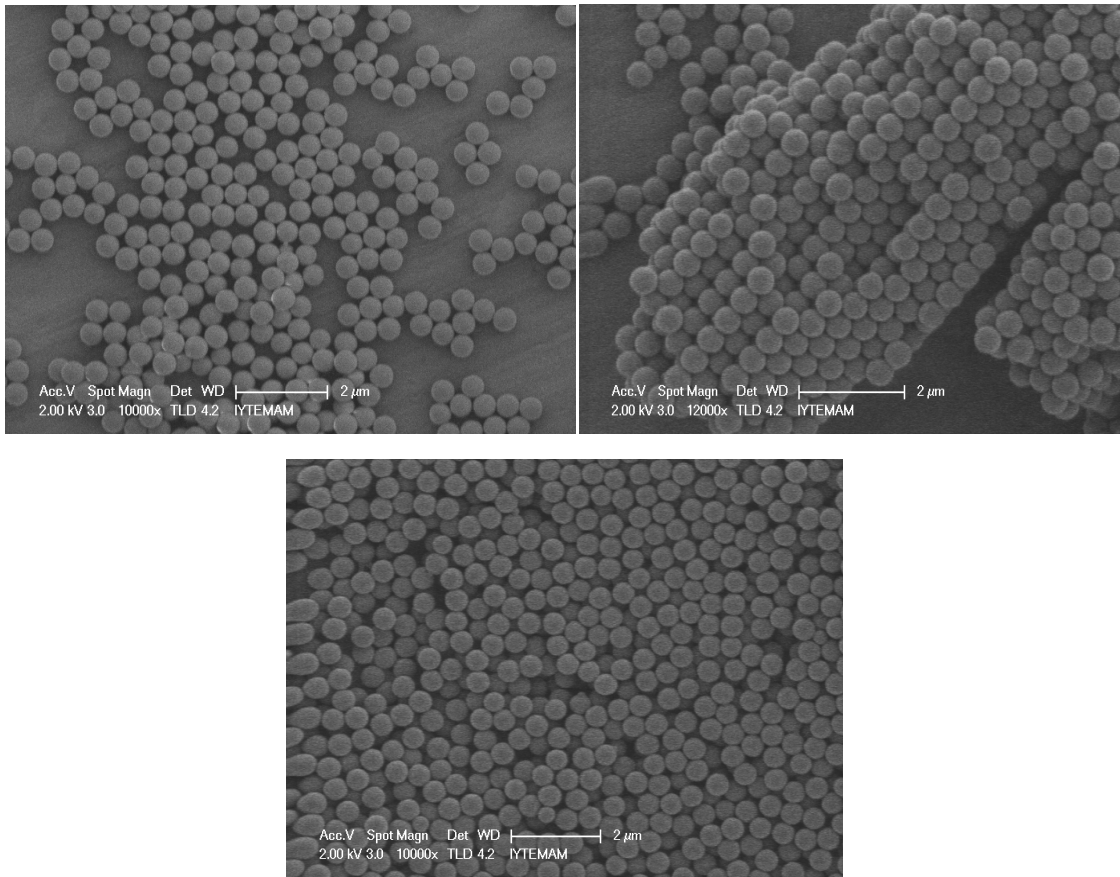


Figure 4.101. The SEM micrographs of SS1.

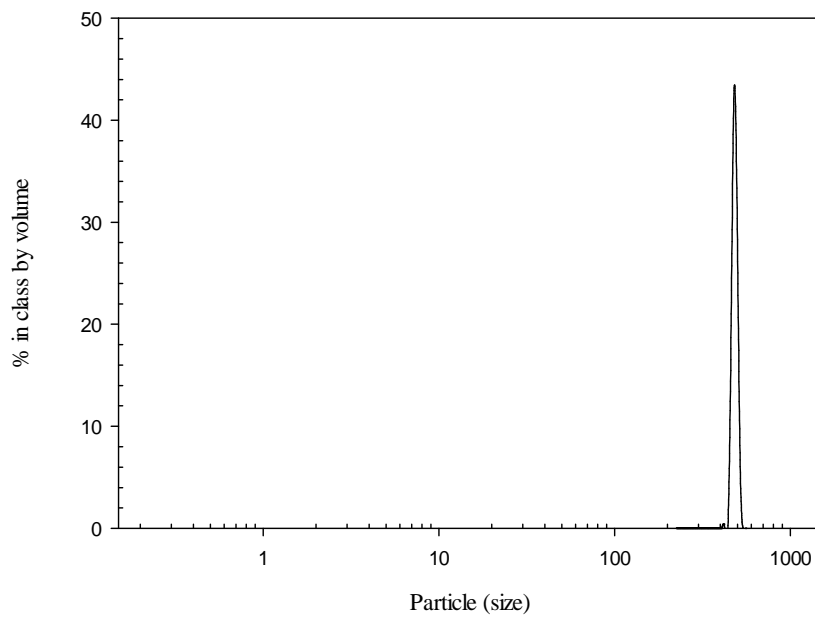


Figure 4.102. Particle Size Distribution of SS1.

The particle size of the spheres was reduced to 201 nm when the  $\text{NH}_3$  alkoxide ratio was cut to 2.189 as seen in Figure 4.104. The peak is not as sharp as in Figure 4.102 which shows the particle size distribution of SS1.

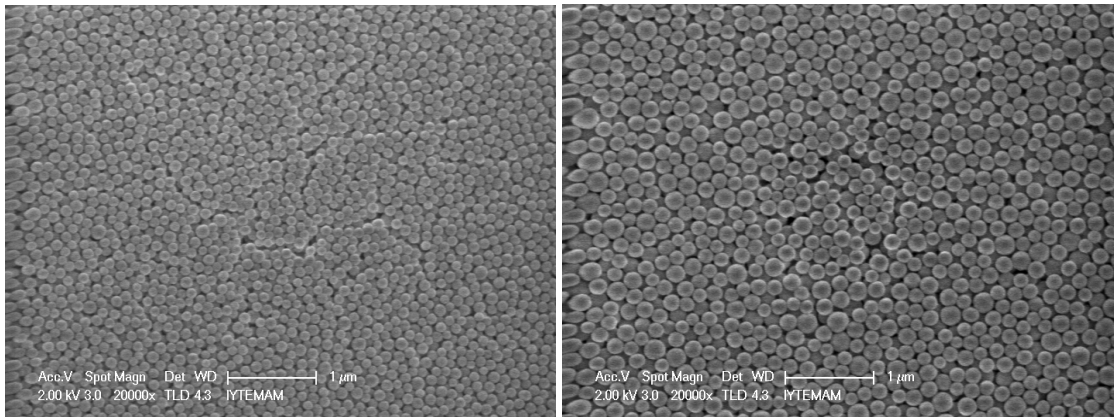


Figure 4.103. The SEM micrographs of SS2.

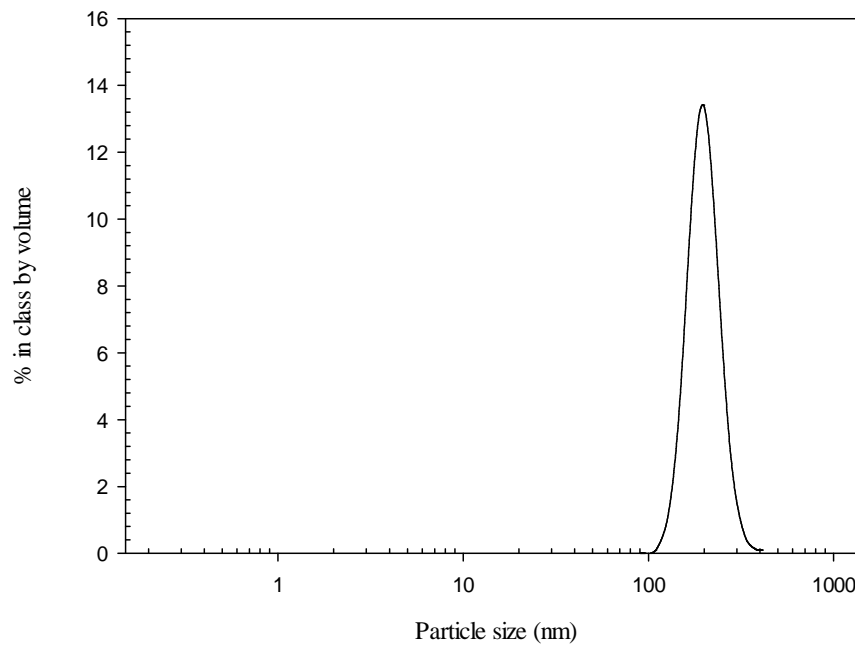


Figure 4.104. Particle Size Distribution of SS2.

In the synthesis of SS3, the  $\text{NH}_3$  to alkoxide was kept constant at 4.39 while water to alkoxide molar ratio was decreased from 16.89 to 14.27 and alcohol ratio was increased from 51.52 to 54.82 when it is compared with SS1.

The SEM micrographs of SS3 are seen in Figure 4.105. The average particle size by volume is 297 nm in Figure 4.106. However, it is obvious on the SEM micrographs

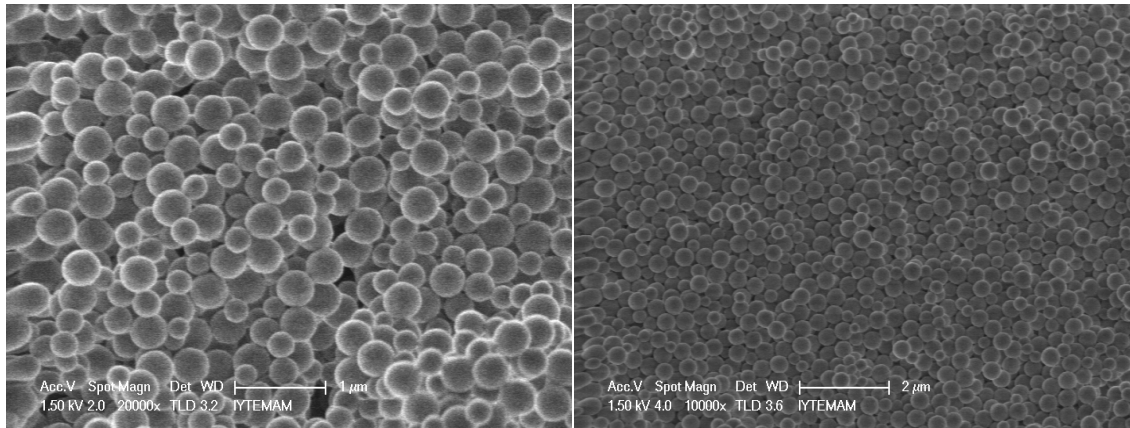


Figure 4.105. The SEM micrographs of SS3.

that synthesized SS3 powder is polydispersed. The particles exist in the size of 250 and 400 nm also as seen in Figure 4.105.

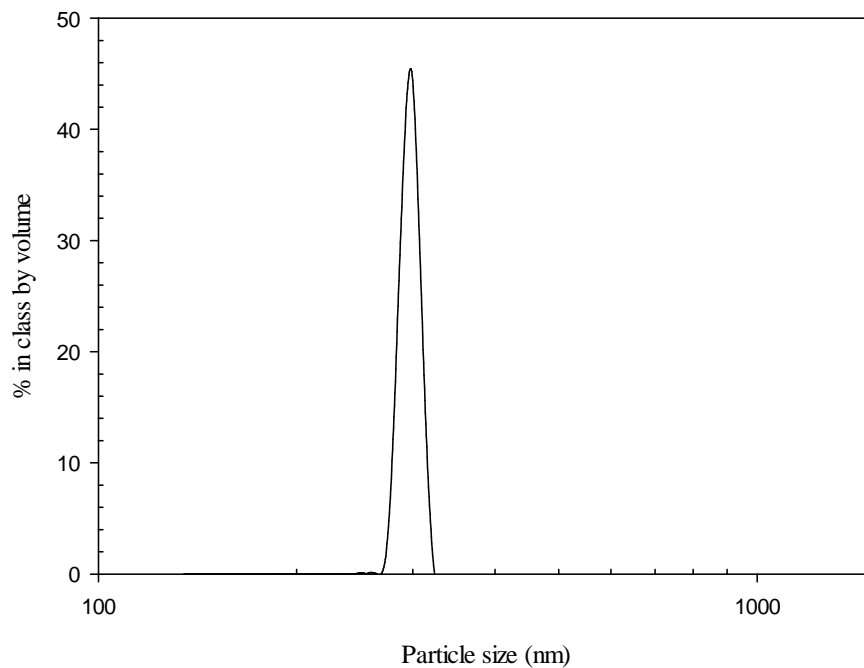


Figure 4.106. Particle Size Distribution of SS3.

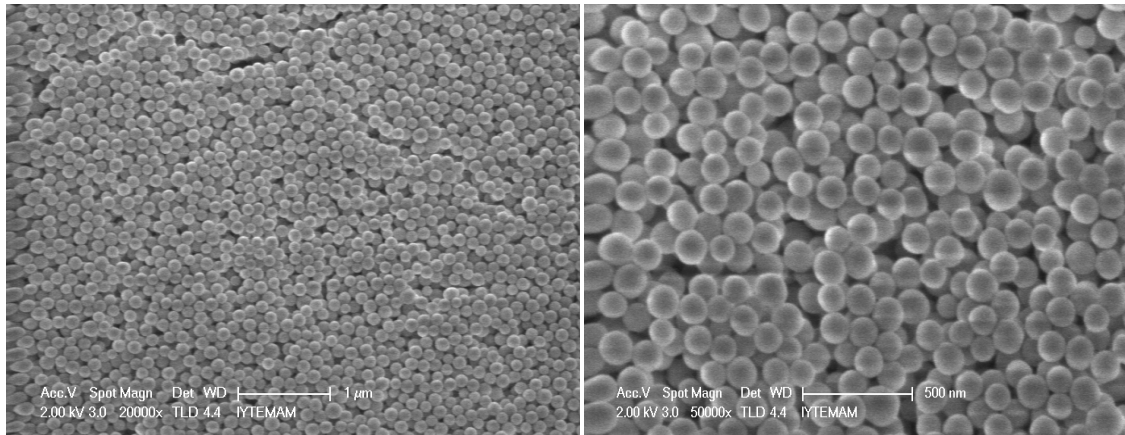


Figure 4.107. The SEM micrographs of SS4.

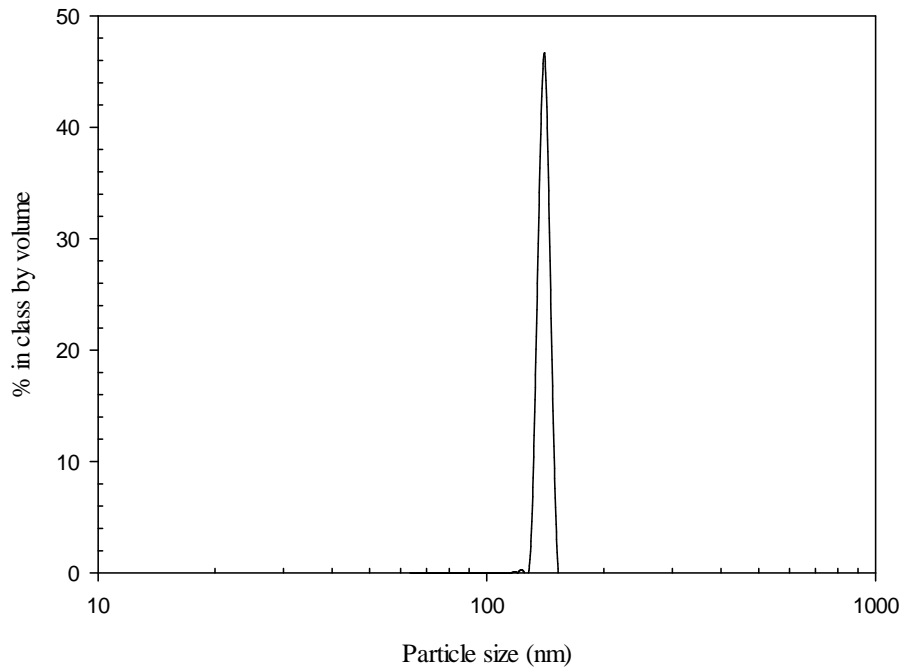


Figure 4.108. Particle Size Distribution of SS4.

The volume of the batches was reduced from 500 to 100 ml in SS4 and SS5. The  $\text{NH}_3$  to alkoxide ratio was cut to 1.1 in SS4 when it is compared with SS2. The particle size was reduced to 140 from 201 nm which can be seen in Figure 4.108. The SEM micrographs of SS4 were also given in Figure 4.107.

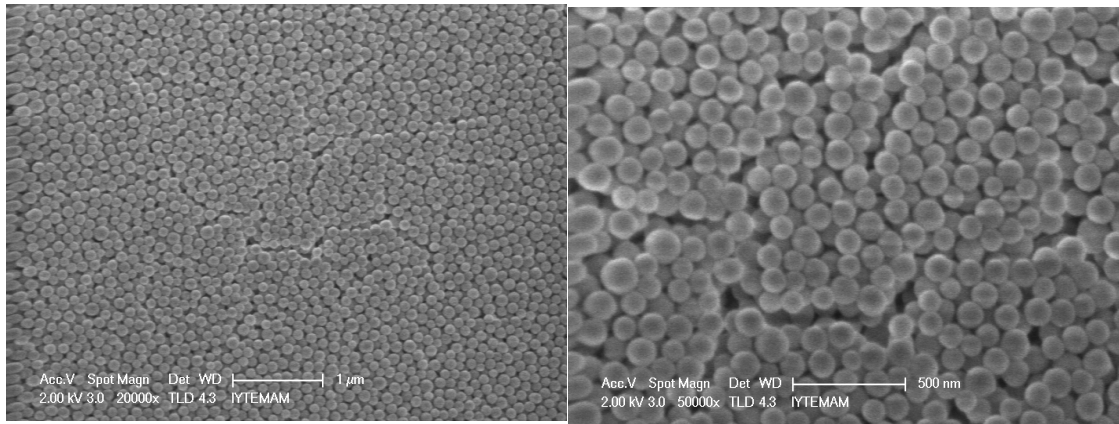


Figure 4.109. The SEM micrographs of SS5.

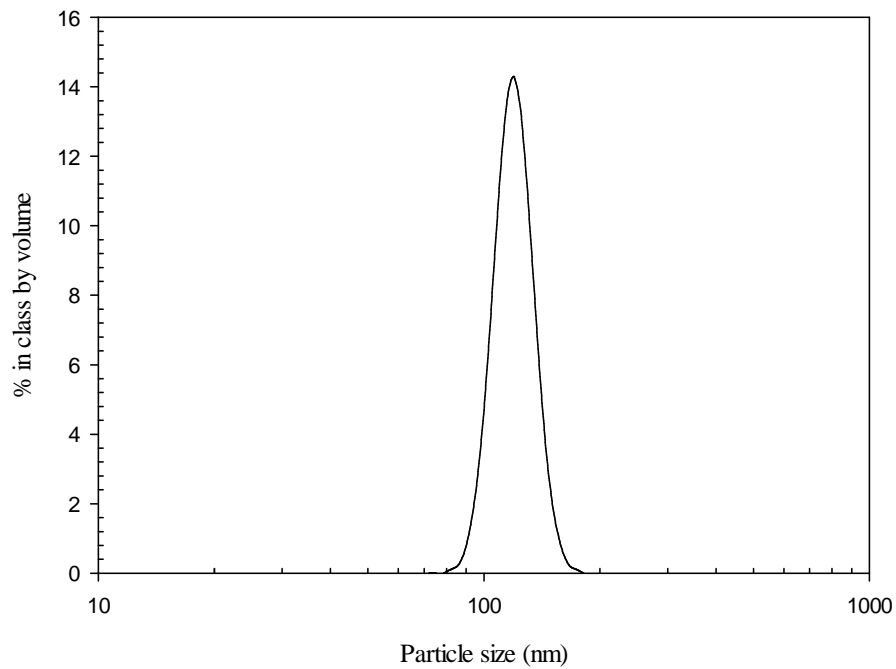


Figure 4.110. Particle Size Distribution of SS5.

In preparation of SS5, the  $\text{NH}_3$  to alkoxide was same as SS4, but the alcohol ratio was decreased from 57.11 to 50.89. As a result of this, the particle size was decreased slightly from 140 to 120 nm as seen in Figure 4.110. The SEM micrographs of SS5 are given in Figure 4.109.

The particle size distributions of all of the synthesized silica particles are given in Figure 4.111. The reduction in initial ammonia ratio makes the particle size of the spheres smaller.

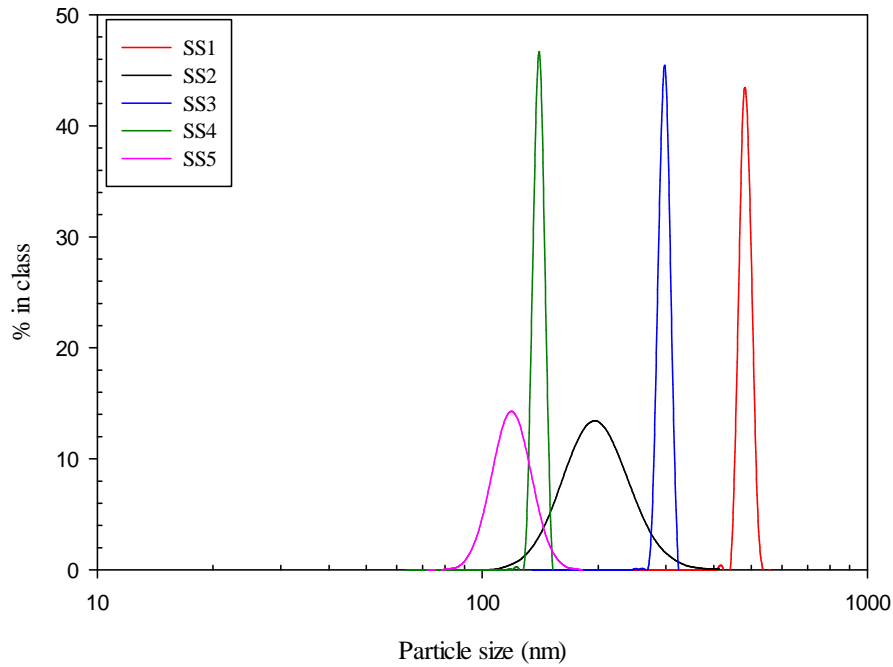


Figure 4.111. Comparison of the Particle Size Distributions of the synthesized silica particles.

### 4.3.2. Rheology of Synthesized SiO<sub>2</sub> Spheres

The synthesized silica particles (SS3) were dispersed in ethylene glycol for the investigation of the rheological behaviour. In order to obtain maximum volume fraction  $\Phi_m$  for SS3, the relative viscosities were drawn at different solid loadings as seen in Figure 4.112. Afterwards, the experimental points were fitted to the modified Krieger-Dougherty equation and the  $\Phi_m$  and  $n$  values were found as 0.47 and 0.5 with  $R^2$  of 1.

Table 4.16. The model parameters of the modified Krieger-Dougherty model calculated for the suspension of SS3.

	$\Phi_m$	$n$	$R^2$
SS3	0.47	0.5011	1.0000

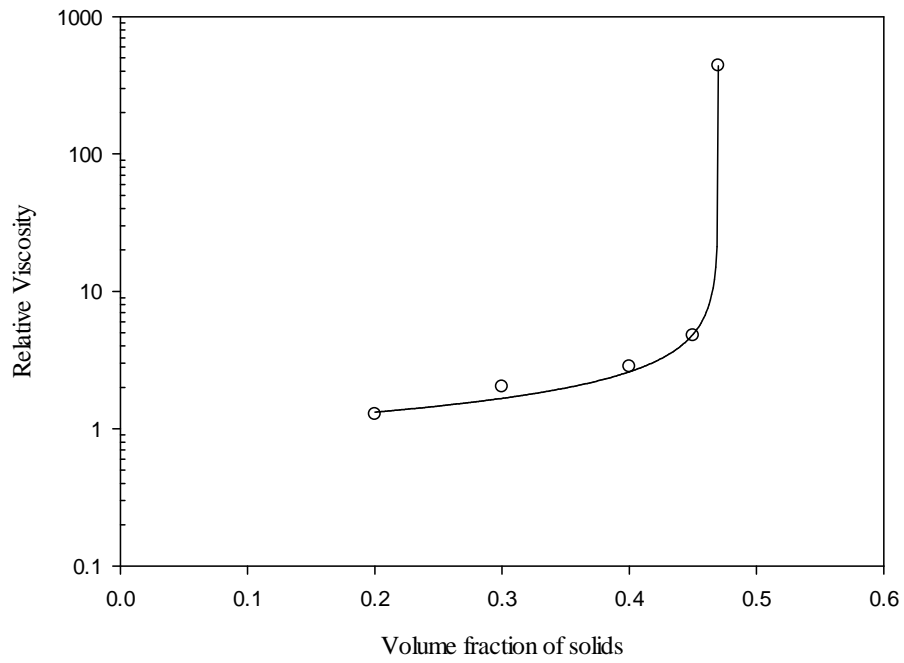


Figure 4.112. Relative high shear viscosity as a function of volume fraction of solids for the suspensions of SS3 in ethylene glycol.

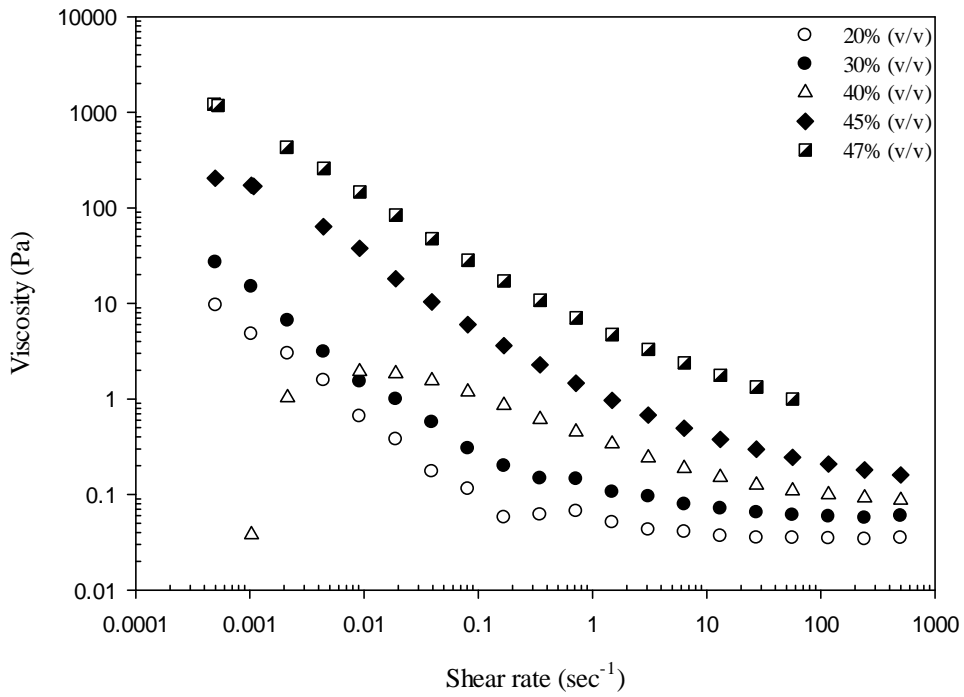


Figure 4.113. Static Viscosity curves of the suspensions of SS3 in ethylene glycol at different solids contents.

The static and dynamic viscosity curves of SS3 at different solids contents in ethylene glycol are given in Figures 4.113 and 4.114. The solids contents of silica spheres changed from 20 to 47 vol% without any surfactant. The viscosity of the suspension decreased for the  $\Phi$  values between 0.2 and 0.45 with increasing shear rate. The shear thickening behaviour was seen firstly in the particle volume  $\Phi= 0.47$ . However, only one data could be taken due to the torque overload. The flow curves are given in Figure 4.115. The Power law and modified-Cross model were applied to the experimental data only for shear-thinning regions because there is only on data at shear thickening part of 47 vol%.

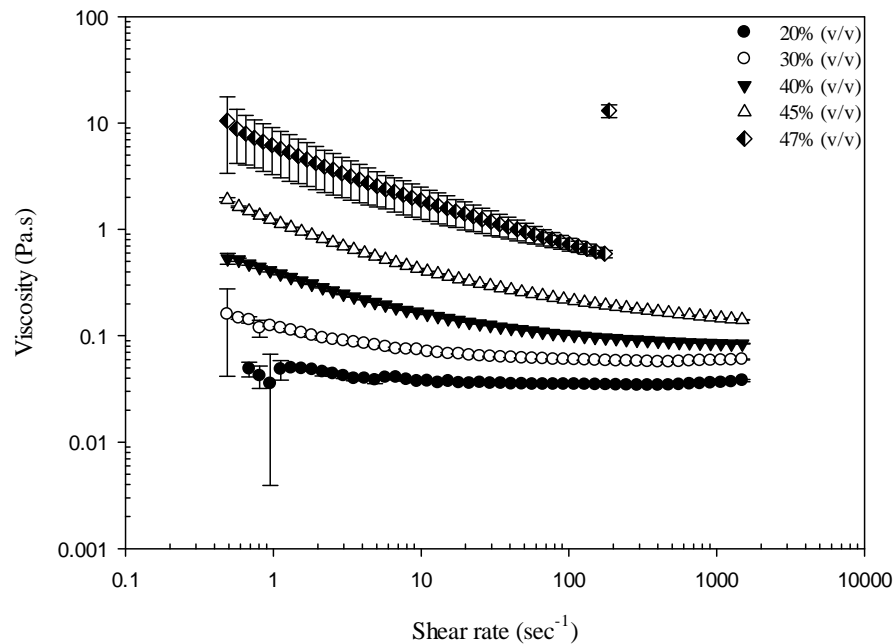


Figure 4.114. Dynamic viscosity curves of the suspensions of SS3 in ethylene glycol at different solids contents.

The fit of shear stress versus shear rate data to Power Law was applied on the plot in Figure 4.116. The calculated  $K$ ,  $n$  and  $R^2$  values were listed in Table 4.17. The  $n$  values are 1 at  $\Phi=0.2$  and 0.3, which indicates that they are Newtonian fluids. The suspensions of SS3 whose  $\Phi$  values are 0.4, 0.45 and 0.47 display shear-thinning behaviour, as the  $n$  values are smaller than 1.

The fit of viscosity versus shear rate to the modified Cross Model can be seen on the plot in Figure 4.117 and the calculated  $K$ ,  $n$  and  $R^2$  values for shear-thickening

region of 47 vol% were given in Table 4.17. In the shear-thinning region, the curve does not seem to fit well to the data and the  $R^2$  value is 0.6878.

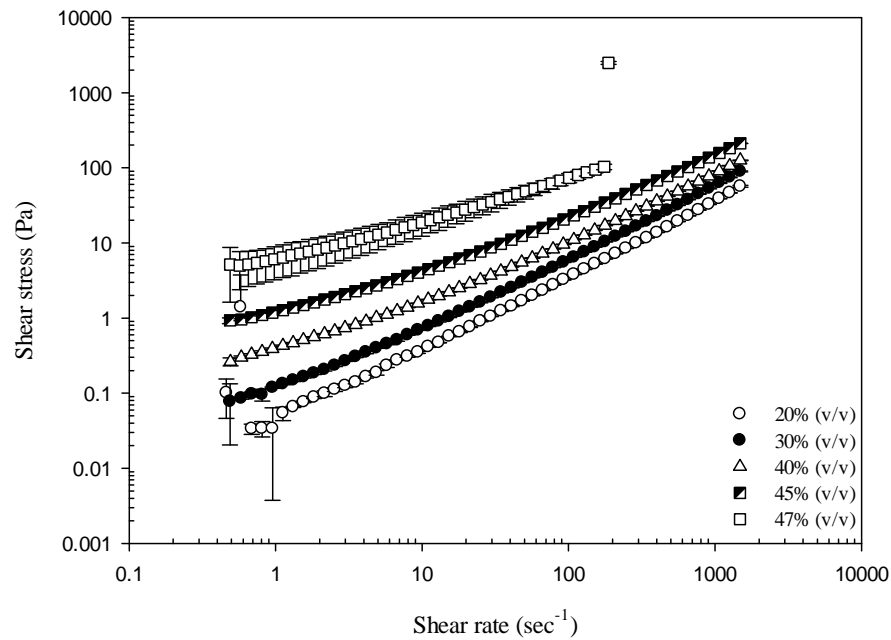


Figure 4.115. Flow curves of the suspensions of SS3 in ethylene glycol at different solids contents.

Table 4.17. The model parameters of Power law model calculated for the suspensions of SS3.

$\Phi$ (% volume)	n value for shear-thinning region	K value for shear-thinning region	$R^2$
0.2	1.0603	0.0241	0.9994
0.3	1.0243	0.0499	0.9998
0.4	0.9412	0.1282	0.9997
0.45	0.8490	0.4212	0.9996
0.47	0.5889	4.8570	0.9990

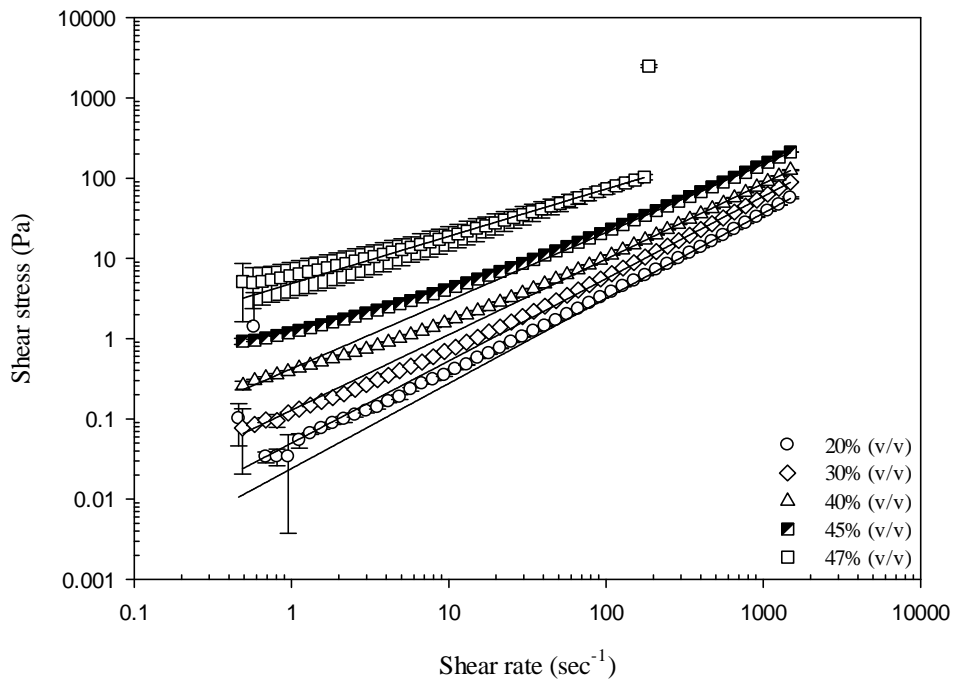


Figure 4.116. Flow curves of the suspensions of SS3 in ethylene glycol (the solid lines represent power law model).

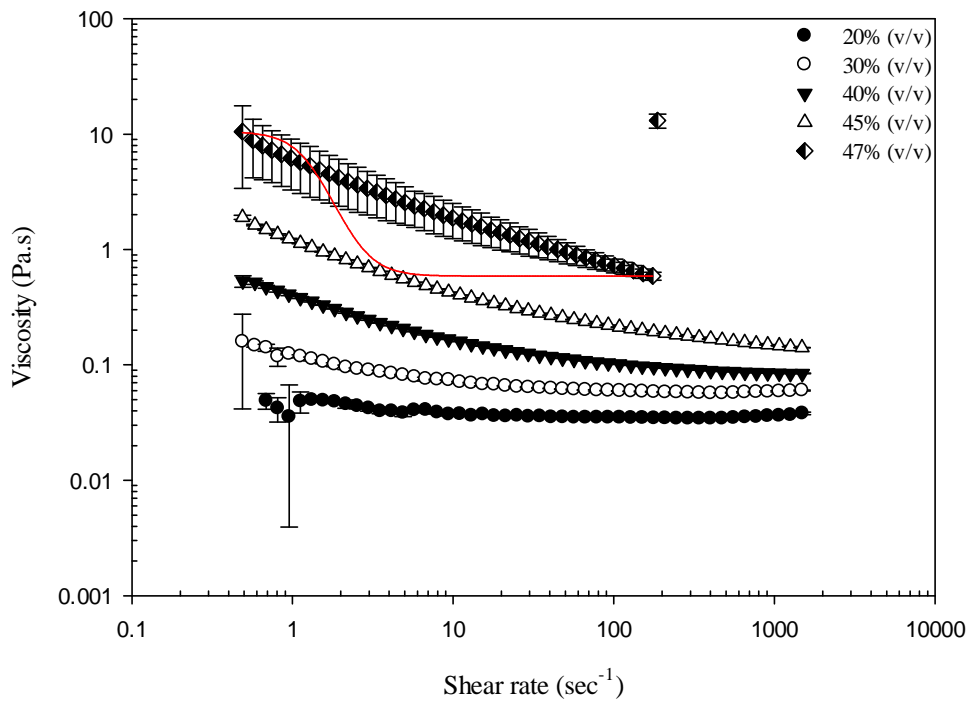


Figure 4.117. Dynamic viscosity curves of the suspensions of SS3 in ethylene glycol at different solids contents (the solid line represents the modified Krieger-Dougherty model).

Table 4.18. The model parameters of the modified Cross model calculated for the 47 vol% suspension of SS3 in ethylene glycol

Solids contents	$K_1$	$n_1$	$R^2$
47% (v/v)	108.2503	2	0.6878

The dynamic shear rheology of the silica dispersions was investigated by stress and frequency sweep tests. The stress sweep tests were used for determination of the linear viscoelastic region of the dispersion. Then, a stress value was picked in the linear viscoelastic region and used in frequency sweep test as seen between the Figures 4.118 and 4.127. The dynamic shear rheology measurements showed that the solid part of the suspensions became dominant over the liquid part for silica as the solid contents is increased from 20 to 47.

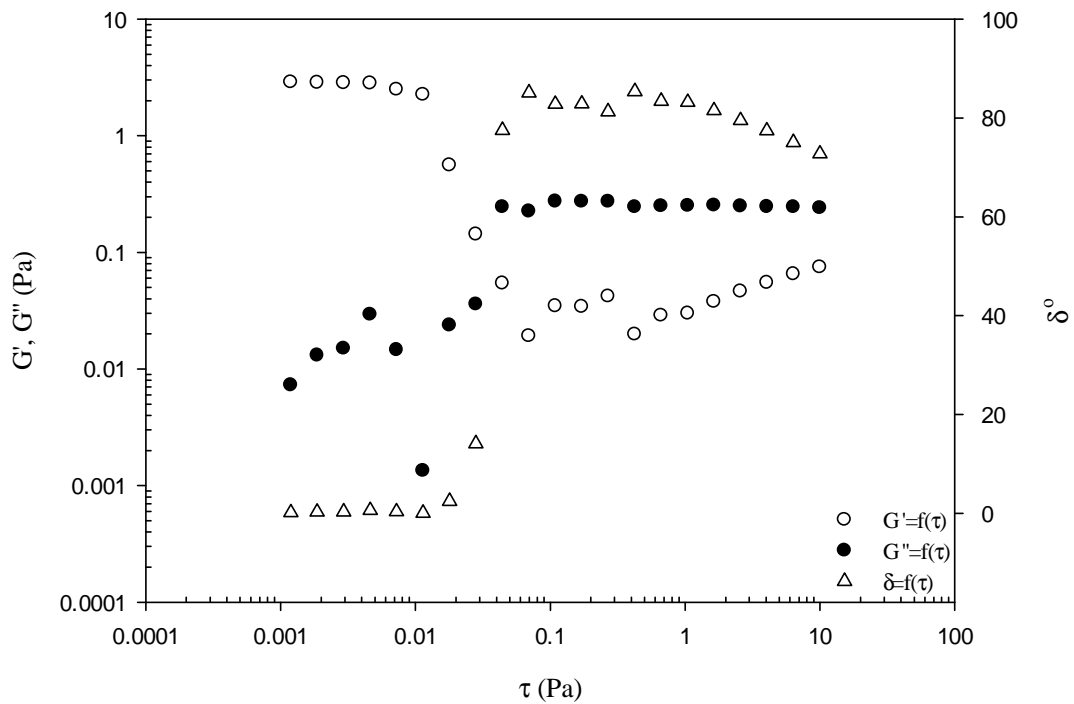


Figure 4.118. Amp- sweep tests of 20 vol% suspension of SS3 in ethylene glycol.

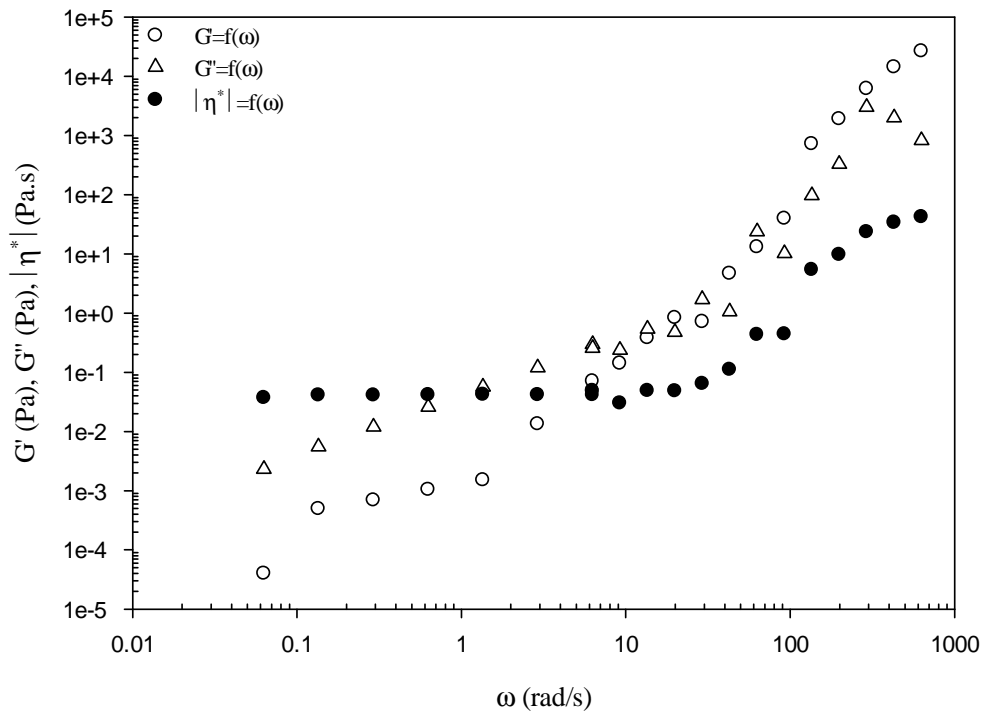


Figure 4.119. Freq-sweep graph of 20 vol% suspension of SS3 in ethylene glycol.

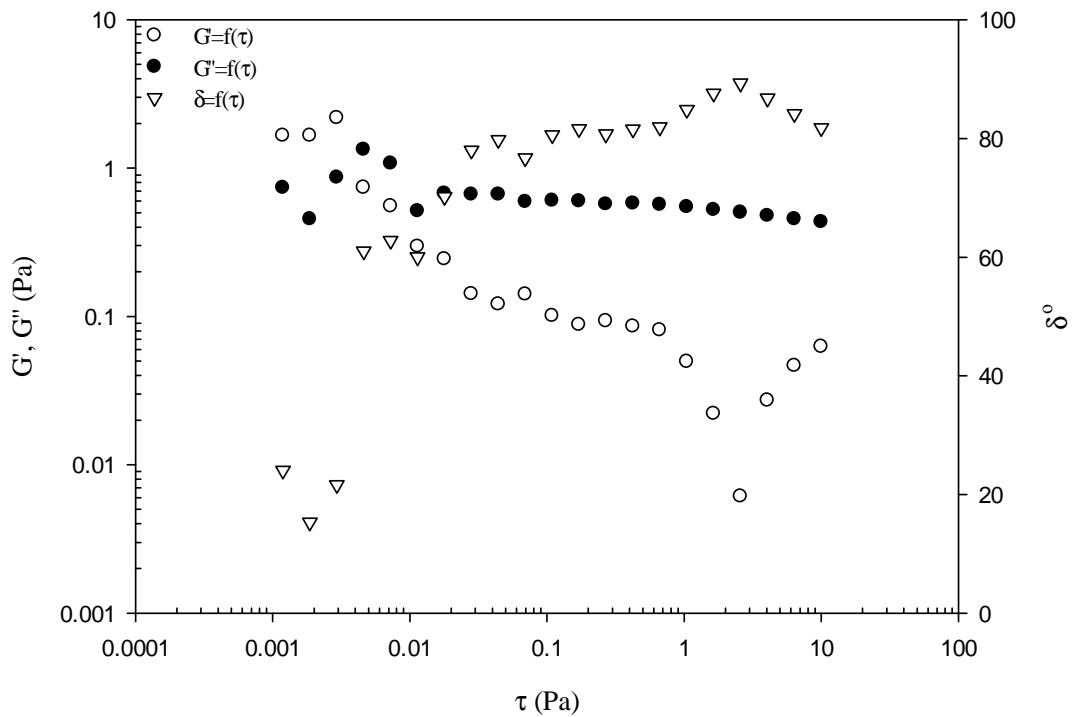


Figure 4.120. Amp-sweep graph of 30 vol% suspension of SS3 in ethylene glycol.

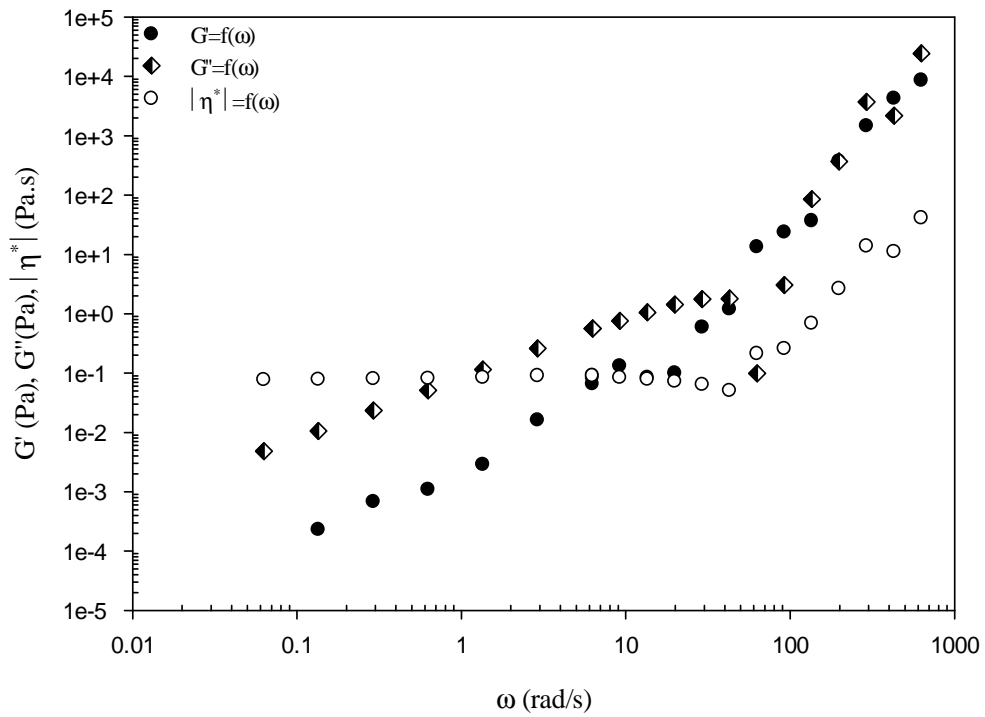


Figure 4.121. Freq-sweep graph of 30 vol% suspension of SS3 in ethylene glycol.

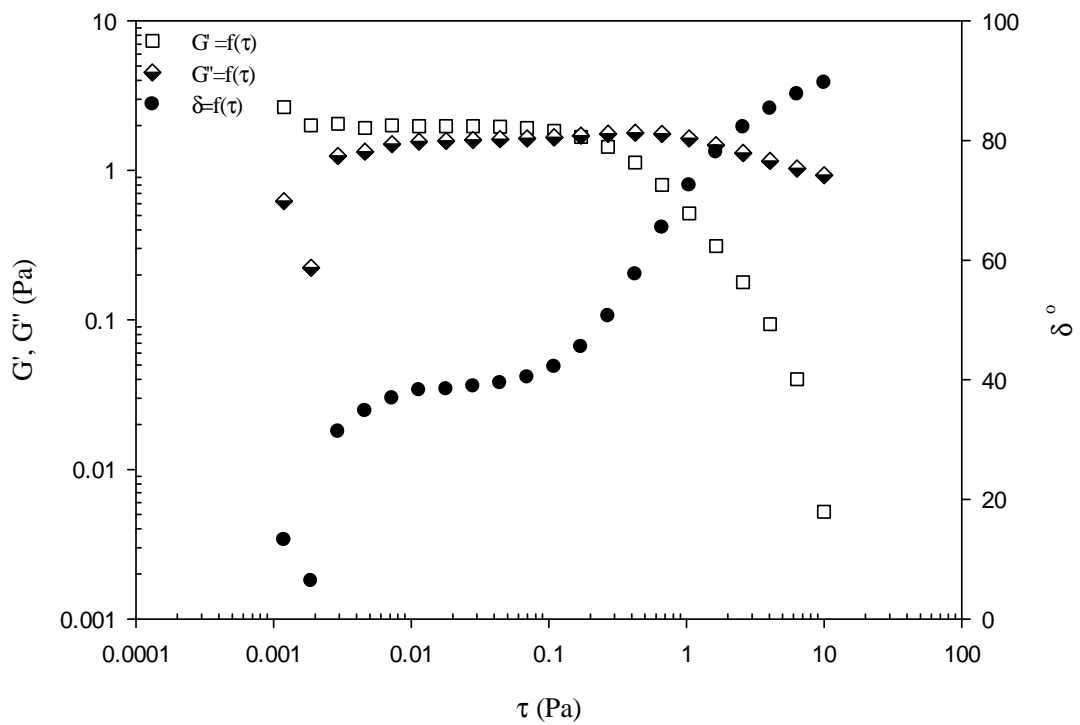


Figure 4.122. Amp-sweep graph of 40 vol% suspension of SS3 in ethylene glycol.

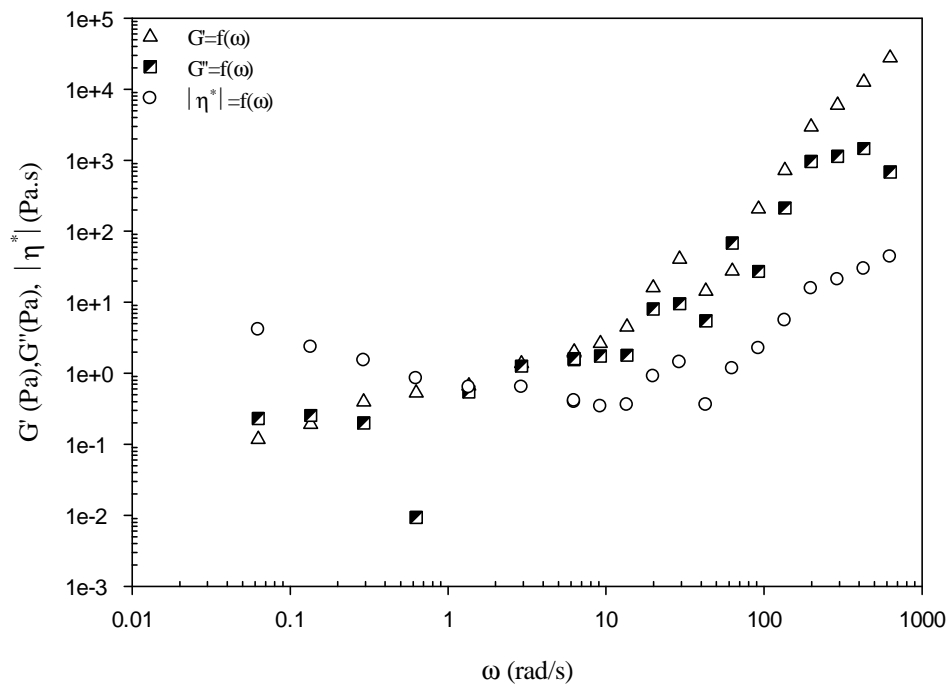


Figure 4.123. Freq-sweep graph of 40 vol% suspension of SS3 in ethylene glycol.

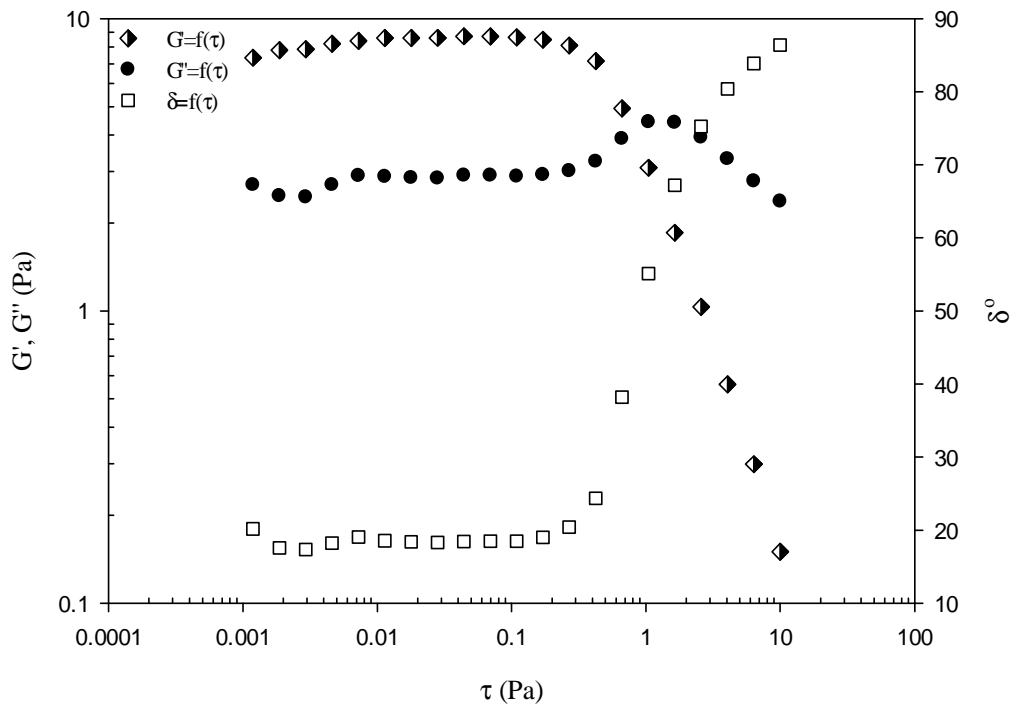


Figure 4.124. Amp-sweep graph of 45 vol% suspension of SS3 in ethylene glycol.

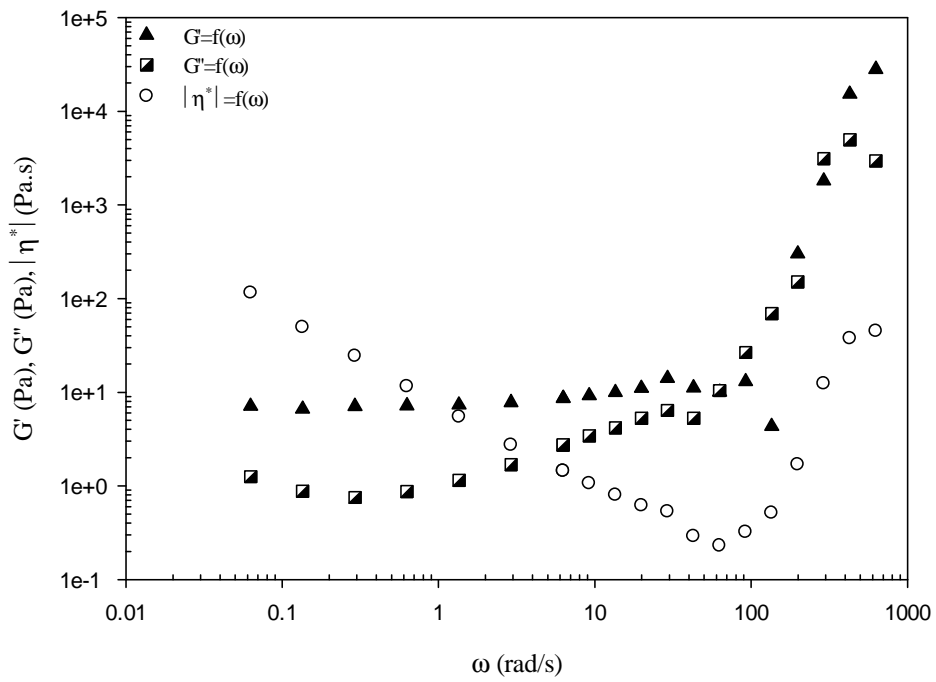


Figure 4.125. Freq-sweep graph of 45 vol% suspension of SS3 in ethylene glycol.

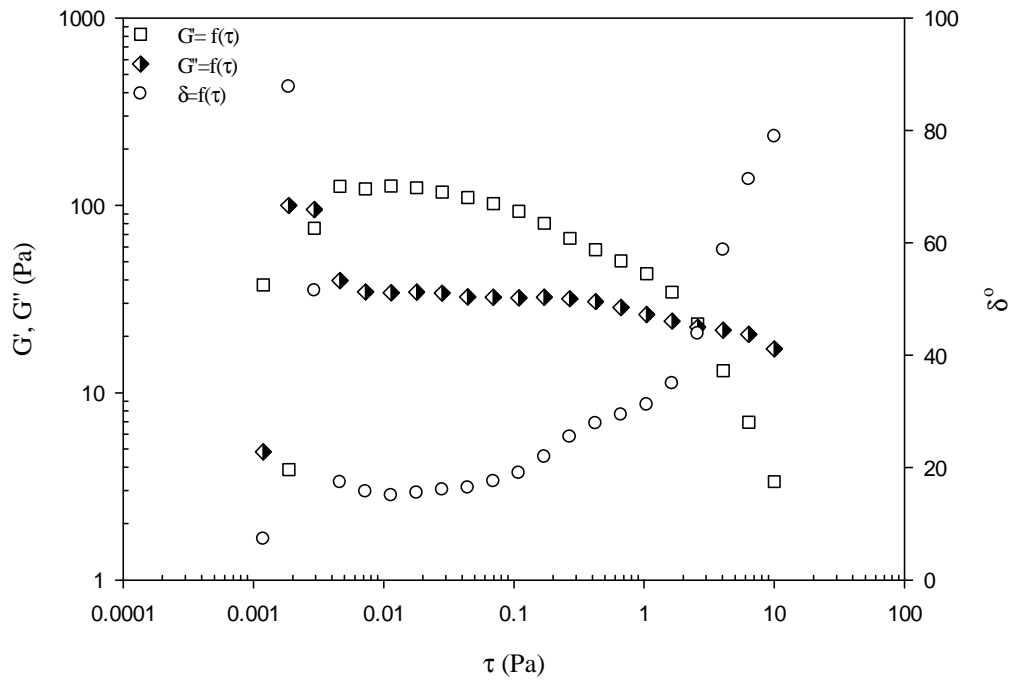


Figure 4.126. Amp-sweep graph of 47 vol% suspension of SS3 in ethylene glycol.

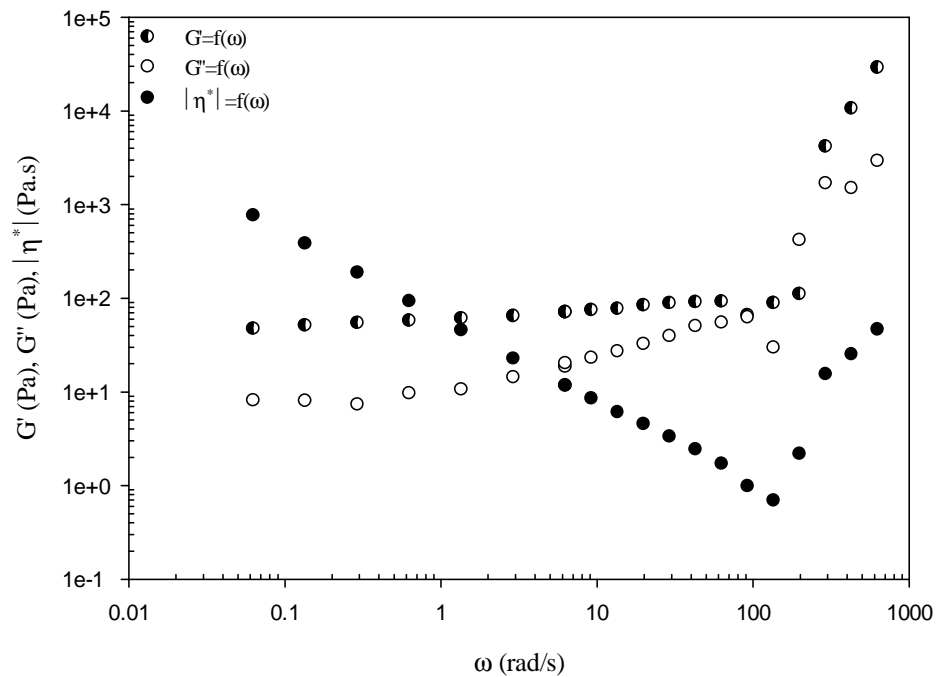


Figure 4.127. Freq-sweep graph of 47 vol% suspension of SS3 in ethylene glycol.

## 4.4. Characterization and Rheological Behaviour of $Al_2O_3$

### 4.4.1. Characterization of $Al_2O_3$ Particles

The SEM pictures of the powders AL1 and AL2 are seen respectively in Figures 4.128 and 4.130. The particle size distribution of powder AL1 is shown in Figure 4.129. The average particle size is found as 326 nm. Figure 4.131 displays the the particle size distribution of the powder AL2. The powder has a polydisperse particle size distribution. The average particle size by volume is 291 nm and 63 nm.

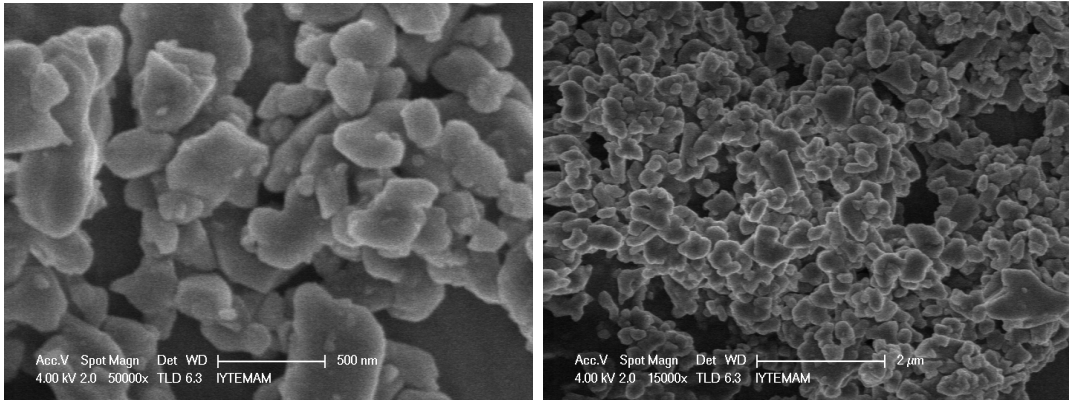


Figure 4.128. The SEM micrographs of AL1.

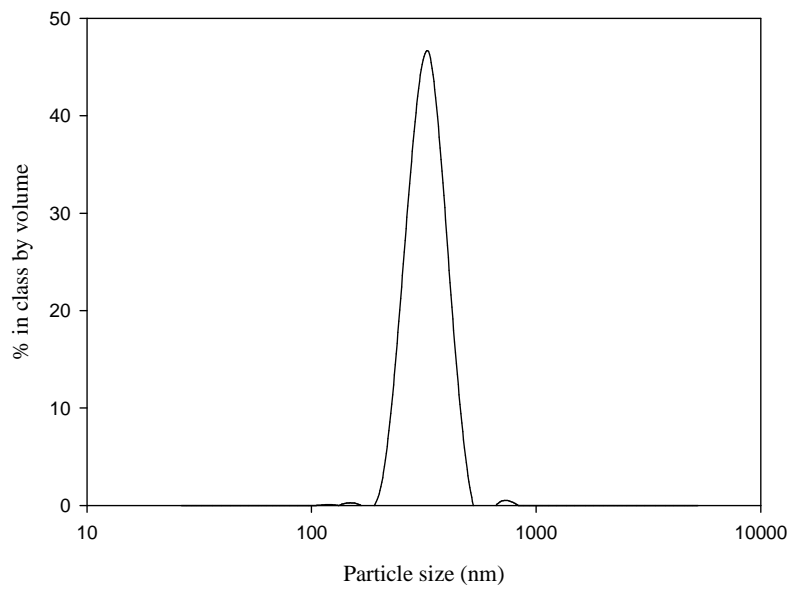


Figure 4.129. Particle Size Distribution of AL1.

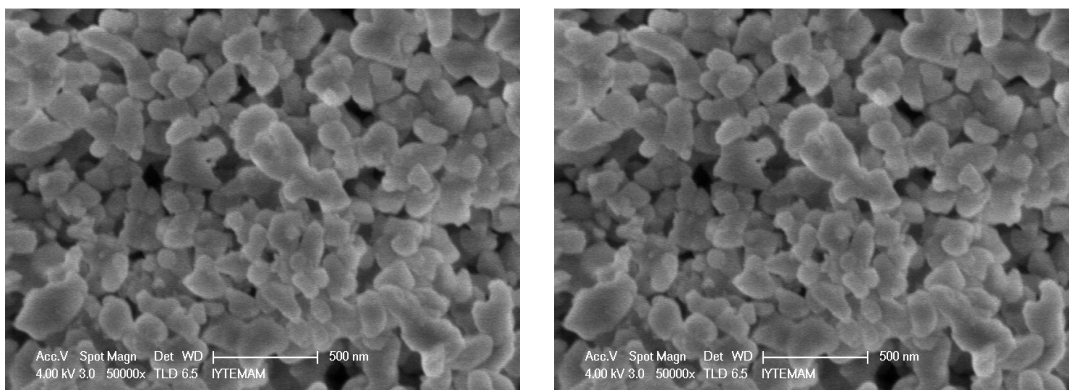


Figure 4.130. The SEM micrographs of AL2

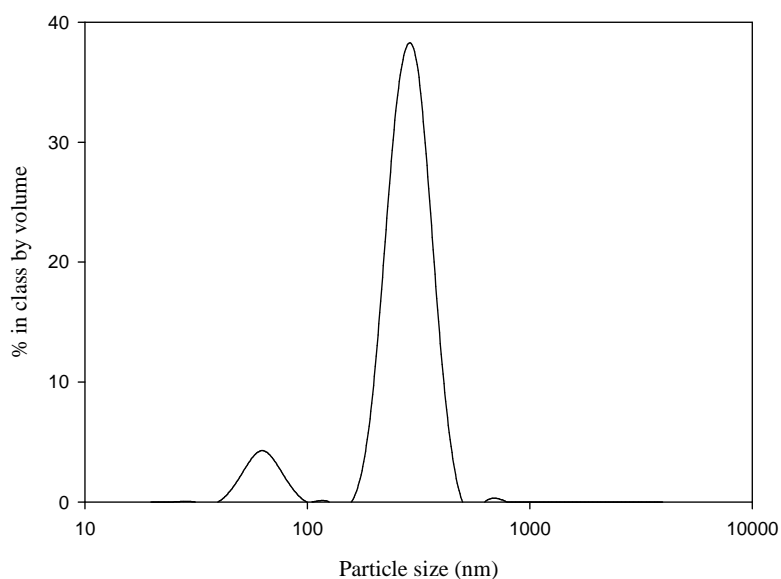


Figure 4.131. Particle Size Distribution of AL2.

#### 4.4.2. Rheological Behaviour of Al<sub>2</sub>O<sub>3</sub> Suspensions

The alumina particles were dispersed in ethylene glycol for the investigation of their rheological behaviour. The dynamic viscosity and flow curves of the suspensions of AL1 in ethylene glycol at different solids contents are given in Figure 4.131 and 4.132. The solids contents of silica spheres changed from 20 to 58 vol% without any surfactant. The viscosity of the suspension decreased for the  $\Phi$  values between 0.2 and 0.3 as the shear rate increased. The shear thickening behaviour was seen firstly in the particle volume  $\Phi= 0.4$ .

The dynamic viscosity and flow curves of AL2 at different solids contents in ethylene glycol are given in Figure 4.133 and 4.134. The solids contents of silica spheres changed from 40 to 62 vol% without any surfactant. The shear thickening behaviour was seen initially in the particle volume  $\Phi= 0.615$ .

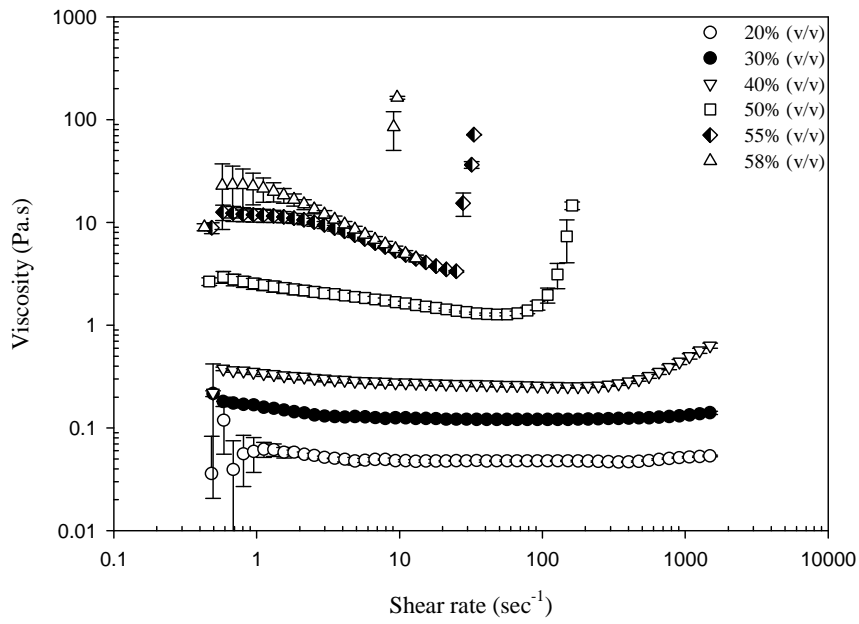


Figure 4.131. Dynamic viscosity curves of the suspensions of AL1 in ethylene glycol at different solids contents.

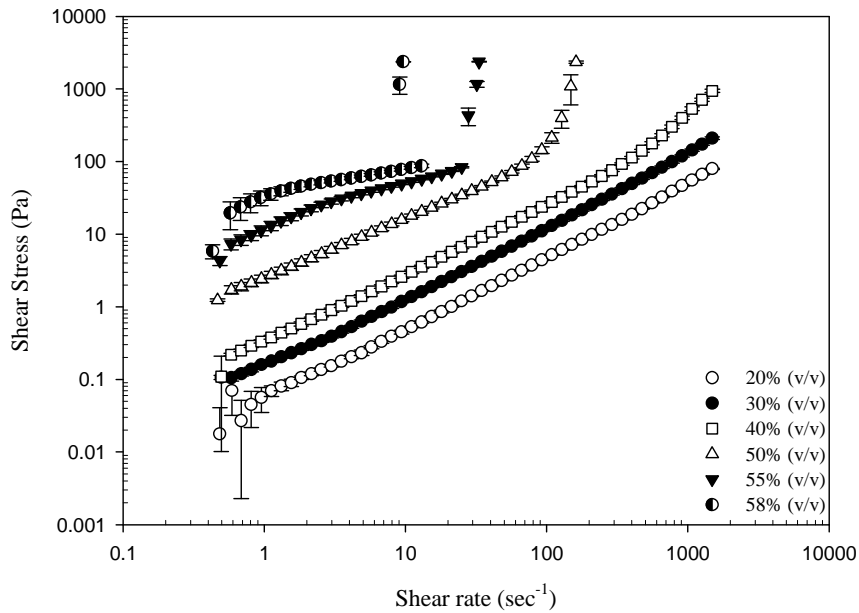


Figure 4.132. Flow curves of the suspensions of AL1 in ethylene glycol at different solids contents.

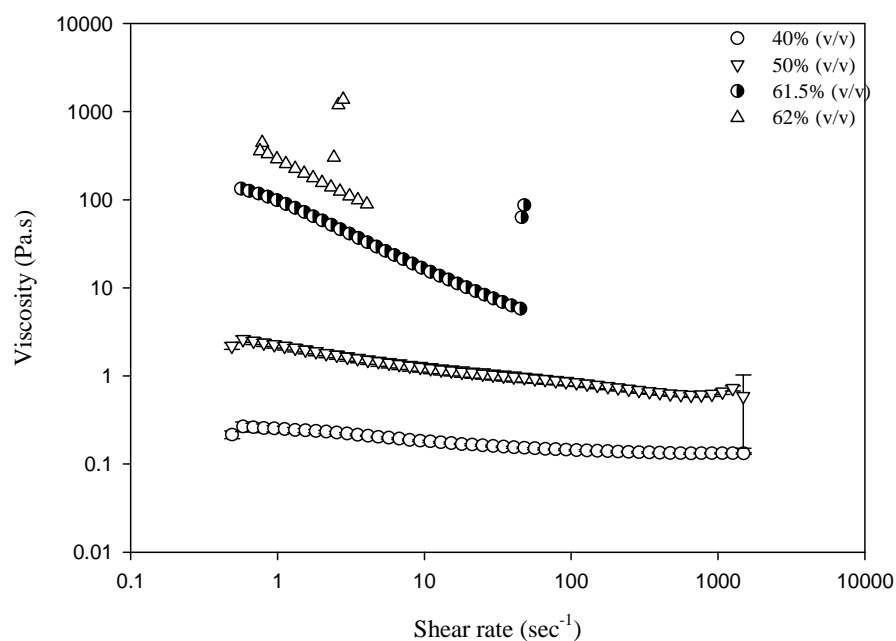


Figure 4.133. Dynamic viscosity curves of the suspensions of AL2 in ethylene glycol at different solids contents.

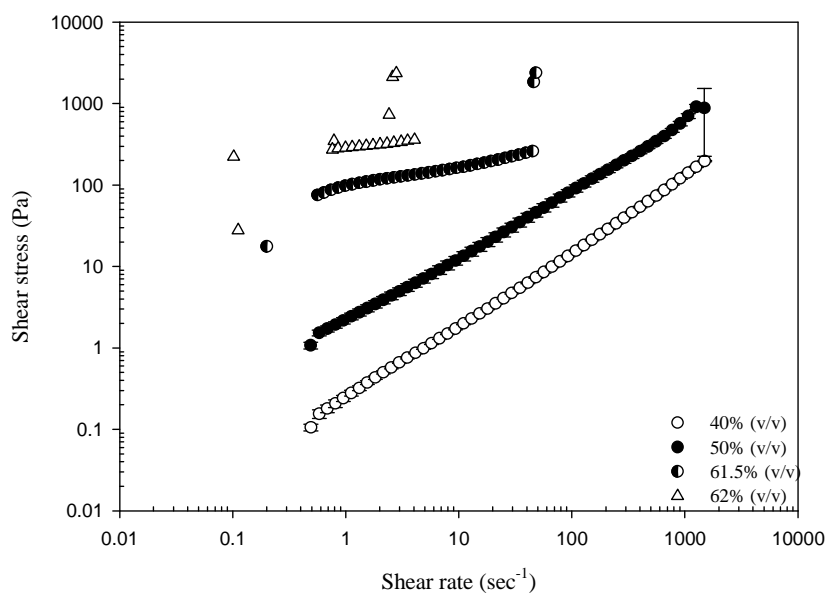


Figure 4.134. Flow curves of the suspensions of AL2 in ethylene glycol at different solids contents.

## 4.5. Characterization and Rheological Behaviour of ZrO<sub>2</sub>

### 4.5.1. Characterization of ZrO<sub>2</sub> Particles

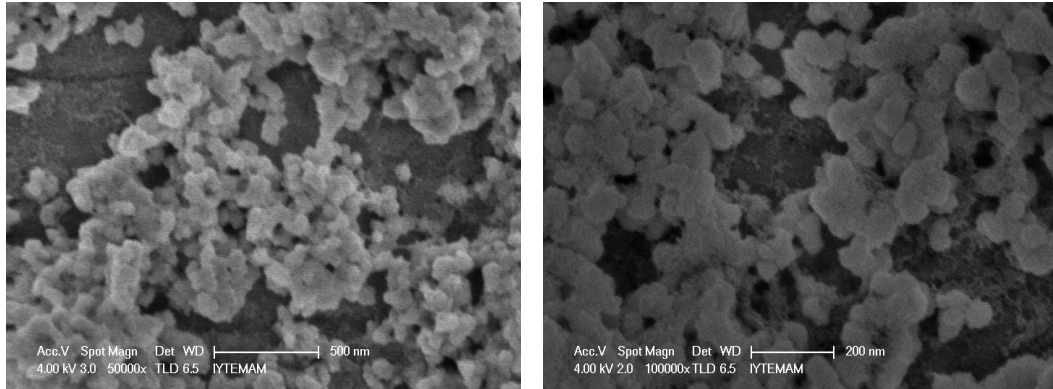


Figure 4.135. The SEM micrographs of zirconia

The SEM micrographs of the zirconia powder is seen in Figures 4.135. The average particle size is about 100 nm.

### 4.5.2. Rheological Behaviour of ZrO<sub>2</sub> Suspensions

The dynamic viscosity and flow curves of the suspensions of zirconia powder in ethylene glycol at different solids contents are given in Figure 4.136 and 4.137. The solids contents of zirconia particles changed from 30 to 53 vol% without any surfactant. The shear thickening behaviour was seen firstly in the particle volume  $\Phi = 0.4$ .

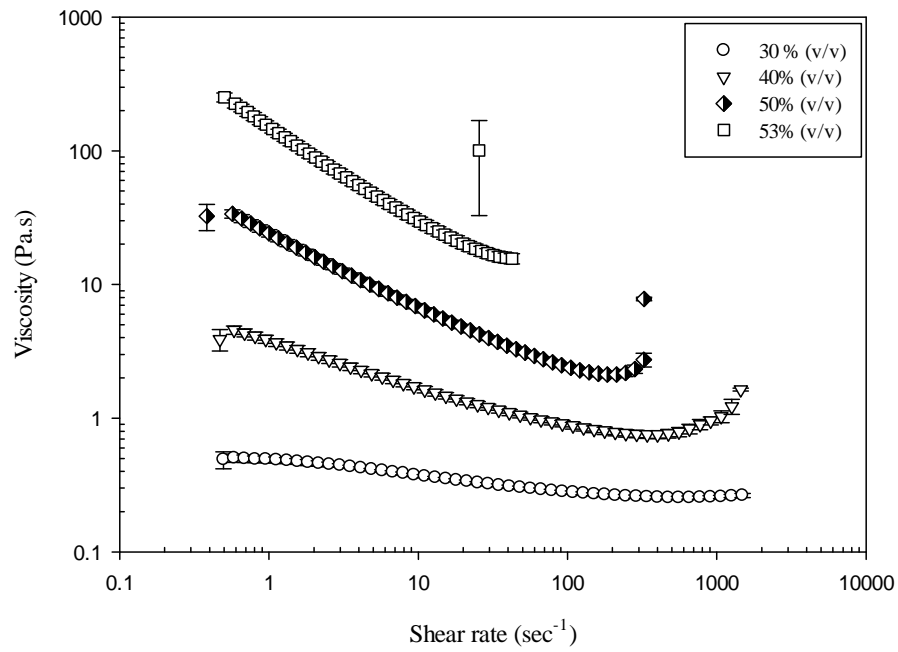


Figure 4.136. Dynamic viscosity curves of the suspensions of zirconia in ethylene glycol at different solids contents.

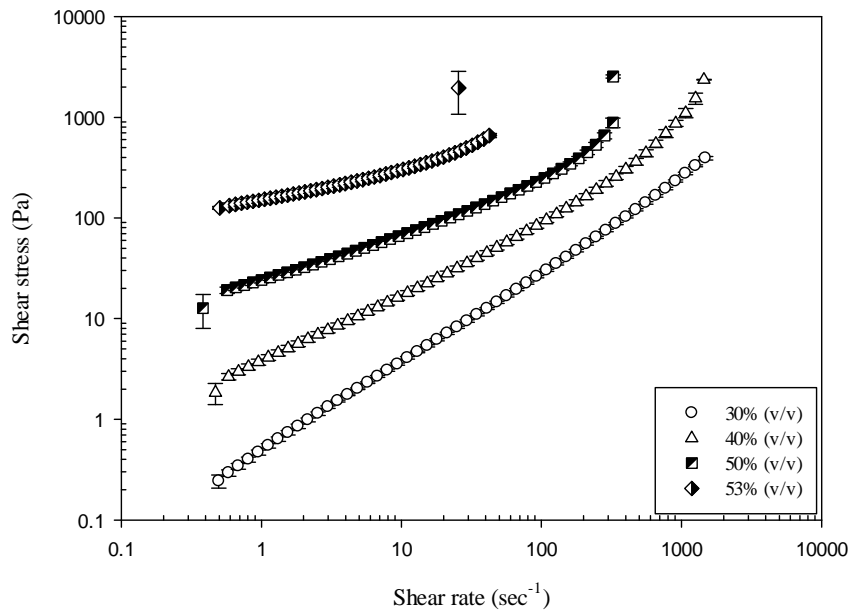


Figure 4.137. Flow curves of the suspensions of zirconia in ethylene glycol at different solids contents.

## CHAPTER 5

### CONCLUSIONS

The suspensions of submicron/nanosized calcium carbonate, titania, silica, alumina and zirconia particles were prepared in ethylene glycol in order to examine the rheological behaviour. Whisker like  $\text{CaCO}_3$  particles were synthesized via a carbonization route. The particles were suspended up to 45% solid content by volume. The shear-thickening fluid behaviour was observed, which was verified by Power law. However, the ballmilled natural  $\text{CaCO}_3$  particles with zirconia beads showed shear-thinning behaviour. In fact, 30% was the limit of the solid loading, since it was difficult to disperse the ballmilled particles whose sizes decreased from 1-2 $\mu\text{m}$  to 50 and 250 nm. Dispersant was used to suspend some of the commercial  $\text{TiO}_2$  powders in ethylene glycol so that higher volume concentrations could be prepared. Some of the  $\text{TiO}_2$  particles have a polydispersed particle size distribution, which led to decrease the solid volume content at which shear thickening was firstly seen. The maximum shear rate obtained was 3259 Pa.s for  $\text{TiO}_2$  suspensions. Nonetheless, in the  $\text{TiO}_2$  suspensions which were composed of polydispersed particles there was not a severe viscosity increase in the shear-thickening region. The onset of shear-thickening was observed at 47% solid loading in  $\text{SiO}_2$  suspensions which was higher than the solid volume content in precipitated  $\text{CaCO}_3$  and  $\text{TiO}_2$  suspensions. The highest solid loading was achieved in alumina suspensions as 62 vol%. Higher shear rates ( $>1500 \text{ sec}^{-1}$ ) could not be performed in rheology tests owing to the rheometry limitations. As a consequence, the maximum viscosities which the suspensions could reach were not possible to record. In addition to this, the third region in shear-thickening fluids where a steep shear-thinning occurs for values of  $\dot{\gamma} > \dot{\gamma}_{max}$  could not be investigated. The  $\Phi_{max}$  values were calculated through adaptation of the modified Krieger–Dougherty equation to experimental viscosity data. Power law and modified version of Cross model were used in curve fitting of experimental data in the shear thinning and shear thickening regions. The best fit was achieved with Power law for both shear thinning and shear thickening regions for all powder suspensions. Besides, the modified Cross-model was examined

not to fit well to the viscosity data in shear-thinning regions while the fitting in shear-thickening region was quite reasonable. The models couldn't be fitted to the data in shear thickening region for some  $\text{TiO}_2$  and  $\text{SiO}_2$  suspensions. Since there were not enough data to apply curve fitting. The oscillatory tests were only carried out for  $\text{SiO}_2$  suspensions successfully. According to the results of dynamic shear rheology measurements, the more solid volume content was increased in the suspension, the more dominant solid part of the suspensions became over the liquid part for silica particles.

Shear thickening fluids whose rheology research is a hot topic nowadays, can be employed as dampers, armours, brakes in vehicles, sensors, micro-fluidic materials, vibration and/or noise reduction in vehicles, and prosthetic limbs. Comprehending the mechanism of rheological behaviour of the dispersions is essential in the application of the particulate suspensions. The rheological behaviour of the particulate suspensions in non-aqueous media is required to be further investigated so as to understand particle-particle and particle/medium interactions.

## REFERENCES

- Barnes, H. A. Shear-Thickening (“Dilatancy”) in Suspensions of Nonaggregating Solid Particles Dispersed in Newtonian Fluids *Journal of Rheology* **1989**, 33(2), 329-366.
- Bergström, L. Rheological Properties of Concentrated, Nonaqueous Silicon Nitride Suspensions *J. Am. Ceram. Soc.* **1996**, 79(12), 3033-40.
- Bergström, L. Shear thinning and shear thickening of concentrated ceramic suspensions *Colloids and Surfaces A Physicochemical and Engineering Aspects* **1998**, 133, 151-155.
- Bogush, G.; Tracy, M.; Zukoski, C. Preparation of Monodisperse Silica Particles: Control of Size and Mass Fraction *Journal of Non-Crystalline Solids* **1997**, 104, 95-106.
- Burns, J. R.; Jachuck, R. J. J.; Monitoring of CaCO<sub>3</sub> Production on a Spinning Disc Reactor Using Conductivity Measurements *AIChE Journal* **2005**, 51(5), 1497-1507.
- Chadwick, M. D.; Goodwin, J. W.; Vincent, B.; Lawson, E. J.; Mills, P. D. A. Rheological behaviour of titanium dioxide (uncoated anatase) in ethylene glycol *Colloids and Surfaces A, Physicochemical and Engineering Aspects* **2002**, 196, 235-245.
- Cho, K.; Chang, H.; Kil, D.; Kim, B.; Jang, H. Synthesis of dispersed CaCO<sub>3</sub> nanoparticles by the ultrafine grinding *Journal of Industrial and Engineering Chemistry* **2009**, 15, 243–246.
- Conley Robert F., Practical Dispersion Wiley-VCH, Inc. 1996
- Egres, R. G.; Nettesheim, F.; Wagner, N. J. Rheo-SANS investigation of acicular-precipitated calcium carbonate colloidal suspensions through the shear thickening transition *J. Rheol.* **2006**, 50 (5), 685-709.
- Franks, G. V.; Zhou, Z.; Duin N. J., Boger D. V. Effect of interparticle forces on shear thickening of oxide suspensions *J.Rheol.* **2000**, 44(4), 759-779.
- Galindo-Rosales, F. J.; Rubio-Hernandez, F. J.; Sevilla A. An apparent viscosity function for shear thickening fluids *J. Non-Newtonian Fluid Mech.* **2011**, 166, 321–325.

- Galindo-Rosales, F. J.; Rubio-Hernandez F. J.; Velázquez-Navarro Shear thickening behaviour of Aerosil R816 nanoparticles suspensions in polar organic liquids *Rheol Acta* **2009**, 48, 699-708.
- Garcia, F.; Bolay N. L.; Trompette J. L.; Frances C. On fragmentation and agglomeration phenomena in an ultrafine wet grinding proces : the role of polyelectrolyte additives *Int. J. Miner. Process.* **2004**,74S, S43–S54.
- Goodwin J., Hughes, R. Rheology for Chemists, An Introduction, The Royal Society of Chemistry, 2000.
- Gregorova, E.; Pabst, W. Porosity and pore size control in starch consolidation casting of oxide ceramics-Achievements and problems *Journal of the European Ceramic Society* **2007**, 27, 669–672.
- Hassan, T. A.; Rangari, V. K.; Jeelani S. Sonochemical synthesis and rheological properties of shear thickening silica dispersions *Ultrasonics chemistry* **2010**, 17, 947–952.
- Hoffman, R. L. Explanations for the cause of shear thickening in concentrated colloidal suspensions *Inc. J. Rheol.* **1998**, 42(1), January/February,111-123.
- Hunter Robert J., Foundations of Colloidal Science 2nd ed.; Oxford University Press, 2001
- Inam, M. A.; Ouattara S., Frances C. Effects of concentration of dispersions on particle sizing during production of fine particles in wet grinding process *Powder Technology* **2011**, 208(2), 329-336.
- James F. Steffe, Ph.D., P.E. Rheological Methods in Food Process Engineering 2nd ed.; Freeman Press, East Lansing, MI, USA, 1996.
- Kalman, D. P.; Schein, J. B.; Houghton, J. M.; Laufer, C. H. N.; Wetzel, E. D.; Wagner, N. J. Polymer Dispersion Based Shear Thickening Fluid-Fabrics for Protective Applications *Proceedings of Sample* **2007**, June.
- Larson Ronald G., The Structure and Rheology of Complex Fluids Oxford University Press, NewYork, 1999.
- Lee, K.; Look, J.;Harris, M.; McCormick V. Assessing Extreme Models of the Stöber Synthesis Using Transients under a Range of Initial Composition *Journal of Colloid and Surfaces* **1997**, 194, 78-88.

- Lee, Y. S.; Wetzel, E. D.; Wagner, N. J. The ballistic impact characteristics of Kevlar woven fabrics impregnated with a colloidal shear thickening fluid *Journal of Materials Science* **2003**, 38, 2825-2833.
- Mewis, J.; Wagner, N. J. Current trends in suspension rheology *J. Non-Newtonian Fluid Mech.* **2009**, 157, 147-150.
- Mezger Thomas G., *The Rheology Handbook* 2nd rev. ed.; Ulrich Zorll, 2002.
- Morris, G. E.; Skinner, W. A.; Self, P. G.; Smart, R. C. Surface chemistry and rheological behaviour of titania pigment suspensions *Colloids and Surfaces A: Physicochemical and Engineering Aspects* **1999**, 155, 27-41.
- Peker S., Helvacı Ş., *Solid-Liquid Two Phase Flow*, Elsevier 2008.
- Ruiz, M.; Hernandez, J.; Banos, L.; Montes, J.; Garcia, M. Characterization of Calcium Carbonate, Calcium Oxide, and Calcium Hydroxide as Starting Point to the Improvement of Lime for Their Use in Construction *Journal of Materials in Civil Engineering* **2009**, 21(11), 694-698.
- Sajan, C.; Basavalingu, B.; Ananda, S.; Byrappa, K. Comparative Study of Photodegradation of Indigo Carmine Dye Using Commercial TiO<sub>2</sub> and Natural Rutile *Journal of the Geological Society India* **2011**, 77(1), 82-88.
- Schramm, G. *A Practical Approach to Rheology and Rheometry* 2nd ed.; Gebrueder HAAKE gmbh, Karlsruhe, Germany, 1998.
- Stober, W.; Fink, A.; Bohn, E. Controlled Growth of Monodisperse Silica Spheres in the Micron Size Range *Journal of Colloid and Interface Science* **1968**, 26, 62-69.
- Topuz, B., *Gas Permeation through sol-gel derived alumina and silica based membranes* Ph.D. Dissertation İzmir Institute of Technology, İzmir, 2009.
- Wagner, N. J.; Brady, J. F. Shear thickening in colloidal dispersions *Physics Today* **2009**, October, 27-32.
- Wang, C.; Sheng, Y.; Zhao, X.; Pan, Y.; Bala, H.; Wang, Z. Synthesis of hydrophobic CaCO<sub>3</sub> nanoparticles *Materials Letters* **2006**, 60, 854-857.
- Weitz, D.; Wyss, H.; Larsen, R.; Harvard University *G.I.T. Laboratory Journal* **2007**, 3(4), 68-70.

Wu, J.; Hao, S.; Lin, J.; Huang, M.; Huang, Y.; Lan, Z.; Li, P. Crystal Morphology of Anatase Titania Nanocrystals Used in Dye-Sensitized Solar Cells *Crytal Growth & Design* **2008**, 8(1), 247-252.

Zupancic, A.; Lapasin, R.; Zumer, M. Rheological characterisation of shear thickening TiO<sub>2</sub> suspensions in low molecular polymer solution *Progress in Organic Coatings* **1997**, 30, 67-78.

